International Journal of Hydrogen Energy

Methane dry reforming on fibrous silica-alumina employing nanocrystals of nickel and cobalt to recognize the most efficient metal

--Manuscript Draft--

Manuscript Number:	HE-D-22-07791R1
Article Type:	SI: Nanomaterials & hydrogen (Vasseghian)
Section/Category:	Catalysts / Electrocatalysts / Photocatalysts
Keywords:	cobalt, nickel; carbon resistance; methane dry reforming; Fibrous silica-alumina
Corresponding Author:	A.A. Jalil, Ph.D Universiti Teknologi Malaysia Johor Bahru, MALAYSIA
First Author:	A.H.K Owgi, Ph.D.
Order of Authors:	A.H.K Owgi, Ph.D.
	A.A. Jalil, Ph.D
	M.A.A Aziz, Dr
	W Nabgan
	M. Alhassan, Ph.D.
	M.Y.S. Hamid
	N.S Hassan
	R Saravanan, Dr
	M.B. Bahari, Dr
	M.H.M Sofi

Feb.1, 2023

Editor in Chief
International Journal of Hydrogen Energy

Ms. Ref. No.: HE-D-22-07791

Dear Dr.

Thank you very much for the review of our manuscript and for giving us an opportunity to revise the manuscript entitled " *Methane dry reforming on fibrous silica-alumina employing nanocrystals of nickel and cobalt to recognize the most efficient metal*". We are also grateful to the reviewers for the helpful comments. The manuscript has been revised after carefully considering the comments.

As shown in the following pages, all the comments are addressed clearly and appropriately. In addition, some corrections have been made. All of the changes are highlighted in yellow in the manuscript. We believe that the revised manuscript is now acceptable for publication since this manuscript is also in line with the objective and scope of *Fuel Journal.*

Thank you again for your time and consideration of this manuscript.

Best Regards,

Prof. Dr. Aishah A. Jalil,
Centre of Hydrogen Energy,
Institute of Future Energy,
School of Chemical and Energy Engineering,
Faculty of Engineering,
Universiti Teknologi Malaysia
81310 UTM Johor Bahru, Johor, Malaysia
Tel : +60-7-5535581 Fax : +60-7-5588166
Email : aishahaj@utm.my

Ms. Ref. No: **HE-D-22-07791**
Title: *The preferable Ni quantity to boost the performance of FSA for dry reforming of methane Fuel.*

- The changes have been done in the manuscript according to the reviewer's comments.
- All of the changes are highlighted in yellow.

Reviewer: 1

No.	Comment	Response to comment	Remark
1	In abstract part, authors must be discuss about results of nanomaterials and output of it	Thank you for your comment. We have revised it by adding nanomaterial notice. Presently, the production of syngas through the dry reforming of methane is a widely employed approach for reducing vast amounts of greenhouse gas emissions. Several metals, particularly transition metals support have been evaluated as active DRM catalyst systems. In this work, a comparative studies is presented between Cobalt and Nickel metals impregnated over fibrous silica-alumina (FSA) support synthesized by the hydrothermal method for dry methane reforming. The specimens were characterized via FESEM mapping, TEM, XRD, H_2-TPR, XRF, N_2 physisorption, and KBr-FTIR techniques. Unlike the Co/FSA, Ni/FSA displayed a higher surface area with a fine dispersion of Ni nano-crystalline and less agglomeration, and more active sites which enhanced the metal-support interaction. Approximately 0.2g of each catalyst was evaluated at 650 - 800 ºC with a respective. CH_4:CO_2:N_2 ratio of 1:1:2, gas hourly space velocity 30,000 mL g^{-1} h^{-1}. The Ni/FSA demonstrated more conversion of CH_4 (89%) over (67%) of Co/FSA at 800ºC. After 10 h of long-term reaction, the Ni/FSA exhibited more stability at 800 ºC. TGA/DTA, Raman, and TEM results showed that spent Ni/FSA catalysts did not demonstrate signs of considerable nano-graphitic carbon or metal sintering as compared to Co/FSA catalysts, which had bigger crystallites of Co. The finding of this study would add new knowledge on reaction conditions involving and catalytic activities of the metals over the FSA.	Page. iii

2	Discuss about FT-IR isnot clear and need more discuss and add suitable references	Thank you for your comment. We have revised it with added more discussion. FTIR spectroscopy with wavelengths between 400 and 4000 cm-1, assessed the various construction heterogeneity of the (Co and Ni) supported FSA, as exhibited in figure.5. The most prominent peaks exhibited siliceous frames because Si interacted with various atoms, (for instance, Si-O-Si, Si-OH, Si-O, Al-O-Al, and Si-O-Al) through the range 400–1300 cm^{-1}. [52]. The wavenumbers of five peaks 1240, 1090, 960, 790, also 460 cm^{-1} were demonstrated in all specimens, which is indicative of Si-O-Si element through peaks in a range of 960-1260 cm^{-1} were apparent via all samples [53]. Simultaneously, all catalysts in fig.5 possess a peak at 3400 cm^{-1} indicating that O-H-stretching is caused by water molecules, which are related to (Brønsted acid sites) increasing ions of hydrogen concentration [54,55]. As displayed in fig.5 Ni/FSA possesses a low-intensity of peak at 3400 cm^{-1} reflected in low Brønsted acid sites. Furthermore, Si-O-Si transverse-optical (TO) and longitudinal-optical (LO) band asymmetric stretching were attributed to the dominant transmittance peak at approximately 1240 cm^{-1} and 1090 cm^{-1}, respectively [56–58]. The weak bands at 960 and 1640 cm^{-1} were assigned external groups of Si-OH, whilst symmetric and asymmetric Al-O and Si-O stretch vibrations were revealed at 800 cm^{-1} and 462 cm^{-1}, respectively [59]. Moreover, asymmetrical and symmetrical stretched vibrations, in addition to stretching vibrations of Si-O-Al, were ascribed to the bands at 1090 cm^{-1}, 790 cm^{-1}, and approximately 460 cm^{-} [60] [1]. The robustness of these peaks diminished when Ni and Co were introduced to FSA, realization that the Si–O–Si and Si-OH were partly replaced by Ni–O–Si, Co–O–Si, Ni-O, and Co–O. In particular, in the Co/FSA spectra, one special peak at 666 cm^{-1} attributable to Co–O vibrations occurred, indicating to the Co had been successfully incorporated into the catalyst [17,41]. The substitution result of O–H and O–Si with the Ni ions in the dendritic fibrous FSA structure showed a greater reduction in peak density compared to the Co sample, which emphasizes that Ni had a more robust interaction with FSA support than Co [61,62].	Page. 11,12
3.	In conclusion section, I cannot see any data from your works? whats happen and whast results coming?	Thank you for your comment we have more clarity. To conclude, fibrous silica-alumina (FSA) has been synthesized through the hydrothermal method with various loading metals by the impregnation method. In the KBr-FTIR and H_2-TPR investigations, the appearance of the degree of metal interactions was conditional on	

		metal dispersion attributed to metal crystallite size on the support surface. Accordingly, Ni/FSA generated superlative function in the DRM reaction across a temperature range of 500–850 °C and extraordinary stability over 10 h it due to its a large surface area (338.56 m^2/g), fine size dispersion of Ni, and strong metal-support interaction, as well as strong resistance to sintering by restricting Ni atoms or crystallite movements on the support. However, Co/FSA had a bigger crystallinite size, which affects the metal-support interaction reflected in the performance of the catalyst. The Ni/FSA catalyst serves as a coke inhibitor and a disordered amorphous phase with no effect on the catalyst stability. These characteristics are the vital causes for Ni/FSA catalyst's superior efficiency to Co/FSA synthesized via wet impregnation. As documented, the conversion of CH_4 was 97.5% for Ni/FSA, while it dramatically dropped to 20.63% for Co/FSA	Page.17
4.	please remove Ni/FSA manifested in the high conversion of CH4 at 96 % and CO2 at 90 % from keyword	Thank you for your comment. We have removed it **Research highlights** • The small Ni particles resist the coke aggregation • The oxygen capacity of the supports inhibits coke formation • Active sites in dendritic fibrous are easily accessible • The catalytic activity is dependent on the metal-support interaction • Carbon nanotubes influence the catalytic activity	Highlights
5.	Purity of materials and also detail of companies relative to instruments must be clear.	Thank you for your comment. We have revised and added more details. Fibrous silica-alumina support has been generated through the hydrothermal method and Al_2O_3. Alumina nitrate (Sigma-Aldrich, > 98%) was combined into a homogenous mixture of n-butanol (Merck, > 98%) and toluene (Sigma-Aldrich, > 98%). Afterwards, the solution was stirred for approximately 30 min prior to introducing TEOS (Merck, > 98%) and was poured dropwise. Urea (Merck, > 98%), Cetrimonium bromide (CTAB- Sigma-Aldrich, > 98%), and 0.75 L of deionized water were added to the mixture. Toluene/1-butanol=13.8, urea/CTAB=3.8, and Si/Al=1.23 are the essential variables. While being exposed to microwave radiation at 400 W for 360 min, the subject substance was vaporized at 120 ℃	Page.5

		for overnight evaporation. The white specimen was heated in a furnace for 360 min at 550 C to produce FSA support. To load metals onto FSA, a 5 wt% Co and Ni-impregnated solution of $Co(NO_3)_2$ and Ni $(NO_3)2.6H_2O$ were (% trace metals) used as purchased from Sigma-Aldrich. Bhd. They dissolved in deionized water was deployed. Beforein getting impregnated, the specimens were evaporatively dried and then calcined for three hours at 550 °C. Co/FSA and Ni/FSA were the end products of this procedure.	

Reviewer: 2

No.	Comment	Response to comment	Remark
1	1 Highlight needs to recheck and revise. Several points are difficult to understand.	Thank you for your comment. We have revised and rewrote them. • The small Ni particles resist the coke aggregation • The oxygen capacity of the supports inhibits coke formation • Active sites in dendritic fibrous are easily accessible • The catalytic activity is dependent on the metal-support interaction • Carbon nanotubes influence the catalytic activity	Highlight
2.	Highlight - "The metal physiochemical properties optimized the activity of a catalyst". Why focus on the physiochemical properties of metal and not the catalyst? What are the characterization analyses used to evaluate the metal properties?	Thank you for your comment. We have revised the highlights and rewrote them. • The small Ni particles resist the coke aggregation • The oxygen capacity of the supports inhibits coke formation • Active sites in dendritic fibrous are easily accessible • The catalytic activity is dependent on the metal-support interaction • Carbon nanotubes influence the catalytic activity	Highlight
3.	Whole manuscript - All abbreviations should be defined before being used.	Thank you for your comment. We have revised and provided the abbreviations. **Abbreviation.** (GHGs): Greenhouse gas. (DRM): Dry reforming of methane. (FSA): Fibrous silica-alumina. (CTAB): Cetrimonium bromide. (TEOS): Tetraethyl orthosilicate.	Page . ii

		(XRD): X-ray diffractograms. XRF): X-ray fluorescence (FESEM): Field emission scanning electron microscopy. (FTIR): Fourier-transform infrared. (TEM): Transmission electron microscopy. (H_2-TPR): H_2 temperature program reduction. (TGA): Thermogravimetric analysis. (GC): Gas chromatography. (BET): Brunauer-Emmett-Teller. (C-NTs): Carbon nanotubes (D-band): Disorder-generated band (G-band): Graphite carbon band (TCD): Thermal conductivity detector (NLDFT): Non-local density functional theory (TO): Transverse-optical (LO): Longitudinal-optical	
4.	Fig.1a seems compressed because the image wide is not similar to the others (Fig. 1b and Fig. 1c). Please check and revise.	Thank you for your comment. We have checked and revised it. 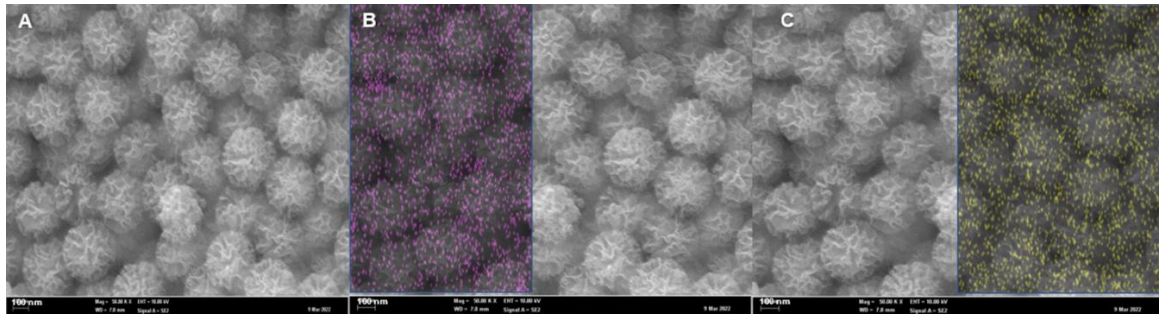 **Fig.1.** (A) FESEM image of FSA diffusion, (B) The particle mapping of Ni/FSA, (C) Co/FSA with mapping.	Page. 1

<table>
<tr><td></td><td></td><td></td><td></td></tr>
<tr><td>5.</td><td>As stated in the methodology, the amount of Co and Ni loaded is 5 wt%. Is there any characterization analysis used to confirm the amount of metal loading? This info is very important to ensure the difference in properties and activities originated from the type of metal and not the amount of metal used.</td><td>Thank you for your comment.
We have provided XRF analysis to confirm the metal loading.
Traces of cobalt and nickel were observed via catalysts are 5.10% and 4.84% respectively by XRF analysis in the table.2, The amounts of Ni-loading at 5% wt are consistent with the quantities employed during catalyst preparations, and the identifying amounts of compounds utilized in this investigation are true.

<table>
<tr><th>Sample</th><th>Ni (% wt)</th><th>SiO_2 (%wt)</th><th>Al_2O_3 (% wt)</th></tr>
<tr><td>Co/FSA</td><td>5.12%</td><td>76.18%</td><td>18.7%</td></tr>
<tr><td>Ni/FSA</td><td>4.84 %</td><td>79.2%</td><td>16.5%</td></tr>
</table>
</td><td>Page.10</td></tr>
<tr><td>6.</td><td>Fig. 6 - The reactant conversion over Ni/FSA and Co/FSA are similar at 700 oC. The explanation behind the findings should be included.</td><td>Thank you for your comment.
We have revised with added the details
Interestingly, the conversion of CH_4 and CO_2 at 700 were similar for the Ni/FSA and Co/FSA catalysts, indicating the possibility that side reactions such as; methane decomposition ($CH_4 \rightarrow C + 2H_2$) and the Boudouard reaction ($2CO \leftrightarrow C + CO_2$) have occurred [7,64].</td><td>Page.14</td></tr>
<tr><td>7.</td><td>Fig. 6 & Fig. 7 - Reaction conditions should be added in the caption for better understanding.</td><td>Thank you for your comment.
We have revised the captions with added more information.

Fig .6. Catalytic performance over the catalysts (A) CH_4 conversion and (B) CO_2 conversion with different catalysts (Condition: CO_2/CH_4=1:1, GHSV=50,000 $mL \cdot g_{cat}^{-1} \cdot h^{-1}$, P= 1atm, T= 500 to 850 ºC).

Fig. 7.Catalytic stability over the catalysts (A) CH_4 conversion, (B) CO_2 conversion, and (C) H_2/CO ratio (Condition: CO_2/CH_4=1:1, GHSV=50,000 $mL \cdot_{gcat}^{-1} \cdot h^{-1}$, P=1atm, T=850 °C, Tim= 10h).</td><td>List of figures</td></tr>
</table>

8.	Fig. 7 - 10h catalyst stability test is considered too short. Normally, stability of the catalyst is monitored with a long hour of reaction (example: 60 h)	Thank you for your comment. Actually, we measure the reaction stability throughout 10 hours, owing to the Co/FSA sample conversions of CH_4 and CO_2, which dropped to around 20% and 17%, respectively. So from our knowledge no need to continue the stability test.	Figure.6
9.	Fig. 7c - Significant decrease in syngas ratio was observed at 1-h of reaction for both catalysts. Why? Please provide the explanation	Thank you for your comment. We have revised and added more information. Simultaneous secondary reactions that occurred throughout catalytic testing were predictable. On the other hand, from the H_2/CO profiles as displayed in Fig. 7C, In actuality, a rise in the ratio of syngas on Ni/FSA after 6 hours was driven by the concomitant occurrence of CH_4 decomposition ($CH_4 \rightarrow C + 2H_2$) and CO disproportionation ($2CO \leftrightarrow C + CO_2$). These subsequent reactions neither simply influenced the syngas ratio, but also produced carbonaceous species that were detrimental to catalytic activity. On the contrary, in the first hours of the reaction, the syngas ratio was shown to drop for both specimens, which was caused by the reverse water gas shift (RWGS) reaction to the decrease in syngas ratio. and seem to improve with the favourability of thermodynamics [67,68]	Page. 15,16
10.	Fig. 7c - Significant increase was observed at 6 h for Ni/FSA. Why the ratio drastically increased at 6-h of reaction? Please provide a scientific explanation.	Thank you for your comment. We have revised and added more information. Simultaneous secondary reactions that occurred throughout catalytic testing were predictable. On the other hand, from the H_2/CO profiles as displayed in Fig. 7C, In actuality, a rise in the ratio of syngas on Ni/FSA after 6 hours was driven by the concomitant occurrence of CH_4 decomposition ($CH_4 \rightarrow C + 2H_2$) and CO disproportionation ($2CO \leftrightarrow C + CO_2$). These subsequent reactions neither simply influenced the syngas ratio, but also produced carbonaceous species that were detrimental to catalytic activity. On the contrary, in the first hours of the reaction, the syngas ratio was shown to drop for both specimens, which was caused by the reverse water gas shift (RWGS) reaction to the decrease in syngas ratio. and seem to improve with the favourability of thermodynamics [67,68].	Page. 15,16

11.	Why were the product selectivity and product yield not examined in this study?	Thank you for your comment. We have revised with added the selectivity and yield result. 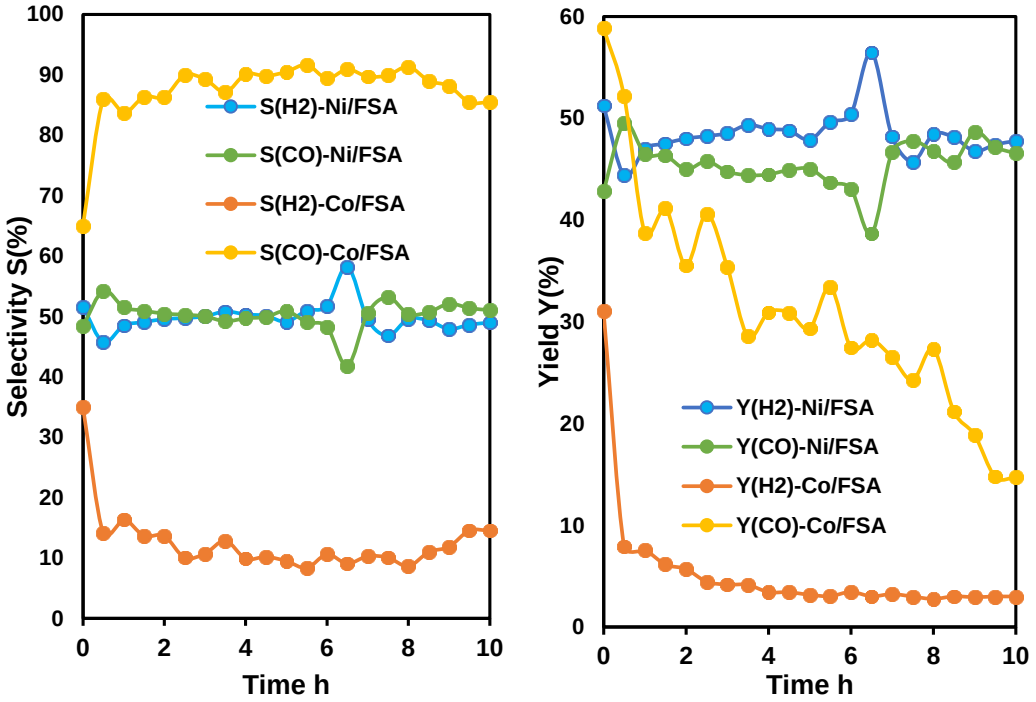 **Fig. 7**. (A) Selectivity of H_2 and CO, the (B) yield of H_2 and Co during methane dry reforming over Ni/FSA and Co/FSA According to Fig. 8, the H_2 yield showed a different trend with conversions, with Ni/FSA achieving the highest H_2 yields and Co/FSA achieving the lowest. Meanwhile, the exception of CO selectivity that appeared to be caused by the Co/FSA catalyst can be explained by the RWGS reaction ($CO_2 + H_2 \leftrightarrow CO + H_2O$). where the H_2 and CO selectivity of Ni/FSA were quite similar, which were 48% of S (CO) and 51% of S (H_2)) [65,66].	Figure. 8 Page.15

12.	Catalysts regeneration and reusability studies should be performed to evaluate the influence of coke deposition on catalyst activity.	Thank you for your comment. We have been studying the carbon impact and type of carbon through the TGA/DTA, Raman, and TEM analysis. These evaluated the carbon effect on the activity of the catalyst. **Spent Characterization** During 10 hours of activation, the Raman spectra evidenced the distinct species of carbon extant in Fig. 8. The sp2-bonded carbon deposit is responsible for two peaks: the disorder-generated band (D-band) at 1350 cm^{-1} and the graphite carbon band (G-band) at 1584 cm^{-1} [38]. The G-to-D-band ratio (IG/ID) is a representation of the amount of carbon placed, which evaluates the quantity of graphitization of coke deposits. Consequently, a higher IG/ID ratio implies that graphitic carbon is being generated at an accelerated rate more highly than amorphous carbon and inconsistently, increases the catalyst's susceptibility to deactivation and complicates the renovation process [69]. The IG/ID ratios for Co/FSA and Ni/FSA were 1.02 and 0.9, respectively, confirming both carbons, graphitic and amorphous, were attended with both specimens. Raman spectra revealed that the Ni/FSA had the lowest IG/ID ratio and narrowest band zones throughout Raman wavelengths. This indicates that a small amount of carbon is deposited on Ni/FSA, while the maximum carbon achieves an amorphous and disordered formation that has little potential for catalyst disruption. The disordered carbon formations are mainly gasified throughout the DRM, preventing them from accumulating and developing into a more stable carbon deposit. Coke coatings on the catalyst surface were evaluated using the TGA and DTA investigation, and the findings are displayed in fig.9. The charts demonstrated the weight portion loss caused by the used catalysts, the amount of carbon formed, and the volume of coke that might be replaced over the suppression mechanism of oxidation employing plenty of O_2 to form CO_2. For the Ni/FSA catalyst, the preliminary loss of weight happened at approximately 85°C and progressed at 4%. This demonstrates the carbon amorphous formation, which is recognized to oxidise at lower temperatures compared with other carbons, on the catalyst surface [70]. Observations in ancient times have proven that the size of the metal crystallization has a considerable impact on restricting carbon residue or elution, as catalysts with minimal metal crystalline phases release fewer cokes [71]. Additionally, the Raman and TGA analyses provided physical and quantifiable verification of the coke generation. Due to amorphous carbon's simpler oxidation than graphitic carbon, it had less of an impact on the catalyst's performance even after 10 hours on streams [72].	Page.16,17, 18,19

		The losing weight is particularly evident in Co/FSA, with a maximum value of peak position appearing at about 600 °C. That proves the accumulation of exceptionally carbonaceous graphitic, which is challenging to gasify on-site or rejuvenate This carbon typee has responsibility for the rapid deactivation of Co/FSA, as shown in the stability evaluation (Fig. 7). The DTG patterns can be subdivided into distinct peaks that correspond to different types of carbon and are classified by the symbols Cγ, Cβ, and Cα [73]. We utilized TGA curve discrimination to determine the varieties of carbon species that are considered the peaks in (Fig. 9B). Amorphous carbon (Cα) is oxidised at minimal temperatures to create the syngas. Whereas, at extreme temperatures, Cγ and Cβ are oxidized, and those carbon sorts are actually involved in the mechanism catalyst performance. The mass loss of roughly 100^{o}C across all specimens is assigned to C, whereas the minor peak at 550^{o}C is related to Cβ, which is presumably formed by polymerization and rearranging of active carbon species. At approximately 650 C, the weighting losses were caused by crystalline carbon C, which is crucial for catalytic inactivation [74,75]. After 10 hours of stream in the DRM reaction, the catalysts had not morphologically deformed and had sustained the FSA fibrosis as shown in fig.10. The Ni lattice fringes were discovered in the assessed quadrat space with lattice spacings of 0.18, 0.25, and 0.2 nm for the Ni/FSA specimen (Fig. 10 B) and related to Ni (200), NiO (111), and Al_3Ni (301), respectively. Moreover, the lattice area which correlated to the Co_3O_4 (111), CoO (200), and Co (100) was 0.466, 0.213, and 0.208 nm, respectively in fig .10D. The lattice spacing of carbon interplanar was nonexistent on Ni/FSA provided evidence that carbon-graphite prevention was observed. Only on Co/FSA could different lattice fringes be seen that were related to carbon graphite and nanotubes with different levels of graphitization (Fig. 9D). Fig. 10A depicts the formation of amorphous carbon that is disordered around the Ni nanoparticles. This classification of carbon was not suffered or had no deactivation for the catalyst during the reaction indicating rapid gasification through oxygen vacancy to generate extra CO. As a consequence, it was minimal potential for accumulation in a long-term DRM. Carbon formation was insignificant after 10 hours of reaction, but the carbon nanotubes (C-NTs), amorphous as well as whiskers, were visible on the spent Co/FSA, as evidenced by the TGA and Raman data. As shown in Figure 6, the apparent inactivity of Co/FSA during the early periods of the long-term reaction is caused by the steady and structural carbon deposition and the lower sintering resistance. The catalyst is more susceptible to inactivation if more graphitic carbon is generated [41,76,77].	

13.	The correlation between catalyst's physicochemical properties and catalyst's activities should be critically analyzed and discussed. What are the vital properties in ensuring the excellent performance of the catalyst? It would be interesting if the author could provide a figure of properties-activities correlation to evaluate their relationship.	Thank you for your comment. We have revised and provided more details about the correlation among properties and activities The activity of Ni/FSA was preferable over that of Co/FSA, which might be attributed to its significant number of active sites via the mesoporous and microporous supplies by the support's fibrous temple. In particular, the characterization results show that the thinner crystallite of NiO is diffused homogeneously across the FSA compared to Co. However, Co has shown in FESEM more accumulation onto the FAS than Ni, as well as the Co particles having blocked the pores of the FSA the (Table. 2). This creates a tremendous contribution to increasing NiO engagement within the FSA and drastically enhancing the environmental basicity of catalysts. As stated previously, the catalysts' basicity assisted CO_2 decomposition and gasification while limiting CH_4 interactions with active sites, potentially minimizing coke formation during the long-term activity[69,70]. Interestingly, FTIR results show that the existence of a synergic influence among Nickle particles and fibrous silica-alumina mesostructures via the generation of Ni-O-Al and Ni-O-Si bonds prevents the aggregation of metal. This coordinated impact shielded the metallic Ni^0 phase during the reduction of the NiO crystalline phase through the H_2 stream before the reaction begging, thus increasing the re-efficiency of both gaseous reactants, CH_4 and CO_2. The inferior catalytic efficacy of Co/FSA is probably attributed to the coke forming and possibly sintering metals during the DRM process [68,71].	Page.15,16
14.	Numerous language deficiencies (poor language, grammar, word choice, tense, and style of writing) are observed in the manuscript. Please thoroughly revise your manuscript with the help of a native speaker or a language editing service such as the one from Elsevier or any other agency of your choice.	Thank you for your comment. We have proofread whole the manuscript	

No. P1222211

CERTIFICATE OF PROOFREADING

THIS IS TO CERTIFY THAT THIS ARTICLE TITLED

Methane dry reforming on fibrous silica-alumina employing nanocrystals of nickel and cobalt to recognize the most efficient metal

HAS BEEN PROOFREAD BY STYLISTIC EDITORS AND PROOFREADERS

THIS IS TO CERTIFY THAT THIS ARTICLE TITLED

Official signature

29/1/2023

Date

Reviewer: 3

No.	Comment	Response to comment	Remark
1	The authors mentioned that dry reforming of methane had been recommended as a superior syngas generation. Why?	Thank you for your comment. It has been suggested that dry reforming of methane (DRM) is a preferable option to producing syngas (H_2/CO ≈1) since it can decrease CO_2 emissions while producing beneficial raw materials [2]. Since in the Fischer-Tropsch synthesis, a feedstock gas combination containing a low H_2/CO ratio is preferred for the creation of hydrocarbon fuels [6–8].	Page.4
2	The authors should discuss DRM, the process conditions that affect the yield, and why catalysts should be used in the introduction section.	Thank you for your comment. We have revised and provided the details To enhance DRM at the industrial scale, three fundamental aspects must be addressed: (1) improved carbon dioxide and methane activation; (2) the improved comprehension of the mechanisms and reaction processes that create H_2 and CO; and (3) strategies to prevent deactivation of catalyst operations [4,5].	Page.4
3	what is the role of oxygen in the activity of the catalyst	Thank you for your comment. We have revised and provided the details The majority of the recent investigations in this area are primarily focused on reducing carbon creation in a variety of methods, either by ; i) using supports that have high oxygen ion mobility which may interact with adsorbed carbon species[21–25] Thus, the Ni/ FSA possesses high oxygen storage caused by the extraordinary surface area to which oxidizing the C to CO thereby forming intermediates carbonate species into reductive basic supports reflected avoiding the coke formation [28].	Page.5 Page.14

4	Why were NiO crystallite dispersion and sizes visible across the support framework? Was the catalyst reduced?	Thank you for your comment we have more clarity. We have revised and provided the details This possibly is owing to the Ni/FSA catalyst possessing a greater capacity to disperse oxygen species over the surface than Co/FSA catalyst [18,19,63].	Page.15
5	Quantitative and important findings should be emphasised in the highlights	Thank you for your comment. We have revised and rewritten it. **Research highlights** • The small Ni particles resist the coke aggregation • The oxygen capacity of the supports inhibits coke formation • Active sites in dendritic fibrous are easily accessible • The catalytic activity is dependent on the metal-support interaction • Carbon nanotubes influence the catalytic activity	Highlights

Research highlights

- The small Ni particles resist the coke aggregation
- The oxygen capacity of the supports inhibits coke formation
- Active sites in dendritic fibrous are easily accessible
- The catalytic activity is dependent on the metal-support interaction
- Carbon nanotubes influence the catalytic activity

Methane dry reforming on fibrous silica-alumina employing nanocrystals of nickel and cobalt to recognize the most efficient metal

A.H.K. Owgi [b], A.A. Jalil [a, b, c*], M.A.A. Aziz[a, b], W. Nabgan [d], M. Alhassan [b,f], M.H.M. Sofi [b], N.S. Hassan [b], R. Saravanan [e], M. B. Bahari [b].

[a] *Centre of Hydrogen Energy, Institute of Future Energy, 81310 UTM Johor Bahru, Johor.*

[b] *Faculty of Chemical and Energy Engineering, Faculty of Engineering, Universiti Teknologi Malaysia, 81310 UTM Johor Bahru, Johor, Malaysia.*

[c] *Saveetha School of Engineering, Saveetha Institute of Medical and Technical Science, Chennai 60210, India*

[d] *Departament d'Enginyeria Qu´ımica, Universitat Rovira I Virgili, Av Pa¨ısos Catalans 26, 43007, Tarragona, Spain.*

[e] *Faculty of Engineering, Department of Mechanical Engineering, University of Tarapacá, Avda, General Velasquez, 1775 Arica, Chile.*

[f] *Department of Chemistry, Sokoto State University, PMB 2134, Airport Road, Sokoto, Nigeria*

**To whom correspondence should be addressed,*

Aishah Abdul Jalil (Ph.D.)

Tel: 60-7-5535581 Fax: 60-7-5536165

Email: aishahaj@utm.my

Abbreviation.

(GHGs):	Greenhouse gas.
(DRM):	Dry reforming of methane.
(FSA):	Fibrous silica-alumina.
(CTAB):	Cetrimonium bromide.
(TEOS):	Tetraethyl orthosilicate.
(XRD):	X-ray diffractograms.
(XRF):	X-ray fluorescence
(FESEM):	Field emission scanning electron microscopy.
(FTIR):	Fourier-transform infrared.
(TEM):	Transmission electron microscopy.
(H_2-TPR):	H_2 temperature program reduction.
(TGA):	Thermogravimetric analysis.
(GC):	Gas chromatography.
(BET):	Brunauer-Emmett-Teller.
(C-NTs):	Carbon nanotubes
(D-band):	Disorder-generated band
(G-band):	Graphite carbon band
(TCD):	Thermal conductivity detector
(NLDFT):	Non-local density functional theory
(TO):	Transverse-optical
(LO):	Longitudinal-optical

ABSTRACT

Presently, the production of syngas through the dry reforming of methane is a widely employed approach for reducing vast amounts of greenhouse gas emissions. Several metals, particularly transition metals support have been evaluated as active DRM catalyst systems. In this work, a comparative studies is presented between Cobalt and Nickel metals impregnated over fibrous silica-alumina (FSA) support synthesized by the hydrothermal method for dry methane reforming. The specimens were characterized via FESEM mapping, TEM, XRD, H_2-TPR, XRF, N_2 physisorption, and KBr-FTIR techniques. Unlike the Co/FSA, Ni/FSA displayed a higher surface area with a fine dispersion of Ni nano-crystalline and less agglomeration, and more active sites which enhanced the metal-support interaction. Approximately 0.2g of each catalyst was evaluated at 650 - 800 ºC with a respective. CH_4:CO_2:N_2 ratio of 1:1:2, gas hourly space velocity 30,000 mL g^{-1} h^{-1}. The Ni/FSA demonstrated more conversion of CH_4 (89%) over (67%) of Co/FSA at 800ºC. After 10 h of long-term reaction, the Ni/FSA exhibited more stability at 800 ºC. TGA/DTA, Raman, and TEM results showed that spent Ni/FSA catalysts did not demonstrate signs of considerable nano-graphitic carbon or metal sintering as compared to Co/FSA catalysts, which had bigger crystallites of Co. The finding of this study would add new knowledge on reaction conditions involving and catalytic activities of the metals over the FSA.

Keywords: cobalt, nickel; carbon resistance; methane dry reforming; Fibrous silica-alumina.

1.0 Introduction

In recent years, there has been a great deal of interest in the dry reforming of methane, which is the conversion of the major negative component of fossil fuel emissions, (CO_2 and CH_4), which is pose a serious environmental issue into synthesis gas with an H_2/CO ratio of unity, which is used to produce synthetic fuel [1–3]. This procedure is incredibly significant to the environment as the GHGs utilized as gas sources are methane and carbon dioxide, all of which are harmful greenhouse gases. It has been suggested that dry reforming of methane (DRM) is a preferable option to producing syngas (H_2/CO≈1) since it can decrease CO_2 emissions while producing beneficial raw materials [2]. To enhance DRM at the industrial scale, three fundamental aspects must be addressed: (1) improved carbon dioxide and methane activation; (2) the improved comprehension of the mechanisms and reaction processes that create H_2 and CO; and (3) strategies to prevent deactivation of catalyst operations [4,5].

In the Fischer-Tropsch synthesis, a feedstock gas combination containing a low H_2/CO ratio is preferred for the creation of hydrocarbon fuels [6–8]. To achieve appropriate conversion levels, the endothermic aspect of the reaction necessitates a high reaction temperature. Because of the considerable operational temperature, adequate catalysts are required. The creation and build-up of carbonaceous deposits typically lead to the sintering of metal particles followed by the deactivation of catalysts as a consequence of the excessive temperature [9–13]. Recently, it is proven that noble metals including platinum, rhodium, and ruthenium, as well as non-noble metals as transaction metals (Ni, Co, and Fe), are employable as catalysts in dry reforming processes[9,10]. According to reports, noble metals possess excellent catalytic activity and have insignificant coking potential. However, due to their restricted variety and expensive cost, they are not widely used in the industrial sector.

Because of their cheaper cost and equivalent catalytic efficiency, non-noble metals such as nickel and cobalt have attracted the curiosity of researchers [4,14–16].

Despite the great catalytic performance demonstrated by nickel-based catalysts, the significant coking and swift inactivation prevent them from being used in industrial applications. Cobalt catalysts for example, possess a considerable soot oxidation ability which could be employed to increase the resistance of a catalytic process to carbon production by reducing the coke formation. Nonetheless, cobalt catalysts exhibit a high proclivity for re-oxidation, resulting in low performance [17–20].

The majority of the recent investigations in this area are primarily focused on reducing carbon creation in a variety of methods, either by ; i) using supports that have high oxygen ion mobility which may interact with adsorbed carbon species, such as SiO_2, CeO_2, and ZrO_2 solid solutions, as opposed to conventional supports[21–25]; ii) the employment of additives such as potassium or sodium, which provide basic aspects to the surface characteristics, despite the reality that they reduce the catalytic activity[26,27]. iii) modifying the morphologies of support specifically bimodal, mesoporous, nanorods, core-shell, nano-fibrate, and fibrous dendrimers [28–34]. The fabrication of incredibly multifunctional supported metal catalysts by wide metal dispersion of nanoparticles is one of the crucial options for heterogeneous catalytic systems that require research. Our prior research on the successful growth of fibrous silica-alumina (FSA) via exceptional surface area and thermal stability was the inspiration for this study [35]. In the present study, the FSA was investigated for DRM and the performance of the metals (Ni and Co) loaded over FSA aiming at getting a greater understanding of the metal's impact on catalytic efficiency and carbon formation.

2.0 Experimental

2.1 Catalyst Preparation

Fibrous silica-alumina support has been generated through the hydrothermal method and Al_2O_3. Alumina nitrate (Sigma-Aldrich, > 98%) was combined into a homogenous mixture of n-butanol (Merck, > 98%) and toluene (Sigma-Aldrich, > 98%). Afterward, the solution was stirred for approximately 30 min prior to introducing TEOS (Merck, > 98%) and was poured dropwise. Urea (Merck, > 98%), Cetrimonium bromide (CTAB- Sigma-Aldrich, > 98%), and 0.75 L of deionized water were added to the mixture. Toluene/1-butanol=13.8, urea/CTAB=3.8, and Si/Al=1.23 are the essential variables. While being exposed to microwave radiation at 400 W for 360 min, the subject substance was vaporized at 120 ℃ for overnight evaporation. The white specimen was heated in a furnace for 360 min at 550 C to produce FSA support.

2.2 Loading Metals

To load metals onto FSA, a 5 wt% Co and Ni-impregnated solution of $Co(NO_3)_2$ and Ni $(NO_3)_{2.6}H_2O$ were (% trace metals) used as purchased from Sigma-Aldrich. Bhd. They dissolved in deionized water was deployed. Before getting impregnated, the specimens were evaporatively dried and then calcined for three hours at 550 °C. Co/FSA and Ni/FSA were the end products of this procedure.

2.2 Characterization

A Bruker D8 Advance diffraction pattern, Which was certified utilizing Cu K-ray radiation at 1.54 wavelengths, was employed to conduct the XRD study on pristine and spent samples. The determination is intended to generate X-ray diffractograms in the range of 1-280º employing data at 0.05º and 0.1º at 46kV and 41mA. (FESEM; Zeiss Supra VP35) field emission scanning electron microscopy was deployed to further analyze the structure of samples. N_2 adsorption-desorption through ASAP2020 apparatus was using an N_2/He mixed gas and a from Micromeritics to determine surface areas. 0.1– 0.15 g of the specimen were refluxed at 200 °C for 240 min before the assessment, followed cooled to room temperature. The BET technique was employed to calculate the total surface area. Additionally, Fourier-transform infrared (FTIR) measurements were conducted on the materials using the Agilent Technology Varian 670 apparatus at 30 ℃ in the 400 to 4000 cm^{-1} wavelength range. By using a Rigaku Primus 2 apparatus and lithium tetraborate to treat the materials, the metal percentage was evaluated using wavelength-dispersive X-ray fluorescence (XRF).

The carbon-containing aggregate structuring in the utilized catalysts was examined by adopting 510nm lasers with a 50x magnified microscope mounted on a Renishaw via a Raman spectrophotometer, The Raman spectra of the specimen were recorded around 1000 and 2200 cm^{-1}. A TGA/SDTA 851e Mettler Toledo thermo-gravimetric instrument with a temperature range of 5-950 ℃ and a heating rise of 10 ℃/min with airflow has also been employed to assess carbon deposits. Additionally, utilizing JEOL JEM-2100 F technology, transmission electron microscopy (TEM) was conducted on the spent samples. All of the materials were acetone-liquefied before being positioned on a copper gridiron that had a penetrable carbon layer covering it. Temperatures of 100 to 1000℃ and an H_2/N_2 flow rate with a concentration of 10% were employed to investigate the reduced specimen (20 mL min^{-1}).

2.3 Catalyst assessment

The DRM assessments were carried out on various catalysts using a series of efficiency measurements at a temperature limitation of 500-850 ℃ through streaming the gases in a fixed-bed reactor to identify the detrimental impacts of the metals on the long-term catalyst performance. The catalysts were tested employing a stream running continuously in a reactor at environmental pressure and a heat range of 500–850 ºC. A portion of the pelletized catalyst (2mg) was placed in a reactor, blocked by quartz wool. Before the activity, the preload catalyst was initially treated with 15 mL min^{-1} oxygen at 700 ℃ for 60 min, followed by 100 $ml.min^{-1}$ at 800 ºC throughout 120 min of H_2:N_2 (50:50). Then the reactor was cooled to a set temperature as a function of the impacts of N_2. The reactor was supplied with the mixture of gases CO_2: CH_4: N_2 at 25:25:50 $ml.min^{-1}$ rate. To continuously monitor and evaluate the surplus reactant and gas released, (Agilent 7890A GC) a gas chromatograph set via a (1010)column carboxy with a 0.1L collecting band with thermal detecting was employed (TCD). Before a randomized choice was determined, 60 minutes were required for reaching the reaction equilibrium at the examined temperature. Equations (1-7) were employed to estimate the rate of conversions and the ratio of syngas (H_2/CO) [9,36,37].

Conversion of CH_4 $= \frac{F_{(CH4)in} - F_{(CH4)out}}{F_{(CH4)in}} \times 100$ (1)

Conversion of CO_2 $= \frac{F_{(CO2)in} - F_{(CO2)out}}{F_{(CO2)in}} \times 100$ (2)

H_2/CO $= \frac{F(H_2)out}{F\ (CO)out}$ (3)

H_2 Selectivity $= \frac{F_{(H2)out}}{2\ [\ F_{(CH4)in} - F_{(CH4)out}]} \times 100$ (4)

CO Selectivity $= \frac{F_{(CO)out}}{[\ F_{(CH4)in} - F_{(CH4)out}] + [\ F_{(CO2)in} - F_{(CO2)out}]} \times 100$ (5)

H_2 Yield $= \frac{F(H_2)out}{2 \times F\ (CH)4in}$ (6)

CO Yield $= \frac{F_{(CO)out}}{F_{(CH4)in} - F_{(C02)in}} \times 100$ (7)

3.0 Reflection on The Findings

3.1 Catalysts characterization

3.1.1 Characteristics of structure and morphology

Figure 1(A–C) displays FESEM micrographs including elements mapping of all specimens demonstrating the particle dispersion of metal. Figures 1(A) depict the creation of the fibrous silica-alumina structure's expected spherical bi-continuous concentric fibrillar shape. NiO and CoO crystallite scattering and sizes were soft purple spots evident scattered over the support structure. The particle sizes, as determined from the XRD spectra using the Scherrer equation, are 11.7nm and 14.3nm for Ni and Co FSA catalysts respectively. For this reason, the Co is less spread on the surface of the FSA than Ni/FSA [38]. The Co was inadequately diffused on the fibrous silica-alumina (Fig. 1C), due to its limited pores as well

as surface area, as shown by the lumps of Co on the surface of the FSA after impregnation. This being the cause of rapid Co/ FSA inactivation during only short hours on the stream cannot be outweighed. Because of the limited distribution of Co, there is a limited surface for reaction and reduction, resulting in significant sintering due to tiny crystallite migration. Consequently, the deactivation potential of the catalyst will be larger based on the amount of carbon placed [5,12,39]. Moreover, Traces of cobalt and nickel were observed via catalysts are 5.10% and 4.84% respectively by XRF analysis (in the Table.1), The amounts of Ni-loading at 5% wt are consistent with the quantities employed during catalyst preparations, and the identifying amounts of compounds utilized in this investigation are true.

Figure .2. displays the crystalline structures through the X-ray diffraction (XRD) for the specimens FSA, Ni/FSA, and Co/FSA. All the samples demonstrated a broad 2θ band from 20 to 30º, this is often attributed to the amorphous phase of SiO_2 (JCPDS card No. 29-0085)[40,41]. Because of the existence of silica species during the fabrication of dendrimeric silica fibres, the XRD pattern intensity diminished. The Ni and Co FSA catalysts both exhibited nine prominent peaks at 2θ value of 25.8°, 35.4°, 37.8°, 43.5°, 52.8°, 57.5°, 66.7°, 68.4°, and 77.1° identical to the (0 1 2), (1 0 4), (1 1 0), (1 1 3), (0 2 4), (1 1 6), (2 1 4), (3 00), and (1 1 9) alumina crystalline planes via structures of rhombohedral (JCPDSICDD File No 46-1212) for FSA sample [35,42].

Three diffraction peaks were seen for NiO via Ni/FSA at 2θ = 62.9, 75.4, and 79.4°, correlating to NiO planes (2 20), (2 2 2), and (3 1 1), respectively (JCPDS 78-0643). The Co_3O_4, Co/FSA showed five peaks at 2θ = 18.6, 31.3, 36.8, 44.8, and 59.4°, which corresponded to (111), (2 2 0), (3 1 1), (4 0 0), and (511), respectively (JCPDS 42-1467)[43]. The diffraction peak intensity was found to be lower in Ni/FSA in comparison to Co/FSA. As revealed by the FESEM studies; moreover, the nano-crystallite metals of NiO deposited on FSA were uniformly distributed more than Co_3O_4. Owing to the active site mobility

obtainable through FSA, which enables NiO scattering, the possibility for NiO crystal aggregation and the metal-support interaction is increased [44]. Moreover, the peaks of Ni-Al_2O_4 appeared less higher than that of Co-Al_2O_4 indicating more crystallinity of Co over Ni

3.1.2 Textural properties

N_2 adsorption-desorption analysis was used to investigate the textural properties of the FSA, Ni/FSA, and Co/FSA. Figure.3 shows the N_2 adsorption-desorption isotherms including pore size dispersion of the catalysts. Referring to the IUPAC categorization, the catalyst isotherms displayed regular type IV adsorption phases at P/Po = 0.4, and 0.9, indicating a mesoporous property [45,46]. The scattering of pore sizes overall catalysts is illustrated in the figure.3 implementing (NLDFT) non-local density functional theory.

The FSA revealed a sharp peak in the 50-70 (Å) range and a thin peak in the 100-200 (Å) band for mesopore distribution. The high peak is due to the formation of mesopores during surfactant self-assembly. However, the small peaks are owing to the spacing between dendrimeric molecules. When Ni/FSA was compared to FSA, there was no substantial shift in pore dispersion. This attests to a real dispersion of Ni dispersion confirmed by FESEM (Fig. 1). However, the peak intensity of pore dispersion is decreased by adding Co. This finding is linked to a decrease in the amount of adsorbed N_2 in Co/FSA P/Po = 0.46–1.0, indicating a decrease in micropores and interparticle voids mesopores[47]. In the present study (Table.2), the FSA displayed (334.92 $m^2\ g^{-1}$) an extraordinary surface area, after loading Ni, the surface area increased to 338.54 $m^2\ g^{-1}$ because there was more scattering of active metal [48]. Moreover, increased Ni encasement over Ni/FSA indicates that dispersion has been optimized. As seen in figure 1. However, when Co was added to the FSA, the surface area and pore volume were reduced to 303.6 $m^2\ g^{-1}$ and 0.856 $cm^3\ g^{-1}$ respectively.

With the addition of Co, the catalysts' surface area and pore volume diminished due to partial pore blockage and/or pore filling.

3.1.3 Reducibility

TPR-H_2 of the calcined catalysts was performed to gain a deeper insight into the evolution of the nickel and cobalt phases as shown in figure.4. This was useful in determining the reduction degree of the Co and Ni oxide species. the solitary peak of Ni/FSA in the region from 260 ºC to 360 ºC correlates to Ni species reduction [49,50]. This is most definitely attributable to a reduction in narrower NiO nanoparticles or nickel aluminates as shown in the XRD result [44,49]. A low degree of reduction peak might imply that the interaction of NiOx species was slight with the exterior of FSA dendritic fibres.

There were two essential reduction stages in the Co/FSA catalyst's reduction studies. The reduction peak centred close to 300-510 ºC is assigned to free Co_3O_4 reduction.However, this involved consecutive reductions to CoO and metallic Co, respectively. A unique peak was identified between 560 and 770 ºC showing the occurrence of considerable quantities of $CoAl_2O_4$ obtained from the strong interaction between Co_3O_4 and Al_2O_3 [12,17,43,51].

3.1.4 Spectroscopic Studies

FTIR spectroscopy with wavelengths between 400 and 4000 cm-1, assessed the various construction heterogeneity of the (Co and Ni) supported FSA, as displyed in figure.5. The most prominent peaks exhibited siliceous frames because Si interacted with various atoms, (for instance, Si-O-Si, Si-OH, Si-O, Al-O-Al, and Si-O-Al) through the range 400–1300 cm^{-1}. [52]. The wavenumbers of five peaks 1240, 1090, 960, 790, also 460 cm^{-1} were demonstrated in all specimens, indicative of Si-O-Si bond apparent within the range of 960-1260 cm^{-1} in all samples [53]. Similar, all catalysts in fig.5 demonstrated a peak at 3400 cm^{-1} indicative of that O-H-stretching vibration due to water molecules, or Brønsted acid sites

which are dependent on hydrogen concentration [54,55]. As displayed by the same figure, Ni/FSA possess a low-intensity peak at 3400 cm^{-1} reflected in low Brønsted acid sites. Furthermore, asymmetric stretching peak attributed to Si-O-Si transverse-optical (TO) and longitudinal-optical (LO) bands were apparent at approximately 1240 cm^{-1} and 1090 cm^{-1}, respectively [56–58]. The weak bands at 960 and 1640 cm^{-1} were assigned to external groups of Si-OH, whilst symmetric and asymmetric Al-O and Si-O stretch vibrations were pronounce at 800 cm^{-1} and 462 cm^{-1}, respectively [59]. Apart from stretching vibrations, symmetrical and asymmetrical stretch attributable to Si-O-Al were reported by [60] 1090, 790 and 460 cm^{-1} .The disappearance of these peaks upon the introduction of Ni and Co to FSA, could imply that the Si–O–Si and Si-OH were partly replaced by Ni–O–Si, Co–O–Si, Ni-O, and Co–O. In particular, the peak at 666 cm^{-1} in the Co/FSA is attributable to Co–O vibrations indicating the successful incorporation of Co onto the support [17,41]. Accordingly, substituting result of the O–H and O–Si with the Ni ions in the dendritic fibrous FSA structure entails a greater reduction in peak density compared to the Co sample, emphasizing that Ni had a more robust interaction with FSA support than the Co [61,62].

3.2 Activity Evaluation

Figure.6 shows the activity results of Ni/FSA and Co/FSA. Ni/FSA converted more CH_4 than Co/FSA under identical reaction conditions. Based on the fine Ni dispersion as seen in the FESEM picture, Ni/FSA catalysts were more efficient than Co/FSA catalysts, which enhanced the porosity and surface area, thereby providing a variety of active reaction sites and mobility of reactant mass in the process. Additionally, textural characteristics have a significant role in catalytic activity, as demonstrated by the FSA characteristics that supply the active species required to prevent deactivation of the catalyst (surface area, pore size, and

pore volume) [63]. Thus, owing to the extraordinary surface area of Ni/ FSA and possession of high oxygen storage deposits of C are easily transformed to CO thereby forming intermediates carbonate species into reductive basic supports reflected avoiding the coke formation [28].

The Ni/FSA catalyst shows superior catalytic efficacy, with the sustained conversion of CH_4 and CO_2 exceeding 89 % and 80 %, respectively, at 800 ºC, In comparison to Co/FSA (XCH_4= 67%, XCO_2 63%). Indeed, the tiny metal particles and superior metal diffusion will lead to more edges and metal-support frameworks, resulting in more active sites. Interestingly, the conversion of CH_4 and CO_2 at 700 were similar for the Ni/FSA and Co/FSA catalysts, indicating the possibility that side reactions such as; methane decomposition ($CH_4 \rightarrow C + 2H_2$) and the Boudouard reaction ($2CO \leftrightarrow C + CO_2$) have occurred [7,64].

To verify the successful Ni/FSA synthesis for DRM catalytic ability in comparison to the Co/FSA at 800 °C prolonged performance for 10 hours, the stabilization assessments were carried out as shown in fig.7 (A and B). Compared to Co/FSA (XCO_2 = 17%, XCH_4 = 21%), the FSA catalyst exhibits superior catalytic performance, with the stable CO_2 conversion and CH_4 achieving 91 % and 96 %, respectively. The catalytic performance of Co/FSA decreases during the second hour while on stream. This should be identified by the poor Co dispersion within surface aggregation and increased acidity that causes coke deposit and inactivation [28,51]. Moreover, the H_2/CO ratio for Co/FSA is lesser than that of Ni/FSA, achieving a ratio of 0.85 to 95 as depicted in Fig. 7C, which is appropriate for the Fischer-Tropsch application to synthesize lipid long hydrocarbons chain. This possibly is owing to the possibility of Ni/FSA to disperse oxygen species over the surface than Co/FSA catalyst [18,19,63]. According to Fig. 8, the H_2 yield showed a different trend with conversions, with Ni/FSA achieving the highest H_2 yields and Co/FSA achieving the lowest. Meanwhile, the exception of CO selectivity that appeared to be caused by the Co/FSA

catalyst could be explained by the RWGS reaction ($CO_2 + H_2 \leftrightarrow CO + H_2O$). where the H_2 and CO selectivity of Ni/FSA were quite similar, which were 48% of S (CO) and 51% of S (H_2) [65,66].

Simultaneous secondary reactions that occurred throughout catalytic testing were predictable. On the other hand, from the H_2/CO profiles as displayed in Fig. 7C, In actuality, a rise in the ratio of syngas on Ni/FSA after 6 hours was driven by the concomitant occurrence of CH_4 decomposition ($CH_4 \rightarrow C + 2H_2$) and CO disproportionation ($2CO \leftrightarrow C + CO_2$). These subsequent reactions neither simply influenced the syngas ratio, but also produced carbonaceous species that were detrimental to catalytic activity. On the contrary, in the first hours of the reaction, the syngas ratio was shown to drop for both specimens, which was caused by the reverse water gas shift (RWGS) reaction to the decrease in syngas ratio. and seem to improve with the favourability of thermodynamics [67,68].

The activity of Ni/FSA was preferable over that of Co/FSA, which might be attributed to its significant number of active sites via the mesoporous and microporous supplies by the support's fibrous temple. In particular, the characterization results show that the thinner crystallite of NiO is diffused homogeneously across the FSA compared to Co. However, Co has shown in FESEM more accumulation onto the FAS than Ni, as well as the Co particles having blocked the pores of the FSA the (Table. 2). This creates a tremendous contribution to increasing NiO engagement within the FSA and drastically enhancing the environmental basicity of catalysts. As stated previously, the catalysts' basicity assisted CO_2 decomposition and gasification while limiting CH_4 interactions with active sites, potentially minimizing coke formation during the long-term activity[69,70].

Interestingly, FTIR results show that the existence of a synergic influence among Nickle particles and fibrous silica-alumina mesostructures via the generation of Ni-O-Al and

Ni-O-Si bonds prevents the aggregation of metal. This coordinated impact shielded the metallic Ni^0 phase during the reduction of the NiO crystalline phase through the H_2 stream before the reaction begging, thus increasing the re-efficiency of both gaseous reactants, CH_4 and CO_2. The inferior catalytic efficacy of Co/FSA is probably attributed to the coke forming and possibly sintering metals during the DRM process [68,71].

3.3 Spent Characterization

During 10 hours of activation, the Raman spectra evidenced the distinct species of carbon extent in Fig. 9. The sp2-bonded carbon deposit is responsible for two peaks: the disorder-generated band (D-band) at 1350 cm^{-1} and the graphite carbon band (G-band) at 1584 cm^{-1} [38]. The G-to-D-band ratio (IG/ID) is a representation of the amount of carbon placed, which evaluates the quantity of graphitization of coke deposits. Consequently, a higher IG/ID ratio implies that graphitic carbon is being generated at an accelerated rate more highly than amorphous carbon and inconsistently, increases the catalyst's susceptibility to deactivation and complicates the renovation process [72]. The IG/ID ratios for Co/FSA and Ni/FSA were 1.02 and 0.9, respectively, confirming both carbons, graphitic and amorphous, were attended with both specimens. Raman spectra revealed that the Ni/FSA had the lowest IG/ID ratio and narrowest band zones throughout Raman wavelengths. This indicates that a small amount of carbon is deposited on Ni/FSA, while the maximum carbon achieves an amorphous and disordered formation that has little potential for catalyst disruption. The disordered carbon formations are mainly gasified throughout the DRM, preventing them from accumulating and developing into a more stable carbon deposit.

Coke coatings on the catalyst surface were evaluated using the TGA and DTA investigation, and the findings are displayed in Fig.10. The charts demonstrated the weight portion loss caused by the used catalysts, the amount of carbon formed, and the volume of

coke that might be replaced over the suppression mechanism of oxidation employing plenty of O_2 to form CO_2. For the Ni/FSA catalyst, the preliminary loss of weight happened at approximately 85°C and progressed at 4%. This demonstrates the formation of amorphous crbon, which is recognized to oxidize at lower temperatures compared to other carbons deposits, on the catalyst surface [73]. Observations in ancient times have proven that the size of the metal crystallization has a considerable impact on restricting carbon residue or elution, as catalysts with minimal metal crystalline phases release fewer cokes [74]. Additionally, the Raman and TGA analyses provided physical and quantifiable verification of the coke generation. The ease of oxidation exhibited by amorphous carbon over graphitic one made its impact after 10h on stream lesser [75]. On the contrary, the loss of weight particularly evident in Co/FSA, with a maximum value of peak position appearing at about 600 °C confirms the accumulation of exceptionally carbonaceous graphitic, which is challenging to gasify on-site. This carbon type has responsible for the rapid deactivation of Co/FSA, as shown by the stability evaluation (Fig. 7).

The DTG patterns can be subdivided into distinct peaks correspond to different types of carbon and are classes dignifed by the symbols Cγ, Cβ, and Cα [76]. The TGA profile was utilized to differentiate varieties in (Fig. 10B). Amorphous carbon (Cα) is oxidized at minimal temperatures to produce the syngas. Whereas, at extreme temperatures, Cγ and Cβ are oxidized, and those carbon sorts are actually involved in the mechanism of catalyst performance. The mass loss of roughly 100^{o}C recorded across all specimens is assigned to C, whereas the minor peak at 550^{o}C is related to Cβ, which is presumably formed by polymerization and rearrangement of active carbon species. At approximately 650 C, the weight losses were caused by crystalline carbon C, which is crucial for catalytic inactivation [77,78].

After 10 hours time on stream, the catalysts had not morphologically deformed and had sustained the FSA fibrosis (as shown in Fig.11). The Ni lattice fringes were discovered in the assessed quadrat space with lattice spacings of 0.18, 0.25, and 0.2 nm for the Ni/FSA specimen (Fig. 11B) and related to Ni (200), NiO (111), and Al_3Ni (301), respectively. Moreover, the lattice area which correlated to the Co_3O_4 (111), CoO (200), and Co (100) was 0.466, 0.213, and 0.208 nm, respectively in fig .11D. The lattice spacing of carbon interplanar was nonexistent on Ni/FSA provided evidence that carbon-graphite prevention was observed. Only on Co/FSA could different lattice fringes be seen that were related to carbon graphite and nanotubes with different levels of graphitization (Fig. 9D).

The formation of amorphous carbon disordered around the Ni nanoparticles is depicted (Fig.11A). The reaction indicated rapid gasification through oxygen vacancy to generate excess CO with no deactivation by coking. Consequently, it had minimal potential for accumulation in a long-term activity. Although the coke formation was insignificant after 10 hours of reaction, but the carbon nanotubes (C-NTs), whiskers, as well as amorphous coke species were visible on the spent Co/FSA, as evidenced by the TGA and Raman data. As shown in Figure 6, the apparent inactivity of Co/FSA during the early periods of the long-term reaction could be caused by the steady and structural carbon deposition and its lower sintering resistance as catalysts are more prone to inactivation if apprecible graphitic carbon is generated [41,79,80].

4.0 Conclusion

To conclude, fibrous silica-alumina (FSA) has been synthesized through the hydrothermal method with various loading metals by the impregnation method. In the KBr-FTIR and H_2-TPR investigations, the appearance of the degree of metal interactions was conditional on metal dispersion attributed to metal crystallite size on the support surface.

Accordingly, Ni/FSA generated superlative function in the DRM reaction across a temperature range of 500–850 °C and extraordinary stability over 10 h it due to its a large surface area (338.56 m^2/g), fine size dispersion of Ni, and strong metal-support interaction, as well as strong resistance to sintering by restricting Ni atoms or crystallite movements on the support. However, Co/FSA had a bigger crystallinite size, which affects the metal-support interaction reflected in the performance of the catalyst. The Ni/FSA catalyst serves as a coke inhibitor and a disordered amorphous phase with no effect on the catalyst stability. These characteristics are the vital causes for Ni/FSA catalyst's superior efficiency to Co/FSA synthesized via wet impregnation. As documented, the conversion of CH_4 was 97.5% for Ni/FSA, while it dramatically dropped to 20.63% for Co/FSA

Acknowledgment

The High Impact Research (UTMHR) Grant from Universiti Teknologi Malaysia funded this research project (08G92).

Reference

[1] Arbag H, Yasyerli S, Yasyerli N, Dogu G. Activity and stability enhancement of Ni-MCM-41 catalysts by Rh incorporation for hydrogen from dry reforming of methane. Int J Hydrogen Energy 2010;35:2296–304. https://doi.org/10.1016/j.ijhydene.2009.12.109.

[2] Gallego GS, Marín JG, Batiot-Dupeyrat C, Barrault J, Mondragón F. Influence of Pr and Ce in dry methane reforming catalysts produced from La1-xAxNiO3-δ perovskites. Appl Catal A Gen 2009;369:97–103. https://doi.org/10.1016/j.apcata.2009.09.004.

[3] Chong CC, Owgi AHK, Ainirazali N, Chin SY, Setiabudi HD. CO2 reforming of CH4 over Ni/SBA-15 prepared by surfactant-assisted impregnation method: Comparative study of surfactant types. Mater Today Proc 2018;5:21644–51. https://doi.org/10.1016/j.matpr.2018.07.014.

[4] Liu Z, Grinter DC, Lustemberg PG, Nguyen- Phan T, Zhou Y, Luo S, et al. Dry Reforming of Methane on a Highly- Active Ni- CeO 2 Catalyst: Effects of Metal- Support Interactions on C−H Bond Breaking . Angewandte Chemie 2016;128:7581–5. https://doi.org/10.1002/ange.201602489.

[5] Aramouni NAK, Touma JG, Tarboush BA, Zeaiter J, Ahmad MN. Catalyst design for dry reforming of methane: Analysis review. Renewable and Sustainable Energy Reviews 2018;82:2570–85. https://doi.org/10.1016/j.rser.2017.09.076.

[6] Takanabe K, Nagaoka K, Nariai K, Aika KI. Influence of reduction temperature on the catalytic behavior of Co/TiO 2 catalysts for CH4/CO2 reforming and its relation with titania bulk crystal structure. J Catal 2005;230:75–85. https://doi.org/10.1016/j.jcat.2004.11.005.

[7] Takanabe K, Nagaoka K, Nariai K, Aika KI. Titania-supported cobalt and nickel bimetallic catalysts for carbon dioxide reforming of methane. J Catal 2005;232:268–75. https://doi.org/10.1016/j.jcat.2005.03.011.

[8] Ruckenstein E, Wang HY. Carbon deposition and catalytic deactivation during CO2 reforming of CH4 over Co/γ -Al2O3 catalysts. J Catal 2002;205:289–93. https://doi.org/10.1006/jcat.2001.3458.

[9] Therdthianwong S, Therdthianwong A, Siangchin C, Yongprapat S. Synthesis gas production from dry reforming of methane over Ni/Al2O3 stabilized by ZrO2. Int J Hydrogen Energy 2008;33:991–9. https://doi.org/10.1016/j.ijhydene.2007.11.029.

[10] Gao J, Hou Z, Guo J, Zhu Y, Zheng X. Catalytic conversion of methane and CO2 to synthesis gas over a La2O3-modified SiO2 supported Ni catalyst in fluidized-bed reactor. Catal Today 2008;131:278–84. https://doi.org/10.1016/j.cattod.2007.10.019.

[11] Hambali HU, Jalil AA, Abdulrasheed AA, Siang TJ, Owgi AHK, Aziz FFA. CO2 reforming of methane over Ta-promoted Ni/ZSM-5 fibre-like catalyst: Insights on

deactivation behavior and optimization using response surface methodology (RSM). Chem Eng Sci 2021;231. https://doi.org/10.1016/j.ces.2020.116320.

[12] Fatah NAA, Jalil AA, Triwahyono S, Yusof N, Mamat CR, Izan SM, et al. Favored hydrogenation of linear carbon monoxide over cobalt loaded on fibrous silica KCC-1. Int J Hydrogen Energy 2020;45:9522–34. https://doi.org/10.1016/j.ijhydene.2020.01.144.

[13] Tran NT, van Le Q, van Cuong N, Nguyen TD, Huy Phuc NH, Phuong PTT, et al. La-doped cobalt supported on mesoporous alumina catalysts for improved methane dry reforming and coke mitigation. Journal of the Energy Institute 2020:1–10. https://doi.org/10.1016/j.joei.2020.01.019.

[14] Shiju NR. The Role of Metal-Support Bonding in Controlling the Particle Size of Ceria-Supported Transition Metal Catalysts. ChemCatChem 2011;3:112–4. https://doi.org/10.1002/cctc.201000357.

[15] Wang F, Xu L, Zhang J, Zhao Y, Li H, Li HX, et al. Tuning the metal-support interaction in catalysts for highly efficient methane dry reforming reaction. Appl Catal B 2016;180:511–20. https://doi.org/10.1016/j.apcatb.2015.07.001.

[16] Ruckenstein E, Hu YH. Carbon dioxide reforming of methane over nickel/alkaline earth metal oxide catalysts. Appl Catal A Gen 1995;133:149–61. https://doi.org/10.1016/0926-860X(95)00201-4.

[17] Xu J, Zhou W, Li Z, Wang J, Ma J. Biogas reforming for hydrogen production over nickel and cobalt bimetallic catalysts. Int J Hydrogen Energy 2009;34:6646–54. https://doi.org/10.1016/j.ijhydene.2009.06.038.

[18] San-José-Alonso D, Juan-Juan J, Illán-Gómez MJ, Román-Martínez MC. Ni, Co and bimetallic Ni-Co catalysts for the dry reforming of methane. Appl Catal A Gen 2009;371:54–9. https://doi.org/10.1016/j.apcata.2009.09.026.

[19] Xin J, Cui H, Cheng Z, Zhou Z. Bimetallic Ni-Co/SBA-15 catalysts prepared by urea co-precipitation for dry reforming of methane. Appl Catal A Gen 2018;554:95–104. https://doi.org/10.1016/j.apcata.2018.01.033.

[20] Erdogan B, Arbag H, Yasyerli N. SBA-15 supported mesoporous Ni and Co catalysts with high coke resistance for dry reforming of methane. Int J Hydrogen Energy 2018;43:1396–405. https://doi.org/10.1016/j.ijhydene.2017.11.127.

[21] Zhang J, Li F. Coke-resistant Ni at SiO2 catalyst for dry reforming of methane. Appl Catal B 2015;176–177:513–21. https://doi.org/10.1016/j.apcatb.2015.04.039.

[22] Plata JJ, Graciani J, Evans J, Rodriguez JA, Sanz JF. Cu Deposited on CeOx-Modified TiO2(110): Synergistic Effects at the Metal-Oxide Interface and the Mechanism of the WGS Reaction. ACS Catal 2016;6:4608–15. https://doi.org/10.1021/acscatal.6b00948.

[23] Chein RY, Fung WY. Syngas production via dry reforming of methane over CeO2 modified Ni/Al2O3 catalysts. Int J Hydrogen Energy 2019;44:14303–15. https://doi.org/10.1016/j.ijhydene.2019.01.113.

[24] Zhang X, Zhang Q, Tsubaki N, Tan Y, Han Y. Influence of Zirconia Phase on the Performance of Ni / ZrO 2 for 2015.

[25] Roh HS, Potdar HS, Jun KW, Kim JW, Oh YS. Carbon dioxide reforming of methane over Ni incorporated into Ce-ZrO 2 catalysts. Appl Catal A Gen 2004;276:231–9. https://doi.org/10.1016/j.apcata.2004.08.009.

[26] Juan-Juan J, Román-Martínez MC, Illán-Gómez MJ. Effect of potassium content in the activity of K-promoted Ni/Al 2O3 catalysts for the dry reforming of methane. Appl Catal A Gen 2006;301:9–15. https://doi.org/10.1016/j.apcata.2005.11.006.

[27] Monteiro WF, Vieira MO, Calgaro CO, Perez-Lopez OW, Ligabue RA. Dry reforming of methane using modified sodium and protonated titanate nanotube catalysts. Fuel 2019;253:713–21. https://doi.org/10.1016/j.fuel.2019.05.019.

[28] Owgi AHK, Jalil AA, Hussain I, Hassan NS, Hambali HU, Siang TJ, et al. Catalytic systems for enhanced carbon dioxide reforming of methane: a review. Environ Chem Lett 2021;19:2157–83. https://doi.org/10.1007/s10311-020-01164-w.

[29] Xu B, Fan Y, Zhang Y, Tsubaki N. Pore diffusion simulation model of bimodal catalyst for Fischer-Tropsch synthesis. AIChE Journal 2005;51:2068–76. https://doi.org/10.1002/aic.10469.

[30] Ma Q, Han Y, Wei Q, Makpal S, Gao X, Zhang J, et al. Stabilizing Ni on bimodal mesoporous-macroporous alumina with enhanced coke tolerance in dry reforming of methane to syngas. Journal of CO2 Utilization 2020;35:288–97. https://doi.org/10.1016/j.jcou.2019.10.010.

[31] Taguchi A, Schüth F. Ordered mesoporous materials in catalysis. vol. 77. 2005. https://doi.org/10.1016/j.micromeso.2004.06.030.

[32] Abdulkareem Ghassan A, Mijan N-A, Hin Taufiq-Yap Y. Nanomaterials: An Overview of Nanorods Synthesis and Optimization. Nanorods and Nanocomposites 2020:1–24. https://doi.org/10.5772/intechopen.84550.

[33] Yu K, Zhang X, Tong H, Yan X, Liu S. Synthesis of fibrous monodisperse core-shell Fe3O 4/SiO2/KCC-1. Mater Lett 2013;106:151–4. https://doi.org/10.1016/j.matlet.2013.04.112.

[34] Ding C, Gao X, Han Y, Ma X, Wang J, Liu S, et al. Effects of surface states over core-shell Ni@SiO2 catalysts on catalytic partial oxidation of methane to synthesis gas. Journal of Energy Chemistry 2015;24:45–53. https://doi.org/10.1016/S2095-4956(15)60283-2.

[35] Owgi AHK, Jalil AA, Hussain I, Hambali HU, Nabgan W. Enhancing resistance of carbon deposition and reaction stability over nickel loaded fibrous silica-alumina (Ni/FSA) for dry reforming of methane. Int J Hydrogen Energy 2022. https://doi.org/10.1016/j.ijhydene.2021.12.134.

[36] Wang M, Zhang Q, Zhang T, Wang Y, Wang J, Long K, et al. Facile one-pot synthesis of highly dispersed Ni nanoparticles embedded in HMS for dry reforming of methane.

Chemical Engineering Journal 2017;313:1370–81. https://doi.org/10.1016/j.cej.2016.11.055.

[37] Naeem MA, Al-Fatesh AS, Fakeeha AH, Abasaeed AE. Hydrogen production from methane dry reforming over nickel-based nanocatalysts using surfactant-assisted or polyol method. Int J Hydrogen Energy 2014;39:17009–23. https://doi.org/10.1016/j.ijhydene.2014.08.090.

[38] Abdulrasheed AA, Jalil AA, Hamid MYS, Siang TJ, Fatah NAA, Izan SM, et al. Dry reforming of methane to hydrogen-rich syngas over robust fibrous KCC-1 stabilized nickel catalyst with high activity and coke resistance. Int J Hydrogen Energy 2019:1–13. https://doi.org/10.1016/j.ijhydene.2019.04.126.

[39] Usman M, Wan Daud WMA, Abbas HF. Dry reforming of methane: Influence of process parameters - A review. Renewable and Sustainable Energy Reviews 2015;45:710–44. https://doi.org/10.1016/j.rser.2015.02.026.

[40] Abdullah N, Ainirazali N, Chong CC, Razak HA, Setiabudi HD, Jalil AA, et al. Influence of impregnation assisted methods of Ni/SBA-15 for production of hydrogen via dry reforming of methane. Int J Hydrogen Energy 2019. https://doi.org/10.1016/j.ijhydene.2019.09.089.

[41] Ashok J, Raju G, Reddy PS, Subrahmanyam M, Venugopal A. Catalytic decomposition of CH4 over Ni-Al2O3-SiO2 catalysts: Influence of pretreatment conditions for the production of H2. Journal of Natural Gas Chemistry 2008;17:113–9. https://doi.org/10.1016/S1003-9953(08)60036-5.

[42] Figueredo GP, Medeiros RLBA, Macedo HP, de Oliveira ÂAS, Braga RM, Mercury JMR, et al. A comparative study of dry reforming of methane over nickel catalysts supported on perovskite-type LaAlO3 and commercial A-Al2O3. Int J Hydrogen Energy 2018;43:11022–37. https://doi.org/10.1016/j.ijhydene.2018.04.224.

[43] Liotta LF, Wu H, Pantaleo G, Venezia AM. Co3O4 nanocrystals and Co3O 4-MOx binary oxides for CO, CH4 and VOC oxidation at low temperatures: A review. Catal Sci Technol 2013;3:3085–102. https://doi.org/10.1039/c3cy00193h.

[44] Littlewood P, Liu S, Weitz E, Marks TJ, Stair PC. Ni-alumina dry reforming catalysts: Atomic layer deposition and the issue of Ni aluminate. Catal Today 2020;343:18–25. https://doi.org/10.1016/j.cattod.2019.03.040.

[45] Huang X, Xue G, Wang C, Zhao N, Sun N, Wei W, et al. Highly stable mesoporous NiO-Y2O3-Al2O3 catalysts for CO2 reforming of methane: Effect of Ni embedding and Y2O3 promotion. Catal Sci Technol 2016;6:449–59. https://doi.org/10.1039/c5cy01171j.

[46] Li J, Miao P, Li Z, He T, Han D, Wu J, et al. Hydrothermal synthesis of nanocrystalline H[Fe, Al]ZSM-5 zeolites for conversion of methanol to gasoline. Energy Convers Manag 2015;93:259–66. https://doi.org/10.1016/j.enconman.2015.01.031.

[47] Pinheiro AN, Valentini A, Sasaki JM, Oliveira AC. Highly stable dealuminated zeolite support for the production of hydrogen by dry reforming of methane. Appl Catal A Gen 2009;355:156–68. https://doi.org/10.1016/j.apcata.2008.12.007.

[48] Owgi AHK, Jalil AA, Aziz MAA, Nabgan W, Hassan NS, Hussain I, et al. The preferable Ni quantity to boost the performance of FSA for dry reforming of methane. Fuel 2023;332. https://doi.org/10.1016/j.fuel.2022.126124.

[49] de Freitas Silva T, Reis CGM, Lucrédio AF, Assaf EM, Assaf JM. Hydrogen production from oxidative reforming of methane on Ni/γ-Al2O3 catalysts: Effect of support promotion with La, La-Ce and La-Zr. Fuel Processing Technology 2014;127:97–104. https://doi.org/10.1016/j.fuproc.2014.06.002.

[50] Kumar P, Sun Y, Idem RO. Comparative study of Ni-based mixed oxide catalyst for carbon dioxide reforming of methane. Energy and Fuels 2008;22:3575–82. https://doi.org/10.1021/ef800326q.

[51] Budiman AW, Song SH, Chang TS, Shin CH, Choi MJ. Dry Reforming of Methane Over Cobalt Catalysts: A Literature Review of Catalyst Development. Catalysis Surveys from Asia 2012;16:183–97. https://doi.org/10.1007/s10563-012-9143-2.

[52] Licciulli A, Notaro M, Santis S de, Terreni C, Kunjalukkal S. CO 2 capture on amine impregnated mesoporous alumina-silica mixed oxide spheres. Fuel Processing Technology 2017;166:202–8. https://doi.org/10.1016/j.fuproc.2017.06.009.

[53] Daniell W, Schubert U, Glöckler R, Meyer A, Noweck K, Knözinger H. Enhanced surface acidity in mixed alumina-silicas: a low-temperature FTIR study. vol. 196. 2000.

[54] Omata K, Nambu T. Catalysis of water molecules acting as Brönsted acids at Lewis acid sites on niobium oxide. Appl Catal A Gen 2020;607. https://doi.org/10.1016/j.apcata.2020.117812.

[55] Ding L, Li M, Zhao Y, Zhang H, Shang J, Zhong J, et al. The vital role of surface Brönsted acid/base sites for the photocatalytic formation of free ·OH radicals. Appl Catal B 2020;266. https://doi.org/10.1016/j.apcatb.2020.118634.

[56] Hambali HU, Jalil AA, Abdulrasheed AA, Siang TJ, Abdullah TAT, Ahmad A, et al. Fibrous spherical Ni-M/ZSM-5 (M: Mg, Ca, Ta, Ga) catalysts for methane dry reforming: The interplay between surface acidity-basicity and coking resistance. Int J Energy Res 2020:1–17. https://doi.org/10.1002/er.5327.

[57] sheng1994 n.d.

[58] Wood DL, Rabinovich EM. HEAT EVOLUTION, LIGHT SCAITERING, AND INFRARED SPECTROSCOPY IN THE FORMATION OF SILICA GELS FROM ALKOXIDES. vol. 107. 1989.

[59] Marie O, Massiani P, Thibault-Starzyk F. Infrared Evidence of a Third Brønsted Site in Mordenites. Journal of Physical Chemistry B 2004;108:5073–81. https://doi.org/10.1021/jp037915v.

[60] Montanari T, Marie O, Daturi M, Busca G. Cobalt on and in zeolites and silica-alumina: Spectroscopic characterization and reactivity. Catal Today, vol. 110, 2005, p. 339–44. https://doi.org/10.1016/j.cattod.2005.09.034.

[61] Chong CC, Teh LP, Setiabudi HD. Syngas production via CO 2 reforming of CH 4 over Ni-based SBA-15: Promotional effect of promoters (Ce, Mg, and Zr). Mater Today Energy 2019;12:408–17. https://doi.org/10.1016/j.mtener.2019.04.001.

[62] Chen BH, Chao ZS, He H, Huang C, Liu YJ, Yi WJ, et al. Towards a full understanding of the nature of Ni(II) species and hydroxyl groups over highly siliceous HZSM-5 zeolite supported nickel catalysts prepared by a deposition-precipitation method. Dalton Transactions 2016;45:2720–39. https://doi.org/10.1039/c4dt00399c.

[63] Zhang RJ, Xia GF, Li MF, Wu Y, Nie H, Li DD. Effect of support on catalytic performance of Ni-based catayst in methane dry reforming. Ranliao Huaxue Xuebao/Journal of Fuel Chemistry and Technology 2015;43:1359–65. https://doi.org/10.1016/S1872-5813(15)30040-2.

[64] San-José-Alonso D, Juan-Juan J, Illán-Gómez MJ, Román-Martínez MC. Ni, Co and bimetallic Ni-Co catalysts for the dry reforming of methane. Appl Catal A Gen 2009;371:54–9. https://doi.org/10.1016/j.apcata.2009.09.026.

[65] Rodriguez JA, Liu P, Wang X, Wen W, Hanson J, Hrbek J, et al. Water-gas shift activity of Cu surfaces and Cu nanoparticles supported on metal oxides. Catal Today 2009;143:45–50. https://doi.org/10.1016/j.cattod.2008.08.022.

[66] Shido T, Asakura K. Reactant-Promoted Reaction Mechanism for Catalytic Water-Gas Shift Reaction on MgO. vol. 122. 1990.

[67] Chen W, Zhao G, Xue Q, Chen L, Lu Y. High carbon-resistance Ni/CeAlO3-Al2O3 catalyst for CH4/CO2 reforming. Appl Catal B 2013;136–137:260–8. https://doi.org/10.1016/j.apcatb.2013.01.044.

[68] Chong CC, Bukhari SN, Cheng YW, Setiabudi HD, Jalil AA, Phalakornkule C. Robust Ni/Dendritic fibrous SBA-15 (Ni/DFSBA-15) for methane dry reforming: Effect of Ni loadings. Appl Catal A Gen 2019;584. https://doi.org/10.1016/j.apcata.2019.117174.

[69] Ribeiro NFP, Neto RCR, Moya SF, Souza MMVM, Schmal M. Synthesis of NiAl2O4 with high surface area as precursor of Ni nanoparticles for hydrogen production. Int J Hydrogen Energy 2010;35:11725–32. https://doi.org/10.1016/j.ijhydene.2010.08.024.

[70] Moradi G, Khezeli F, Hemmati H. Syngas production with dry reforming of methane over Ni/ZSM-5 catalysts. J Nat Gas Sci Eng 2016;33:657–65. https://doi.org/10.1016/j.jngse.2016.06.004.

[71] Hambali HU, Jalil AA, Abdulrasheed AA, Siang TJ, Vo DVN. Enhanced dry reforming of methane over mesostructured fibrous Ni/MFI zeolite: Influence of preparation methods. Journal of the Energy Institute 2020. https://doi.org/10.1016/j.joei.2020.01.016.

[72] Nguyen TGH, Tran DL, Sakamoto M, Uchida T, Sasaki K, To TD, et al. Ni-loaded (Ce,Zr)O2–Δ-dispersed paper-structured catalyst for dry reforming of methane. Int J Hydrogen Energy 2018;43:4951–60. https://doi.org/10.1016/j.ijhydene.2018.01.118.

[73] Zhang Y, Tao Y, Huang J, Williams P. Influence of silica–alumina support ratio on H2 production and catalyst carbon deposition from the Ni-catalytic pyrolysis/reforming of waste tyres. Waste Management and Research 2017;35:1045–54. https://doi.org/10.1177/0734242X17722207.

[74] Gurav HR, Dama S, Samuel V, Chilukuri S. Influence of preparation method on activity and stability of Ni catalysts supported on Gd doped ceria in dry reforming of methane. Journal of CO2 Utilization 2017;20:357–67. https://doi.org/10.1016/j.jcou.2017.06.014.

[75] Meng J, Gu T, Pan W, Bu C, Zhang J, Wang X, et al. Promotional effects of defects on Ni/HAP catalyst for carbon resistance and durability during dry reforming of methane. Fuel 2022;310:122363. https://doi.org/10.1016/j.fuel.2021.122363.

[76] Zhang ZL, Verykios XE. Carbon dioxide reforming of methane to synthesis gas over supported Ni catalysts. Catal Today 1994;21:589–95. https://doi.org/10.1016/0920-5861(94)80183-5.

[77] Han JW, Park JS, Choi MS, Lee H. Uncoupling the size and support effects of Ni catalysts for dry reforming of methane. Appl Catal B 2017;203:625–32. https://doi.org/10.1016/j.apcatb.2016.10.069.

[78] Serrano-Lotina A, Daza L. Highly stable and active catalyst for hydrogen production from biogas. J Power Sources 2013;238:81–6. https://doi.org/10.1016/j.jpowsour.2013.03.067.

[79] Navalikhina MD, Kavalerskaya NE, Lokteva ES, Peristyi AA, Golubina E v., Lunin V v. Hydrodechlorination of chlorobenzene on Ni and Ni-Pd catalysts modified by heteropolycompounds of the keggin type. Russian Journal of Physical Chemistry A 2012;86:1669–75. https://doi.org/10.1134/S0036024412110192.

[80] Phan TS, Sane AR, Rêgo de Vasconcelos B, Nzihou A, Sharrock P, Grouset D, et al. Hydroxyapatite supported bimetallic cobalt and nickel catalysts for syngas production from dry reforming of methane. Appl Catal B 2018;224:310–21. https://doi.org/10.1016/j.apcatb.2017.10.063.

Methane dry reforming on fibrous silica-alumina employing nanocrystals of nickel and cobalt to recognize the most efficient metal

A.H.K. Owgi [b], A.A. Jalil [a, b, c*], M.A.A. Aziz[a, b], W. Nabgan [d], M. Alhassan [b,f], M.H.M. Sofi [b], N.S. Hassan [b], R. Saravanan [e], M. B. Bahari [b].

[a] *Centre of Hydrogen Energy, Institute of Future Energy, 81310 UTM Johor Bahru, Johor.*

[b] *Faculty of Chemical and Energy Engineering, Faculty of Engineering, Universiti Teknologi Malaysia, 81310 UTM Johor Bahru, Johor, Malaysia.*

[c] *Saveetha School of Engineering, Saveetha Institute of Medical and Technical Science, Chennai 60210, India*

[d] *Departament d'Enginyeria Qu´ımica, Universitat Rovira I Virgili, Av Pa¨ısos Catalans 26, 43007, Tarragona, Spain.*

[e] *Faculty of Engineering, Department of Mechanical Engineering, University of Tarapacá, Avda, General Velasquez, 1775 Arica, Chile.*

[f] *Department of Chemistry, Sokoto State University, PMB 2134, Airport Road, Sokoto, Nigeria*

**To whom correspondence should be addressed,*

Aishah Abdul Jalil (Ph.D.)

Tel: 60-7-5535581 Fax: 60-7-5536165

Email: aishahaj@utm.my

Abbreviation.

(GHGs):	Greenhouse gas.
(DRM):	Dry reforming of methane.
(FSA):	Fibrous silica-alumina.
(CTAB):	Cetrimonium bromide.
(TEOS):	Tetraethyl orthosilicate.
(XRD):	X-ray diffractograms.
(XRF):	X-ray fluorescence
(FESEM):	Field emission scanning electron microscopy.
(FTIR):	Fourier-transform infrared.
(TEM):	Transmission electron microscopy.
(H_2-TPR):	H_2 temperature program reduction.
(TGA):	Thermogravimetric analysis.
(GC):	Gas chromatography.
(BET):	Brunauer-Emmett-Teller.
(C-NTs):	Carbon nanotubes
(D-band):	Disorder-generated band
(G-band):	Graphite carbon band
(TCD):	Thermal conductivity detector
(NLDFT):	Non-local density functional theory
(TO):	Transverse-optical
(LO):	Longitudinal-optical

ABSTRACT

Presently, the production of syngas through the dry reforming of methane is a widely employed approach for reducing vast amounts of greenhouse gas emissions. Several metals, particularly transition metals support have been evaluated as active DRM catalyst systems. In this work, a comparative studies is presented between Cobalt and Nickel metals impregnated over fibrous silica-alumina (FSA) support synthesized by the hydrothermal method for dry methane reforming. The specimens were characterized via FESEM mapping, TEM, XRD, H_2-TPR, XRF, N_2 physisorption, and KBr-FTIR techniques. Unlike the Co/FSA, Ni/FSA displayed a higher surface area with a fine dispersion of Ni nano-crystalline and less agglomeration, and more active sites which enhanced the metal-support interaction. Approximately 0.2g of each catalyst was evaluated at 650 - 800 ºC with a respective. CH_4:CO_2:N_2 ratio of 1:1:2, gas hourly space velocity 30,000 mL g^{-1} h^{-1}. The Ni/FSA demonstrated more conversion of CH_4 (89%) over (67%) of Co/FSA at 800ºC. After 10 h of long-term reaction, the Ni/FSA exhibited more stability at 800 ºC. TGA/DTA, Raman, and TEM results showed that spent Ni/FSA catalysts did not demonstrate signs of considerable nano-graphitic carbon or metal sintering as compared to Co/FSA catalysts, which had bigger crystallites of Co. The finding of this study would add new knowledge on reaction conditions involving and catalytic activities of the metals over the FSA.

Keywords: cobalt, nickel; carbon resistance; methane dry reforming; Fibrous silica-alumina.

1.0 Introduction

In recent years, there has been a great deal of interest in the dry reforming of methane, which is the conversion of the major negative component of fossil fuel emissions, (CO_2 and CH_4), which is pose a serious environmental issue into synthesis gas with an H_2/CO ratio of unity, which is used to produce synthetic fuel [1–3]. This procedure is incredibly significant to the environment as the GHGs utilized as gas sources are methane and carbon dioxide, all of which are harmful greenhouse gases. It has been suggested that dry reforming of methane (DRM) is a preferable option to producing syngas (H_2/CO≈1) since it can decrease CO_2 emissions while producing beneficial raw materials [2]. To enhance DRM at the industrial scale, three fundamental aspects must be addressed: (1) improved carbon dioxide and methane activation; (2) the improved comprehension of the mechanisms and reaction processes that create H_2 and CO; and (3) strategies to prevent deactivation of catalyst operations [4,5].

In the Fischer-Tropsch synthesis, a feedstock gas combination containing a low H_2/CO ratio is preferred for the creation of hydrocarbon fuels [6–8]. To achieve appropriate conversion levels, the endothermic aspect of the reaction necessitates a high reaction temperature. Because of the considerable operational temperature, adequate catalysts are required. The creation and build-up of carbonaceous deposits typically lead to the sintering of metal particles followed by the deactivation of catalysts as a consequence of the excessive temperature [9–13]. Recently, it is proven that noble metals including platinum, rhodium, and ruthenium, as well as non-noble metals as transaction metals (Ni, Co, and Fe), are employable as catalysts in dry reforming processes[9,10]. According to reports, noble metals possess excellent catalytic activity and have insignificant coking potential. However, due to their restricted variety and expensive cost, they are not widely used in the industrial sector.

Because of their cheaper cost and equivalent catalytic efficiency, non-noble metals such as nickel and cobalt have attracted the curiosity of researchers [4,14–16].

Despite the great catalytic performance demonstrated by nickel-based catalysts, the significant coking and swift inactivation prevent them from being used in industrial applications. Cobalt catalysts for example, possess a considerable soot oxidation ability which could be employed to increase the resistance of a catalytic process to carbon production by reducing the coke formation. Nonetheless, cobalt catalysts exhibit a high proclivity for re-oxidation, resulting in low performance [17–20].

The majority of the recent investigations in this area are primarily focused on reducing carbon creation in a variety of methods, either by ; i) using supports that have high oxygen ion mobility which may interact with adsorbed carbon species, such as SiO_2, CeO_2, and ZrO_2 solid solutions, as opposed to conventional supports[21–25]; ii) the employment of additives such as potassium or sodium, which provide basic aspects to the surface characteristics, despite the reality that they reduce the catalytic activity[26,27]. iii) modifying the morphologies of support specifically bimodal, mesoporous, nanorods, core-shell, nano-fibrate, and fibrous dendrimers [28–34]. The fabrication of incredibly multifunctional supported metal catalysts by wide metal dispersion of nanoparticles is one of the crucial options for heterogeneous catalytic systems that require research. Our prior research on the successful growth of fibrous silica-alumina (FSA) via exceptional surface area and thermal stability was the inspiration for this study [35]. In the present study, the FSA was investigated for DRM and the performance of the metals (Ni and Co) loaded over FSA aiming at getting a greater understanding of the metal's impact on catalytic efficiency and carbon formation.

2.0 Experimental

2.1 Catalyst Preparation

Fibrous silica-alumina support has been generated through the hydrothermal method and Al_2O_3. Alumina nitrate (Sigma-Aldrich, > 98%) was combined into a homogenous mixture of n-butanol (Merck, > 98%) and toluene (Sigma-Aldrich, > 98%). Afterward, the solution was stirred for approximately 30 min prior to introducing TEOS (Merck, > 98%) and was poured dropwise. Urea (Merck, > 98%), Cetrimonium bromide (CTAB- Sigma-Aldrich, > 98%), and 0.75 L of deionized water were added to the mixture. Toluene/1-butanol=13.8, urea/CTAB=3.8, and Si/Al=1.23 are the essential variables. While being exposed to microwave radiation at 400 W for 360 min, the subject substance was vaporized at 120 ℃ for overnight evaporation. The white specimen was heated in a furnace for 360 min at 550 C to produce FSA support.

2.2 Loading Metals

To load metals onto FSA, a 5 wt% Co and Ni-impregnated solution of $Co(NO_3)_2$ and Ni $(NO_3)_{2.6}H_2O$ were (% trace metals) used as purchased from Sigma-Aldrich. Bhd. They dissolved in deionized water was deployed. Before getting impregnated, the specimens were evaporatively dried and then calcined for three hours at 550 °C. Co/FSA and Ni/FSA were the end products of this procedure.

2.2 Characterization

A Bruker D8 Advance diffraction pattern, Which was certified utilizing Cu K-ray radiation at 1.54 wavelengths, was employed to conduct the XRD study on pristine and spent samples. The determination is intended to generate X-ray diffractograms in the range of 1-280º employing data at 0.05º and 0.1º at 46kV and 41mA. (FESEM; Zeiss Supra VP35) field emission scanning electron microscopy was deployed to further analyze the structure of samples. N_2 adsorption-desorption through ASAP2020 apparatus was using an N_2/He mixed gas and a from Micromeritics to determine surface areas. 0.1– 0.15 g of the specimen were refluxed at 200 °C for 240 min before the assessment, followed cooled to room temperature. The BET technique was employed to calculate the total surface area. Additionally, Fourier-transform infrared (FTIR) measurements were conducted on the materials using the Agilent Technology Varian 670 apparatus at 30 ℃ in the 400 to 4000 cm^{-1} wavelength range. By using a Rigaku Primus 2 apparatus and lithium tetraborate to treat the materials, the metal percentage was evaluated using wavelength-dispersive X-ray fluorescence (XRF).

The carbon-containing aggregate structuring in the utilized catalysts was examined by adopting 510nm lasers with a 50x magnified microscope mounted on a Renishaw via a Raman spectrophotometer, The Raman spectra of the specimen were recorded around 1000 and 2200 cm^{-1}. A TGA/SDTA 851e Mettler Toledo thermo-gravimetric instrument with a temperature range of 5-950 ℃ and a heating rise of 10 ℃/min with airflow has also been employed to assess carbon deposits. Additionally, utilizing JEOL JEM-2100 F technology, transmission electron microscopy (TEM) was conducted on the spent samples. All of the materials were acetone-liquefied before being positioned on a copper gridiron that had a penetrable carbon layer covering it. Temperatures of 100 to 1000℃ and an H_2/N_2 flow rate with a concentration of 10% were employed to investigate the reduced specimen (20 mL min^{-1}).

2.3 Catalyst assessment

The DRM assessments were carried out on various catalysts using a series of efficiency measurements at a temperature limitation of 500-850 ℃ through streaming the gases in a fixed-bed reactor to identify the detrimental impacts of the metals on the long-term catalyst performance. The catalysts were tested employing a stream running continuously in a reactor at environmental pressure and a heat range of 500–850 ºC. A portion of the pelletized catalyst (2mg) was placed in a reactor, blocked by quartz wool. Before the activity, the preload catalyst was initially treated with 15 mL min^{-1} oxygen at 700 ℃ for 60 min, followed by 100 $ml.min^{-1}$ at 800 ºC throughout 120 min of H_2:N_2 (50:50). Then the reactor was cooled to a set temperature as a function of the impacts of N_2. The reactor was supplied with the mixture of gases CO_2: CH_4: N_2 at 25:25:50 $ml.min^{-1}$ rate. To continuously monitor and evaluate the surplus reactant and gas released, (Agilent 7890A GC) a gas chromatograph set via a (1010)column carboxy with a 0.1L collecting band with thermal detecting was employed (TCD). Before a randomized choice was determined, 60 minutes were required for reaching the reaction equilibrium at the examined temperature. Equations (1-7) were employed to estimate the rate of conversions and the ratio of syngas (H_2/CO) [9,36,37].

Conversion of CH_4 $= \frac{F_{(CH4)in} - F_{(CH4)out}}{F_{(CH4)in}} \times 100$ (1)

Conversion of CO_2 $= \frac{F_{(CO2)in} - F_{(CO2)out}}{F_{(CO2)in}} \times 100$ (2)

H_2/CO $= \frac{F(H_2)out}{F\ (CO)out}$ (3)

H_2 Selectivity $= \frac{F_{(H2)out}}{2\ [\ F_{(CH4)in} - F_{(CH4)out}]} \times 100$ (4)

CO Selectivity $= \frac{F_{(CO)out}}{[\ F_{(CH4)in} - F_{(CH4)out}] + [\ F_{(CO2)in} - F_{(CO2)out}]} \times 100$ (5)

H_2 Yield $= \frac{F(H_2)out}{2 \times F\ (CH)4in}$ (6)

CO Yield $= \frac{F_{(CO)out}}{F_{(CH4)in} - F_{(C02)in}]} \times 100$ (7)

3.0 Reflection on The Findings

3.1 Catalysts characterization

3.1.1 Characteristics of structure and morphology

Figure 1(A–C) displays FESEM micrographs including elements mapping of all specimens demonstrating the particle dispersion of metal. Figures 1(A) depict the creation of the fibrous silica-alumina structure's expected spherical bi-continuous concentric fibrillar shape. NiO and CoO crystallite scattering and sizes were soft purple spots evident scattered over the support structure. The particle sizes, as determined from the XRD spectra using the Scherrer equation, are 11.7nm and 14.3nm for Ni and Co FSA catalysts respectively. For this reason, the Co is less spread on the surface of the FSA than Ni/FSA [38]. The Co was inadequately diffused on the fibrous silica-alumina (Fig. 1C), due to its limited pores as well

as surface area, as shown by the lumps of Co on the surface of the FSA after impregnation. This being the cause of rapid Co/ FSA inactivation during only short hours on the stream cannot be outweighed. Because of the limited distribution of Co, there is a limited surface for reaction and reduction, resulting in significant sintering due to tiny crystallite migration. Consequently, the deactivation potential of the catalyst will be larger based on the amount of carbon placed [5,12,39]. Moreover, Traces of cobalt and nickel were observed via catalysts are 5.10% and 4.84% respectively by XRF analysis (in the Table.1), The amounts of Ni-loading at 5% wt are consistent with the quantities employed during catalyst preparations, and the identifying amounts of compounds utilized in this investigation are true.

Figure .2. displays the crystalline structures through the X-ray diffraction (XRD) for the specimens FSA, Ni/FSA, and Co/FSA. All the samples demonstrated a broad 2θ band from 20 to 30º, this is often attributed to the amorphous phase of SiO_2 (JCPDS card No. 29-0085)[40,41]. Because of the existence of silica species during the fabrication of dendrimeric silica fibres, the XRD pattern intensity diminished. The Ni and Co FSA catalysts both exhibited nine prominent peaks at 2θ value of 25.8°, 35.4°, 37.8°, 43.5°, 52.8°, 57.5°, 66.7°, 68.4°, and 77.1° identical to the (0 1 2), (1 0 4), (1 1 0), (1 1 3), (0 2 4), (1 1 6), (2 1 4), (3 00), and (1 1 9) alumina crystalline planes via structures of rhombohedral (JCPDSICDD File No 46-1212) for FSA sample [35,42].

Three diffraction peaks were seen for NiO via Ni/FSA at 2θ = 62.9, 75.4, and 79.4°, correlating to NiO planes (2 20), (2 2 2), and (3 1 1), respectively (JCPDS 78-0643). The Co_3O_4, Co/FSA showed five peaks at 2θ = 18.6, 31.3, 36.8, 44.8, and 59.4°, which corresponded to (111), (2 2 0), (3 1 1), (4 0 0), and (511), respectively (JCPDS 42-1467)[43]. The diffraction peak intensity was found to be lower in Ni/FSA in comparison to Co/FSA. As revealed by the FESEM studies; moreover, the nano-crystallite metals of NiO deposited on FSA were uniformly distributed more than Co_3O_4. Owing to the active site mobility

obtainable through FSA, which enables NiO scattering, the possibility for NiO crystal aggregation and the metal-support interaction is increased [44]. Moreover, the peaks of Ni-Al_2O_4 appeared less higher than that of Co-Al_2O_4 indicating more crystallinity of Co over Ni

3.1.2 Textural properties

N_2 adsorption-desorption analysis was used to investigate the textural properties of the FSA, Ni/FSA, and Co/FSA. Figure.3 shows the N_2 adsorption-desorption isotherms including pore size dispersion of the catalysts. Referring to the IUPAC categorization, the catalyst isotherms displayed regular type IV adsorption phases at P/Po = 0.4, and 0.9, indicating a mesoporous property [45,46]. The scattering of pore sizes overall catalysts is illustrated in the figure.3 implementing (NLDFT) non-local density functional theory.

The FSA revealed a sharp peak in the 50-70 (Å) range and a thin peak in the 100-200 (Å) band for mesopore distribution. The high peak is due to the formation of mesopores during surfactant self-assembly. However, the small peaks are owing to the spacing between dendrimeric molecules. When Ni/FSA was compared to FSA, there was no substantial shift in pore dispersion. This attests to a real dispersion of Ni dispersion confirmed by FESEM (Fig. 1). However, the peak intensity of pore dispersion is decreased by adding Co. This finding is linked to a decrease in the amount of adsorbed N_2 in Co/FSA P/Po = 0.46–1.0, indicating a decrease in micropores and interparticle voids mesopores[47]. In the present study (Table.2), the FSA displayed (334.92 $m^2\ g^{-1}$) an extraordinary surface area, after loading Ni, the surface area increased to 338.54 $m^2\ g^{-1}$ because there was more scattering of active metal [48]. Moreover, increased Ni encasement over Ni/FSA indicates that dispersion has been optimized. As seen in figure 1. However, when Co was added to the FSA, the surface area and pore volume were reduced to 303.6 $m^2\ g^{-1}$ and 0.856 $cm^3\ g^{-1}$ respectively.

With the addition of Co, the catalysts' surface area and pore volume diminished due to partial pore blockage and/or pore filling.

3.1.3 Reducibility

TPR-H_2 of the calcined catalysts was performed to gain a deeper insight into the evolution of the nickel and cobalt phases as shown in figure.4. This was useful in determining the reduction degree of the Co and Ni oxide species. the solitary peak of Ni/FSA in the region from 260 ºC to 360 ºC correlates to Ni species reduction [49,50]. This is most definitely attributable to a reduction in narrower NiO nanoparticles or nickel aluminates as shown in the XRD result [44,49]. A low degree of reduction peak might imply that the interaction of NiOx species was slight with the exterior of FSA dendritic fibres.

There were two essential reduction stages in the Co/FSA catalyst's reduction studies. The reduction peak centred close to 300-510 ºC is assigned to free Co_3O_4 reduction.However, this involved consecutive reductions to CoO and metallic Co, respectively. A unique peak was identified between 560 and 770 ºC showing the occurrence of considerable quantities of $CoAl_2O_4$ obtained from the strong interaction between Co_3O_4 and Al_2O_3 [12,17,43,51].

3.1.4 Spectroscopic Studies

FTIR spectroscopy with wavelengths between 400 and 4000 cm-1, assessed the various construction heterogeneity of the (Co and Ni) supported FSA, as displyed in figure.5. The most prominent peaks exhibited siliceous frames because Si interacted with various atoms, (for instance, Si-O-Si, Si-OH, Si-O, Al-O-Al, and Si-O-Al) through the range 400–1300 cm^{-1}. [52]. The wavenumbers of five peaks 1240, 1090, 960, 790, also 460 cm^{-1} were demonstrated in all specimens, indicative of Si-O-Si bond apparent within the range of 960-1260 cm^{-1} in all samples [53]. Similar, all catalysts in fig.5 demonstrated a peak at 3400 cm^{-1} indicative of that O-H-stretching vibration due to water molecules, or Brønsted acid sites

which are dependent on hydrogen concentration [54,55]. As displayed by the same figure, Ni/FSA possess a low-intensity peak at 3400 cm^{-1} reflected in low Brønsted acid sites. Furthermore, asymmetric stretching peak attributed to Si-O-Si transverse-optical (TO) and longitudinal-optical (LO) bands were apparent at approximately 1240 cm^{-1} and 1090 cm^{-1}, respectively [56–58]. The weak bands at 960 and 1640 cm^{-1} were assigned to external groups of Si-OH, whilst symmetric and asymmetric Al-O and Si-O stretch vibrations were pronounce at 800 cm^{-1} and 462 cm^{-1}, respectively [59]. Apart from stretching vibrations, symmetrical and asymmetrical stretch attributable to Si-O-Al were reported by [60] 1090, 790 and 460 cm^{-1} .The disappearance of these peaks upon the introduction of Ni and Co to FSA, could imply that the Si–O–Si and Si-OH were partly replaced by Ni–O–Si, Co–O–Si, Ni-O, and Co–O. In particular, the peak at 666 cm^{-1} in the Co/FSA is attributable to Co–O vibrations indicating the successful incorporation of Co onto the support [17,41]. Accordingly, substituting result of the O–H and O–Si with the Ni ions in the dendritic fibrous FSA structure entails a greater reduction in peak density compared to the Co sample, emphasizing that Ni had a more robust interaction with FSA support than the Co [61,62].

3.2 Activity Evaluation

Figure.6 shows the activity results of Ni/FSA and Co/FSA. Ni/FSA converted more CH_4 than Co/FSA under identical reaction conditions. Based on the fine Ni dispersion as seen in the FESEM picture, Ni/FSA catalysts were more efficient than Co/FSA catalysts, which enhanced the porosity and surface area, thereby providing a variety of active reaction sites and mobility of reactant mass in the process. Additionally, textural characteristics have a significant role in catalytic activity, as demonstrated by the FSA characteristics that supply the active species required to prevent deactivation of the catalyst (surface area, pore size, and

pore volume) [63]. Thus, owing to the extraordinary surface area of Ni/ FSA and possession of high oxygen storage deposits of C are easily transformed to CO thereby forming intermediates carbonate species into reductive basic supports reflected avoiding the coke formation [28].

The Ni/FSA catalyst shows superior catalytic efficacy, with the sustained conversion of CH_4 and CO_2 exceeding 89 % and 80 %, respectively, at 800 ºC, In comparison to Co/FSA (XCH_4= 67%, XCO_2 63%). Indeed, the tiny metal particles and superior metal diffusion will lead to more edges and metal-support frameworks, resulting in more active sites. Interestingly, the conversion of CH_4 and CO_2 at 700 were similar for the Ni/FSA and Co/FSA catalysts, indicating the possibility that side reactions such as; methane decomposition ($CH_4 \rightarrow C + 2H_2$) and the Boudouard reaction ($2CO \leftrightarrow C + CO_2$) have occurred [7,64].

To verify the successful Ni/FSA synthesis for DRM catalytic ability in comparison to the Co/FSA at 800 °C prolonged performance for 10 hours, the stabilization assessments were carried out as shown in fig.7 (A and B). Compared to Co/FSA (XCO_2 = 17%, XCH_4 = 21%), the FSA catalyst exhibits superior catalytic performance, with the stable CO_2 conversion and CH_4 achieving 91 % and 96 %, respectively. The catalytic performance of Co/FSA decreases during the second hour while on stream. This should be identified by the poor Co dispersion within surface aggregation and increased acidity that causes coke deposit and inactivation [28,51]. Moreover, the H_2/CO ratio for Co/FSA is lesser than that of Ni/FSA, achieving a ratio of 0.85 to 95 as depicted in Fig. 7C, which is appropriate for the Fischer-Tropsch application to synthesize lipid long hydrocarbons chain. This possibly is owing to the possibility of Ni/FSA to disperse oxygen species over the surface than Co/FSA catalyst [18,19,63]. According to Fig. 8, the H_2 yield showed a different trend with conversions, with Ni/FSA achieving the highest H_2 yields and Co/FSA achieving the lowest. Meanwhile, the exception of CO selectivity that appeared to be caused by the Co/FSA

catalyst could be explained by the RWGS reaction ($CO_2 + H_2 \leftrightarrow CO + H_2O$). where the H_2 and CO selectivity of Ni/FSA were quite similar, which were 48% of S (CO) and 51% of S (H_2) [65,66].

Simultaneous secondary reactions that occurred throughout catalytic testing were predictable. On the other hand, from the H_2/CO profiles as displayed in Fig. 7C, In actuality, a rise in the ratio of syngas on Ni/FSA after 6 hours was driven by the concomitant occurrence of CH_4 decomposition ($CH_4 \rightarrow C + 2H_2$) and CO disproportionation ($2CO \leftrightarrow C + CO_2$). These subsequent reactions neither simply influenced the syngas ratio, but also produced carbonaceous species that were detrimental to catalytic activity. On the contrary, in the first hours of the reaction, the syngas ratio was shown to drop for both specimens, which was caused by the reverse water gas shift (RWGS) reaction to the decrease in syngas ratio. and seem to improve with the favourability of thermodynamics [67,68].

The activity of Ni/FSA was preferable over that of Co/FSA, which might be attributed to its significant number of active sites via the mesoporous and microporous supplies by the support's fibrous temple. In particular, the characterization results show that the thinner crystallite of NiO is diffused homogeneously across the FSA compared to Co. However, Co has shown in FESEM more accumulation onto the FAS than Ni, as well as the Co particles having blocked the pores of the FSA the (Table. 2). This creates a tremendous contribution to increasing NiO engagement within the FSA and drastically enhancing the environmental basicity of catalysts. As stated previously, the catalysts' basicity assisted CO_2 decomposition and gasification while limiting CH_4 interactions with active sites, potentially minimizing coke formation during the long-term activity[69,70].

Interestingly, FTIR results show that the existence of a synergic influence among Nickle particles and fibrous silica-alumina mesostructures via the generation of Ni-O-Al and

Ni-O-Si bonds prevents the aggregation of metal. This coordinated impact shielded the metallic Ni^0 phase during the reduction of the NiO crystalline phase through the H_2 stream before the reaction begging, thus increasing the re-efficiency of both gaseous reactants, CH_4 and CO_2. The inferior catalytic efficacy of Co/FSA is probably attributed to the coke forming and possibly sintering metals during the DRM process [68,71].

3.3 Spent Characterization

During 10 hours of activation, the Raman spectra evidenced the distinct species of carbon extent in Fig. 9. The sp2-bonded carbon deposit is responsible for two peaks: the disorder-generated band (D-band) at 1350 cm^{-1} and the graphite carbon band (G-band) at 1584 cm^{-1} [38]. The G-to-D-band ratio (IG/ID) is a representation of the amount of carbon placed, which evaluates the quantity of graphitization of coke deposits. Consequently, a higher IG/ID ratio implies that graphitic carbon is being generated at an accelerated rate more highly than amorphous carbon and inconsistently, increases the catalyst's susceptibility to deactivation and complicates the renovation process [72]. The IG/ID ratios for Co/FSA and Ni/FSA were 1.02 and 0.9, respectively, confirming both carbons, graphitic and amorphous, were attended with both specimens. Raman spectra revealed that the Ni/FSA had the lowest IG/ID ratio and narrowest band zones throughout Raman wavelengths. This indicates that a small amount of carbon is deposited on Ni/FSA, while the maximum carbon achieves an amorphous and disordered formation that has little potential for catalyst disruption. The disordered carbon formations are mainly gasified throughout the DRM, preventing them from accumulating and developing into a more stable carbon deposit.

Coke coatings on the catalyst surface were evaluated using the TGA and DTA investigation, and the findings are displayed in Fig.10. The charts demonstrated the weight portion loss caused by the used catalysts, the amount of carbon formed, and the volume of

coke that might be replaced over the suppression mechanism of oxidation employing plenty of O_2 to form CO_2. For the Ni/FSA catalyst, the preliminary loss of weight happened at approximately 85°C and progressed at 4%. This demonstrates the formation of amorphous crbon, which is recognized to oxidize at lower temperatures compared to other carbons deposits, on the catalyst surface [73]. Observations in ancient times have proven that the size of the metal crystallization has a considerable impact on restricting carbon residue or elution, as catalysts with minimal metal crystalline phases release fewer cokes [74]. Additionally, the Raman and TGA analyses provided physical and quantifiable verification of the coke generation. The ease of oxidation exhibited by amorphous carbon over graphitic one made its impact after 10h on stream lesser [75]. On the contrary, the loss of weight particularly evident in Co/FSA, with a maximum value of peak position appearing at about 600 °C confirms the accumulation of exceptionally carbonaceous graphitic, which is challenging to gasify on-site. This carbon type has responsible for the rapid deactivation of Co/FSA, as shown by the stability evaluation (Fig. 7).

The DTG patterns can be subdivided into distinct peaks correspond to different types of carbon and are classes dignifed by the symbols Cγ, Cβ, and Cα [76]. The TGA profile was utilized to differentiate varieties in (Fig. 10B). Amorphous carbon (Cα) is oxidized at minimal temperatures to produce the syngas. Whereas, at extreme temperatures, Cγ and Cβ are oxidized, and those carbon sorts are actually involved in the mechanism of catalyst performance. The mass loss of roughly 100^{o}C recorded across all specimens is assigned to C, whereas the minor peak at 550^{o}C is related to Cβ, which is presumably formed by polymerization and rearrangement of active carbon species. At approximately 650 C, the weight losses were caused by crystalline carbon C, which is crucial for catalytic inactivation [77,78].

After 10 hours time on stream, the catalysts had not morphologically deformed and had sustained the FSA fibrosis (as shown in Fig.11). The Ni lattice fringes were discovered in the assessed quadrat space with lattice spacings of 0.18, 0.25, and 0.2 nm for the Ni/FSA specimen (Fig. 11B) and related to Ni (200), NiO (111), and Al_3Ni (301), respectively. Moreover, the lattice area which correlated to the Co_3O_4 (111), CoO (200), and Co (100) was 0.466, 0.213, and 0.208 nm, respectively in fig .11D. The lattice spacing of carbon interplanar was nonexistent on Ni/FSA provided evidence that carbon-graphite prevention was observed. Only on Co/FSA could different lattice fringes be seen that were related to carbon graphite and nanotubes with different levels of graphitization (Fig. 9D).

The formation of amorphous carbon disordered around the Ni nanoparticles is depicted (Fig.11A). The reaction indicated rapid gasification through oxygen vacancy to generate excess CO with no deactivation by coking. Consequently, it had minimal potential for accumulation in a long-term activity. Although the coke formation was insignificant after 10 hours of reaction, but the carbon nanotubes (C-NTs), whiskers, as well as amorphous coke species were visible on the spent Co/FSA, as evidenced by the TGA and Raman data. As shown in Figure 6, the apparent inactivity of Co/FSA during the early periods of the long-term reaction could be caused by the steady and structural carbon deposition and its lower sintering resistance as catalysts are more prone to inactivation if apprecible graphitic carbon is generated [41,79,80].

4.0 Conclusion

To conclude, fibrous silica-alumina (FSA) has been synthesized through the hydrothermal method with various loading metals by the impregnation method. In the KBr-FTIR and H_2-TPR investigations, the appearance of the degree of metal interactions was conditional on metal dispersion attributed to metal crystallite size on the support surface.

Accordingly, Ni/FSA generated superlative function in the DRM reaction across a temperature range of 500–850 °C and extraordinary stability over 10 h it due to its a large surface area (338.56 m^2/g), fine size dispersion of Ni, and strong metal-support interaction, as well as strong resistance to sintering by restricting Ni atoms or crystallite movements on the support. However, Co/FSA had a bigger crystallinite size, which affects the metal-support interaction reflected in the performance of the catalyst. The Ni/FSA catalyst serves as a coke inhibitor and a disordered amorphous phase with no effect on the catalyst stability. These characteristics are the vital causes for Ni/FSA catalyst's superior efficiency to Co/FSA synthesized via wet impregnation. As documented, the conversion of CH_4 was 97.5% for Ni/FSA, while it dramatically dropped to 20.63% for Co/FSA

Acknowledgment

The High Impact Research (UTMHR) Grant from Universiti Teknologi Malaysia funded this research project (08G92).

Reference

[1] Arbag H, Yasyerli S, Yasyerli N, Dogu G. Activity and stability enhancement of Ni-MCM-41 catalysts by Rh incorporation for hydrogen from dry reforming of methane. Int J Hydrogen Energy 2010;35:2296–304. https://doi.org/10.1016/j.ijhydene.2009.12.109.

[2] Gallego GS, Marín JG, Batiot-Dupeyrat C, Barrault J, Mondragón F. Influence of Pr and Ce in dry methane reforming catalysts produced from La1-xAxNiO3-δ perovskites. Appl Catal A Gen 2009;369:97–103. https://doi.org/10.1016/j.apcata.2009.09.004.

[3] Chong CC, Owgi AHK, Ainirazali N, Chin SY, Setiabudi HD. CO2 reforming of CH4 over Ni/SBA-15 prepared by surfactant-assisted impregnation method: Comparative study of surfactant types. Mater Today Proc 2018;5:21644–51. https://doi.org/10.1016/j.matpr.2018.07.014.

[4] Liu Z, Grinter DC, Lustemberg PG, Nguyen- Phan T, Zhou Y, Luo S, et al. Dry Reforming of Methane on a Highly- Active Ni- CeO 2 Catalyst: Effects of Metal- Support Interactions on C−H Bond Breaking . Angewandte Chemie 2016;128:7581–5. https://doi.org/10.1002/ange.201602489.

[5] Aramouni NAK, Touma JG, Tarboush BA, Zeaiter J, Ahmad MN. Catalyst design for dry reforming of methane: Analysis review. Renewable and Sustainable Energy Reviews 2018;82:2570–85. https://doi.org/10.1016/j.rser.2017.09.076.

[6] Takanabe K, Nagaoka K, Nariai K, Aika KI. Influence of reduction temperature on the catalytic behavior of Co/TiO 2 catalysts for CH4/CO2 reforming and its relation with titania bulk crystal structure. J Catal 2005;230:75–85. https://doi.org/10.1016/j.jcat.2004.11.005.

[7] Takanabe K, Nagaoka K, Nariai K, Aika KI. Titania-supported cobalt and nickel bimetallic catalysts for carbon dioxide reforming of methane. J Catal 2005;232:268–75. https://doi.org/10.1016/j.jcat.2005.03.011.

[8] Ruckenstein E, Wang HY. Carbon deposition and catalytic deactivation during CO2 reforming of CH4 over Co/γ -Al2O3 catalysts. J Catal 2002;205:289–93. https://doi.org/10.1006/jcat.2001.3458.

[9] Therdthianwong S, Therdthianwong A, Siangchin C, Yongprapat S. Synthesis gas production from dry reforming of methane over Ni/Al2O3 stabilized by ZrO2. Int J Hydrogen Energy 2008;33:991–9. https://doi.org/10.1016/j.ijhydene.2007.11.029.

[10] Gao J, Hou Z, Guo J, Zhu Y, Zheng X. Catalytic conversion of methane and CO2 to synthesis gas over a La2O3-modified SiO2 supported Ni catalyst in fluidized-bed reactor. Catal Today 2008;131:278–84. https://doi.org/10.1016/j.cattod.2007.10.019.

[11] Hambali HU, Jalil AA, Abdulrasheed AA, Siang TJ, Owgi AHK, Aziz FFA. CO2 reforming of methane over Ta-promoted Ni/ZSM-5 fibre-like catalyst: Insights on

deactivation behavior and optimization using response surface methodology (RSM). Chem Eng Sci 2021;231. https://doi.org/10.1016/j.ces.2020.116320.

[12] Fatah NAA, Jalil AA, Triwahyono S, Yusof N, Mamat CR, Izan SM, et al. Favored hydrogenation of linear carbon monoxide over cobalt loaded on fibrous silica KCC-1. Int J Hydrogen Energy 2020;45:9522–34. https://doi.org/10.1016/j.ijhydene.2020.01.144.

[13] Tran NT, van Le Q, van Cuong N, Nguyen TD, Huy Phuc NH, Phuong PTT, et al. La-doped cobalt supported on mesoporous alumina catalysts for improved methane dry reforming and coke mitigation. Journal of the Energy Institute 2020:1–10. https://doi.org/10.1016/j.joei.2020.01.019.

[14] Shiju NR. The Role of Metal-Support Bonding in Controlling the Particle Size of Ceria-Supported Transition Metal Catalysts. ChemCatChem 2011;3:112–4. https://doi.org/10.1002/cctc.201000357.

[15] Wang F, Xu L, Zhang J, Zhao Y, Li H, Li HX, et al. Tuning the metal-support interaction in catalysts for highly efficient methane dry reforming reaction. Appl Catal B 2016;180:511–20. https://doi.org/10.1016/j.apcatb.2015.07.001.

[16] Ruckenstein E, Hu YH. Carbon dioxide reforming of methane over nickel/alkaline earth metal oxide catalysts. Appl Catal A Gen 1995;133:149–61. https://doi.org/10.1016/0926-860X(95)00201-4.

[17] Xu J, Zhou W, Li Z, Wang J, Ma J. Biogas reforming for hydrogen production over nickel and cobalt bimetallic catalysts. Int J Hydrogen Energy 2009;34:6646–54. https://doi.org/10.1016/j.ijhydene.2009.06.038.

[18] San-José-Alonso D, Juan-Juan J, Illán-Gómez MJ, Román-Martínez MC. Ni, Co and bimetallic Ni-Co catalysts for the dry reforming of methane. Appl Catal A Gen 2009;371:54–9. https://doi.org/10.1016/j.apcata.2009.09.026.

[19] Xin J, Cui H, Cheng Z, Zhou Z. Bimetallic Ni-Co/SBA-15 catalysts prepared by urea co-precipitation for dry reforming of methane. Appl Catal A Gen 2018;554:95–104. https://doi.org/10.1016/j.apcata.2018.01.033.

[20] Erdogan B, Arbag H, Yasyerli N. SBA-15 supported mesoporous Ni and Co catalysts with high coke resistance for dry reforming of methane. Int J Hydrogen Energy 2018;43:1396–405. https://doi.org/10.1016/j.ijhydene.2017.11.127.

[21] Zhang J, Li F. Coke-resistant Ni at SiO2 catalyst for dry reforming of methane. Appl Catal B 2015;176–177:513–21. https://doi.org/10.1016/j.apcatb.2015.04.039.

[22] Plata JJ, Graciani J, Evans J, Rodriguez JA, Sanz JF. Cu Deposited on CeOx-Modified TiO2(110): Synergistic Effects at the Metal-Oxide Interface and the Mechanism of the WGS Reaction. ACS Catal 2016;6:4608–15. https://doi.org/10.1021/acscatal.6b00948.

[23] Chein RY, Fung WY. Syngas production via dry reforming of methane over CeO2 modified Ni/Al2O3 catalysts. Int J Hydrogen Energy 2019;44:14303–15. https://doi.org/10.1016/j.ijhydene.2019.01.113.

[24] Zhang X, Zhang Q, Tsubaki N, Tan Y, Han Y. Influence of Zirconia Phase on the Performance of Ni / ZrO 2 for 2015.

[25] Roh HS, Potdar HS, Jun KW, Kim JW, Oh YS. Carbon dioxide reforming of methane over Ni incorporated into Ce-ZrO 2 catalysts. Appl Catal A Gen 2004;276:231–9. https://doi.org/10.1016/j.apcata.2004.08.009.

[26] Juan-Juan J, Román-Martínez MC, Illán-Gómez MJ. Effect of potassium content in the activity of K-promoted Ni/Al 2O3 catalysts for the dry reforming of methane. Appl Catal A Gen 2006;301:9–15. https://doi.org/10.1016/j.apcata.2005.11.006.

[27] Monteiro WF, Vieira MO, Calgaro CO, Perez-Lopez OW, Ligabue RA. Dry reforming of methane using modified sodium and protonated titanate nanotube catalysts. Fuel 2019;253:713–21. https://doi.org/10.1016/j.fuel.2019.05.019.

[28] Owgi AHK, Jalil AA, Hussain I, Hassan NS, Hambali HU, Siang TJ, et al. Catalytic systems for enhanced carbon dioxide reforming of methane: a review. Environ Chem Lett 2021;19:2157–83. https://doi.org/10.1007/s10311-020-01164-w.

[29] Xu B, Fan Y, Zhang Y, Tsubaki N. Pore diffusion simulation model of bimodal catalyst for Fischer-Tropsch synthesis. AIChE Journal 2005;51:2068–76. https://doi.org/10.1002/aic.10469.

[30] Ma Q, Han Y, Wei Q, Makpal S, Gao X, Zhang J, et al. Stabilizing Ni on bimodal mesoporous-macroporous alumina with enhanced coke tolerance in dry reforming of methane to syngas. Journal of CO2 Utilization 2020;35:288–97. https://doi.org/10.1016/j.jcou.2019.10.010.

[31] Taguchi A, Schüth F. Ordered mesoporous materials in catalysis. vol. 77. 2005. https://doi.org/10.1016/j.micromeso.2004.06.030.

[32] Abdulkareem Ghassan A, Mijan N-A, Hin Taufiq-Yap Y. Nanomaterials: An Overview of Nanorods Synthesis and Optimization. Nanorods and Nanocomposites 2020:1–24. https://doi.org/10.5772/intechopen.84550.

[33] Yu K, Zhang X, Tong H, Yan X, Liu S. Synthesis of fibrous monodisperse core-shell Fe3O 4/SiO2/KCC-1. Mater Lett 2013;106:151–4. https://doi.org/10.1016/j.matlet.2013.04.112.

[34] Ding C, Gao X, Han Y, Ma X, Wang J, Liu S, et al. Effects of surface states over core-shell Ni@SiO2 catalysts on catalytic partial oxidation of methane to synthesis gas. Journal of Energy Chemistry 2015;24:45–53. https://doi.org/10.1016/S2095-4956(15)60283-2.

[35] Owgi AHK, Jalil AA, Hussain I, Hambali HU, Nabgan W. Enhancing resistance of carbon deposition and reaction stability over nickel loaded fibrous silica-alumina (Ni/FSA) for dry reforming of methane. Int J Hydrogen Energy 2022. https://doi.org/10.1016/j.ijhydene.2021.12.134.

[36] Wang M, Zhang Q, Zhang T, Wang Y, Wang J, Long K, et al. Facile one-pot synthesis of highly dispersed Ni nanoparticles embedded in HMS for dry reforming of methane.

Chemical Engineering Journal 2017;313:1370–81. https://doi.org/10.1016/j.cej.2016.11.055.

[37] Naeem MA, Al-Fatesh AS, Fakeeha AH, Abasaeed AE. Hydrogen production from methane dry reforming over nickel-based nanocatalysts using surfactant-assisted or polyol method. Int J Hydrogen Energy 2014;39:17009–23. https://doi.org/10.1016/j.ijhydene.2014.08.090.

[38] Abdulrasheed AA, Jalil AA, Hamid MYS, Siang TJ, Fatah NAA, Izan SM, et al. Dry reforming of methane to hydrogen-rich syngas over robust fibrous KCC-1 stabilized nickel catalyst with high activity and coke resistance. Int J Hydrogen Energy 2019:1–13. https://doi.org/10.1016/j.ijhydene.2019.04.126.

[39] Usman M, Wan Daud WMA, Abbas HF. Dry reforming of methane: Influence of process parameters - A review. Renewable and Sustainable Energy Reviews 2015;45:710–44. https://doi.org/10.1016/j.rser.2015.02.026.

[40] Abdullah N, Ainirazali N, Chong CC, Razak HA, Setiabudi HD, Jalil AA, et al. Influence of impregnation assisted methods of Ni/SBA-15 for production of hydrogen via dry reforming of methane. Int J Hydrogen Energy 2019. https://doi.org/10.1016/j.ijhydene.2019.09.089.

[41] Ashok J, Raju G, Reddy PS, Subrahmanyam M, Venugopal A. Catalytic decomposition of CH4 over Ni-Al2O3-SiO2 catalysts: Influence of pretreatment conditions for the production of H2. Journal of Natural Gas Chemistry 2008;17:113–9. https://doi.org/10.1016/S1003-9953(08)60036-5.

[42] Figueredo GP, Medeiros RLBA, Macedo HP, de Oliveira ÂAS, Braga RM, Mercury JMR, et al. A comparative study of dry reforming of methane over nickel catalysts supported on perovskite-type LaAlO3 and commercial A-Al2O3. Int J Hydrogen Energy 2018;43:11022–37. https://doi.org/10.1016/j.ijhydene.2018.04.224.

[43] Liotta LF, Wu H, Pantaleo G, Venezia AM. Co3O4 nanocrystals and Co3O 4-MOx binary oxides for CO, CH4 and VOC oxidation at low temperatures: A review. Catal Sci Technol 2013;3:3085–102. https://doi.org/10.1039/c3cy00193h.

[44] Littlewood P, Liu S, Weitz E, Marks TJ, Stair PC. Ni-alumina dry reforming catalysts: Atomic layer deposition and the issue of Ni aluminate. Catal Today 2020;343:18–25. https://doi.org/10.1016/j.cattod.2019.03.040.

[45] Huang X, Xue G, Wang C, Zhao N, Sun N, Wei W, et al. Highly stable mesoporous NiO-Y2O3-Al2O3 catalysts for CO2 reforming of methane: Effect of Ni embedding and Y2O3 promotion. Catal Sci Technol 2016;6:449–59. https://doi.org/10.1039/c5cy01171j.

[46] Li J, Miao P, Li Z, He T, Han D, Wu J, et al. Hydrothermal synthesis of nanocrystalline H[Fe, Al]ZSM-5 zeolites for conversion of methanol to gasoline. Energy Convers Manag 2015;93:259–66. https://doi.org/10.1016/j.enconman.2015.01.031.

[47] Pinheiro AN, Valentini A, Sasaki JM, Oliveira AC. Highly stable dealuminated zeolite support for the production of hydrogen by dry reforming of methane. Appl Catal A Gen 2009;355:156–68. https://doi.org/10.1016/j.apcata.2008.12.007.

[48] Owgi AHK, Jalil AA, Aziz MAA, Nabgan W, Hassan NS, Hussain I, et al. The preferable Ni quantity to boost the performance of FSA for dry reforming of methane. Fuel 2023;332. https://doi.org/10.1016/j.fuel.2022.126124.

[49] de Freitas Silva T, Reis CGM, Lucrédio AF, Assaf EM, Assaf JM. Hydrogen production from oxidative reforming of methane on Ni/γ-Al2O3 catalysts: Effect of support promotion with La, La-Ce and La-Zr. Fuel Processing Technology 2014;127:97–104. https://doi.org/10.1016/j.fuproc.2014.06.002.

[50] Kumar P, Sun Y, Idem RO. Comparative study of Ni-based mixed oxide catalyst for carbon dioxide reforming of methane. Energy and Fuels 2008;22:3575–82. https://doi.org/10.1021/ef800326q.

[51] Budiman AW, Song SH, Chang TS, Shin CH, Choi MJ. Dry Reforming of Methane Over Cobalt Catalysts: A Literature Review of Catalyst Development. Catalysis Surveys from Asia 2012;16:183–97. https://doi.org/10.1007/s10563-012-9143-2.

[52] Licciulli A, Notaro M, Santis S de, Terreni C, Kunjalukkal S. CO 2 capture on amine impregnated mesoporous alumina-silica mixed oxide spheres. Fuel Processing Technology 2017;166:202–8. https://doi.org/10.1016/j.fuproc.2017.06.009.

[53] Daniell W, Schubert U, Glöckler R, Meyer A, Noweck K, Knözinger H. Enhanced surface acidity in mixed alumina-silicas: a low-temperature FTIR study. vol. 196. 2000.

[54] Omata K, Nambu T. Catalysis of water molecules acting as Brönsted acids at Lewis acid sites on niobium oxide. Appl Catal A Gen 2020;607. https://doi.org/10.1016/j.apcata.2020.117812.

[55] Ding L, Li M, Zhao Y, Zhang H, Shang J, Zhong J, et al. The vital role of surface Brönsted acid/base sites for the photocatalytic formation of free ·OH radicals. Appl Catal B 2020;266. https://doi.org/10.1016/j.apcatb.2020.118634.

[56] Hambali HU, Jalil AA, Abdulrasheed AA, Siang TJ, Abdullah TAT, Ahmad A, et al. Fibrous spherical Ni-M/ZSM-5 (M: Mg, Ca, Ta, Ga) catalysts for methane dry reforming: The interplay between surface acidity-basicity and coking resistance. Int J Energy Res 2020:1–17. https://doi.org/10.1002/er.5327.

[57] sheng1994 n.d.

[58] Wood DL, Rabinovich EM. HEAT EVOLUTION, LIGHT SCAITERING, AND INFRARED SPECTROSCOPY IN THE FORMATION OF SILICA GELS FROM ALKOXIDES. vol. 107. 1989.

[59] Marie O, Massiani P, Thibault-Starzyk F. Infrared Evidence of a Third Brønsted Site in Mordenites. Journal of Physical Chemistry B 2004;108:5073–81. https://doi.org/10.1021/jp037915v.

[60] Montanari T, Marie O, Daturi M, Busca G. Cobalt on and in zeolites and silica-alumina: Spectroscopic characterization and reactivity. Catal Today, vol. 110, 2005, p. 339–44. https://doi.org/10.1016/j.cattod.2005.09.034.

[61] Chong CC, Teh LP, Setiabudi HD. Syngas production via CO 2 reforming of CH 4 over Ni-based SBA-15: Promotional effect of promoters (Ce, Mg, and Zr). Mater Today Energy 2019;12:408–17. https://doi.org/10.1016/j.mtener.2019.04.001.

[62] Chen BH, Chao ZS, He H, Huang C, Liu YJ, Yi WJ, et al. Towards a full understanding of the nature of Ni(II) species and hydroxyl groups over highly siliceous HZSM-5 zeolite supported nickel catalysts prepared by a deposition-precipitation method. Dalton Transactions 2016;45:2720–39. https://doi.org/10.1039/c4dt00399c.

[63] Zhang RJ, Xia GF, Li MF, Wu Y, Nie H, Li DD. Effect of support on catalytic performance of Ni-based catayst in methane dry reforming. Ranliao Huaxue Xuebao/Journal of Fuel Chemistry and Technology 2015;43:1359–65. https://doi.org/10.1016/S1872-5813(15)30040-2.

[64] San-José-Alonso D, Juan-Juan J, Illán-Gómez MJ, Román-Martínez MC. Ni, Co and bimetallic Ni-Co catalysts for the dry reforming of methane. Appl Catal A Gen 2009;371:54–9. https://doi.org/10.1016/j.apcata.2009.09.026.

[65] Rodriguez JA, Liu P, Wang X, Wen W, Hanson J, Hrbek J, et al. Water-gas shift activity of Cu surfaces and Cu nanoparticles supported on metal oxides. Catal Today 2009;143:45–50. https://doi.org/10.1016/j.cattod.2008.08.022.

[66] Shido T, Asakura K. Reactant-Promoted Reaction Mechanism for Catalytic Water-Gas Shift Reaction on MgO. vol. 122. 1990.

[67] Chen W, Zhao G, Xue Q, Chen L, Lu Y. High carbon-resistance Ni/CeAlO3-Al2O3 catalyst for CH4/CO2 reforming. Appl Catal B 2013;136–137:260–8. https://doi.org/10.1016/j.apcatb.2013.01.044.

[68] Chong CC, Bukhari SN, Cheng YW, Setiabudi HD, Jalil AA, Phalakornkule C. Robust Ni/Dendritic fibrous SBA-15 (Ni/DFSBA-15) for methane dry reforming: Effect of Ni loadings. Appl Catal A Gen 2019;584. https://doi.org/10.1016/j.apcata.2019.117174.

[69] Ribeiro NFP, Neto RCR, Moya SF, Souza MMVM, Schmal M. Synthesis of NiAl2O4 with high surface area as precursor of Ni nanoparticles for hydrogen production. Int J Hydrogen Energy 2010;35:11725–32. https://doi.org/10.1016/j.ijhydene.2010.08.024.

[70] Moradi G, Khezeli F, Hemmati H. Syngas production with dry reforming of methane over Ni/ZSM-5 catalysts. J Nat Gas Sci Eng 2016;33:657–65. https://doi.org/10.1016/j.jngse.2016.06.004.

[71] Hambali HU, Jalil AA, Abdulrasheed AA, Siang TJ, Vo DVN. Enhanced dry reforming of methane over mesostructured fibrous Ni/MFI zeolite: Influence of preparation methods. Journal of the Energy Institute 2020. https://doi.org/10.1016/j.joei.2020.01.016.

[72] Nguyen TGH, Tran DL, Sakamoto M, Uchida T, Sasaki K, To TD, et al. Ni-loaded (Ce,Zr)O2–Δ-dispersed paper-structured catalyst for dry reforming of methane. Int J Hydrogen Energy 2018;43:4951–60. https://doi.org/10.1016/j.ijhydene.2018.01.118.

[73] Zhang Y, Tao Y, Huang J, Williams P. Influence of silica–alumina support ratio on H2 production and catalyst carbon deposition from the Ni-catalytic pyrolysis/reforming of waste tyres. Waste Management and Research 2017;35:1045–54. https://doi.org/10.1177/0734242X17722207.

[74] Gurav HR, Dama S, Samuel V, Chilukuri S. Influence of preparation method on activity and stability of Ni catalysts supported on Gd doped ceria in dry reforming of methane. Journal of CO2 Utilization 2017;20:357–67. https://doi.org/10.1016/j.jcou.2017.06.014.

[75] Meng J, Gu T, Pan W, Bu C, Zhang J, Wang X, et al. Promotional effects of defects on Ni/HAP catalyst for carbon resistance and durability during dry reforming of methane. Fuel 2022;310:122363. https://doi.org/10.1016/j.fuel.2021.122363.

[76] Zhang ZL, Verykios XE. Carbon dioxide reforming of methane to synthesis gas over supported Ni catalysts. Catal Today 1994;21:589–95. https://doi.org/10.1016/0920-5861(94)80183-5.

[77] Han JW, Park JS, Choi MS, Lee H. Uncoupling the size and support effects of Ni catalysts for dry reforming of methane. Appl Catal B 2017;203:625–32. https://doi.org/10.1016/j.apcatb.2016.10.069.

[78] Serrano-Lotina A, Daza L. Highly stable and active catalyst for hydrogen production from biogas. J Power Sources 2013;238:81–6. https://doi.org/10.1016/j.jpowsour.2013.03.067.

[79] Navalikhina MD, Kavalerskaya NE, Lokteva ES, Peristyi AA, Golubina E v., Lunin V v. Hydrodechlorination of chlorobenzene on Ni and Ni-Pd catalysts modified by heteropolycompounds of the keggin type. Russian Journal of Physical Chemistry A 2012;86:1669–75. https://doi.org/10.1134/S0036024412110192.

[80] Phan TS, Sane AR, Rêgo de Vasconcelos B, Nzihou A, Sharrock P, Grouset D, et al. Hydroxyapatite supported bimetallic cobalt and nickel catalysts for syngas production from dry reforming of methane. Appl Catal B 2018;224:310–21. https://doi.org/10.1016/j.apcatb.2017.10.063.

Methane dry reforming on fibrous silica-alumina employing nanocrystals of nickel and cobalt to recognize the most efficient metal

A.H.K. Owgi [b], A.A. Jalil [a, b, c*], M.A.A. Aziz[a, b], W. Nabgan [d], M. Alhassan [b,f], M.H.M. Sofi [b], N.S. Hassan [b], R. Saravanan [e], M. B. Bahari [b].

[a] *Centre of Hydrogen Energy, Institute of Future Energy, 81310 UTM Johor Bahru, Johor.*

[b] *Faculty of Chemical and Energy Engineering, Faculty of Engineering, Universiti Teknologi Malaysia, 81310 UTM Johor Bahru, Johor, Malaysia.*

[c] *Saveetha School of Engineering, Saveetha Institute of Medical and Technical Science, Chennai 60210, India*

[d] *Departament d'Enginyeria Qu´ımica, Universitat Rovira I Virgili, Av Pa¨ısos Catalans 26, 43007, Tarragona, Spain.*

[e] *Faculty of Engineering, Department of Mechanical Engineering, University of Tarapacá, Avda, General Velasquez, 1775 Arica, Chile.*

[f] *Department of Chemistry, Sokoto State University, PMB 2134, Airport Road, Sokoto, Nigeria*

**To whom correspondence should be addressed,*

Aishah Abdul Jalil (Ph.D.)

Tel: 60-7-5535581 Fax: 60-7-5536165

Email: aishahaj@utm.my

Abbreviation.

(GHGs):	Greenhouse gas.
(DRM):	Dry reforming of methane.
(FSA):	Fibrous silica-alumina.
(CTAB):	Cetrimonium bromide.
(TEOS):	Tetraethyl orthosilicate.
(XRD):	X-ray diffractograms.
(XRF):	X-ray fluorescence
(FESEM):	Field emission scanning electron microscopy.
(FTIR):	Fourier-transform infrared.
(TEM):	Transmission electron microscopy.
(H_2-TPR):	H_2 temperature program reduction.
(TGA):	Thermogravimetric analysis.
(GC):	Gas chromatography.
(BET):	Brunauer-Emmett-Teller.
(C-NTs):	Carbon nanotubes
(D-band):	Disorder-generated band
(G-band):	Graphite carbon band
(TCD):	Thermal conductivity detector
(NLDFT):	Non-local density functional theory
(TO):	Transverse-optical
(LO):	Longitudinal-optical

ABSTRACT

Presently, the production of syngas through the dry reforming of methane is a widely employed approach for reducing vast amounts of greenhouse gas emissions. Several metals, particularly transition metals support have been evaluated as active DRM catalyst systems. In this work, a comparative studies is presented between Cobalt and Nickel metals impregnated over fibrous silica-alumina (FSA) support synthesized by the hydrothermal method for dry methane reforming. The specimens were characterized via FESEM mapping, TEM, XRD, H_2-TPR, XRF, N_2 physisorption, and KBr-FTIR techniques. Unlike the Co/FSA, Ni/FSA displayed a higher surface area with a fine dispersion of Ni nano-crystalline and less agglomeration, and more active sites which enhanced the metal-support interaction. Approximately 0.2g of each catalyst was evaluated at 650 - 800 ºC with a respective. CH_4:CO_2:N_2 ratio of 1:1:2, gas hourly space velocity 30,000 mL g^{-1} h^{-1}. The Ni/FSA demonstrated more conversion of CH_4 (89%) over (67%) of Co/FSA at 800ºC. After 10 h of long-term reaction, the Ni/FSA exhibited more stability at 800 ºC. TGA/DTA, Raman, and TEM results showed that spent Ni/FSA catalysts did not demonstrate signs of considerable nano-graphitic carbon or metal sintering as compared to Co/FSA catalysts, which had bigger crystallites of Co. The finding of this study would add new knowledge on reaction conditions involving and catalytic activities of the metals over the FSA.

Keywords: cobalt, nickel; carbon resistance; methane dry reforming; Fibrous silica-alumina.

1.0 Introduction

In recent years, there has been a great deal of interest in the dry reforming of methane, which is the conversion of the major negative component of fossil fuel emissions, (CO_2 and CH_4), which is pose a serious environmental issue into synthesis gas with an H_2/CO ratio of unity, which is used to produce synthetic fuel [1–3]. This procedure is incredibly significant to the environment as the GHGs utilized as gas sources are methane and carbon dioxide, all of which are harmful greenhouse gases. It has been suggested that dry reforming of methane (DRM) is a preferable option to producing syngas (H_2/CO≈1) since it can decrease CO_2 emissions while producing beneficial raw materials [2]. To enhance DRM at the industrial scale, three fundamental aspects must be addressed: (1) improved carbon dioxide and methane activation; (2) the improved comprehension of the mechanisms and reaction processes that create H_2 and CO; and (3) strategies to prevent deactivation of catalyst operations [4,5].

In the Fischer-Tropsch synthesis, a feedstock gas combination containing a low H_2/CO ratio is preferred for the creation of hydrocarbon fuels [6–8]. To achieve appropriate conversion levels, the endothermic aspect of the reaction necessitates a high reaction temperature. Because of the considerable operational temperature, adequate catalysts are required. The creation and build-up of carbonaceous deposits typically lead to the sintering of metal particles followed by the deactivation of catalysts as a consequence of the excessive temperature [9–13]. Recently, it is proven that noble metals including platinum, rhodium, and ruthenium, as well as non-noble metals as transaction metals (Ni, Co, and Fe), are employable as catalysts in dry reforming processes[9,10]. According to reports, noble metals possess excellent catalytic activity and have insignificant coking potential. However, due to their restricted variety and expensive cost, they are not widely used in the industrial sector.

Because of their cheaper cost and equivalent catalytic efficiency, non-noble metals such as nickel and cobalt have attracted the curiosity of researchers [4,14–16].

Despite the great catalytic performance demonstrated by nickel-based catalysts, the significant coking and swift inactivation prevent them from being used in industrial applications. Cobalt catalysts for example, possess a considerable soot oxidation ability which could be employed to increase the resistance of a catalytic process to carbon production by reducing the coke formation. Nonetheless, cobalt catalysts exhibit a high proclivity for re-oxidation, resulting in low performance [17–20].

The majority of the recent investigations in this area are primarily focused on reducing carbon creation in a variety of methods, either by ; i) using supports that have high oxygen ion mobility which may interact with adsorbed carbon species, such as SiO_2, CeO_2, and ZrO_2 solid solutions, as opposed to conventional supports[21–25]; ii) the employment of additives such as potassium or sodium, which provide basic aspects to the surface characteristics, despite the reality that they reduce the catalytic activity[26,27]. iii) modifying the morphologies of support specifically bimodal, mesoporous, nanorods, core-shell, nano-fibrate, and fibrous dendrimers [28–34]. The fabrication of incredibly multifunctional supported metal catalysts by wide metal dispersion of nanoparticles is one of the crucial options for heterogeneous catalytic systems that require research. Our prior research on the successful growth of fibrous silica-alumina (FSA) via exceptional surface area and thermal stability was the inspiration for this study [35]. In the present study, the FSA was investigated for DRM and the performance of the metals (Ni and Co) loaded over FSA aiming at getting a greater understanding of the metal's impact on catalytic efficiency and carbon formation.

2.0 Experimental

2.1 Catalyst Preparation

Fibrous silica-alumina support has been generated through the hydrothermal method and Al_2O_3. Alumina nitrate (Sigma-Aldrich, > 98%) was combined into a homogenous mixture of n-butanol (Merck, > 98%) and toluene (Sigma-Aldrich, > 98%). Afterward, the solution was stirred for approximately 30 min prior to introducing TEOS (Merck, > 98%) and was poured dropwise. Urea (Merck, > 98%), Cetrimonium bromide (CTAB- Sigma-Aldrich, > 98%), and 0.75 L of deionized water were added to the mixture. Toluene/1-butanol=13.8, urea/CTAB=3.8, and Si/Al=1.23 are the essential variables. While being exposed to microwave radiation at 400 W for 360 min, the subject substance was vaporized at 120 ℃ for overnight evaporation. The white specimen was heated in a furnace for 360 min at 550 C to produce FSA support.

2.2 Loading Metals

To load metals onto FSA, a 5 wt% Co and Ni-impregnated solution of $Co(NO_3)_2$ and Ni $(NO_3)_{2.6}H_2O$ were (% trace metals) used as purchased from Sigma-Aldrich. Bhd. They dissolved in deionized water was deployed. Before getting impregnated, the specimens were evaporatively dried and then calcined for three hours at 550 °C. Co/FSA and Ni/FSA were the end products of this procedure.

2.2 Characterization

A Bruker D8 Advance diffraction pattern, Which was certified utilizing Cu K-ray radiation at 1.54 wavelengths, was employed to conduct the XRD study on pristine and spent samples. The determination is intended to generate X-ray diffractograms in the range of 1-280º employing data at 0.05º and 0.1º at 46kV and 41mA. (FESEM; Zeiss Supra VP35) field emission scanning electron microscopy was deployed to further analyze the structure of samples. N_2 adsorption-desorption through ASAP2020 apparatus was using an N_2/He mixed gas and a from Micromeritics to determine surface areas. 0.1– 0.15 g of the specimen were refluxed at 200 °C for 240 min before the assessment, followed cooled to room temperature. The BET technique was employed to calculate the total surface area. Additionally, Fourier-transform infrared (FTIR) measurements were conducted on the materials using the Agilent Technology Varian 670 apparatus at 30 ℃ in the 400 to 4000 cm^{-1} wavelength range. By using a Rigaku Primus 2 apparatus and lithium tetraborate to treat the materials, the metal percentage was evaluated using wavelength-dispersive X-ray fluorescence (XRF).

The carbon-containing aggregate structuring in the utilized catalysts was examined by adopting 510nm lasers with a 50x magnified microscope mounted on a Renishaw via a Raman spectrophotometer, The Raman spectra of the specimen were recorded around 1000 and 2200 cm^{-1}. A TGA/SDTA 851e Mettler Toledo thermo-gravimetric instrument with a temperature range of 5-950 ℃ and a heating rise of 10 ℃/min with airflow has also been employed to assess carbon deposits. Additionally, utilizing JEOL JEM-2100 F technology, transmission electron microscopy (TEM) was conducted on the spent samples. All of the materials were acetone-liquefied before being positioned on a copper gridiron that had a penetrable carbon layer covering it. Temperatures of 100 to 1000℃ and an H_2/N_2 flow rate with a concentration of 10% were employed to investigate the reduced specimen (20 mL min^{-1}).

2.3 Catalyst assessment

The DRM assessments were carried out on various catalysts using a series of efficiency measurements at a temperature limitation of 500-850 ℃ through streaming the gases in a fixed-bed reactor to identify the detrimental impacts of the metals on the long-term catalyst performance. The catalysts were tested employing a stream running continuously in a reactor at environmental pressure and a heat range of 500–850 ºC. A portion of the pelletized catalyst (2mg) was placed in a reactor, blocked by quartz wool. Before the activity, the preload catalyst was initially treated with 15 mL min^{-1} oxygen at 700 ℃ for 60 min, followed by 100 $ml.min^{-1}$ at 800 ºC throughout 120 min of H_2:N_2 (50:50). Then the reactor was cooled to a set temperature as a function of the impacts of N_2. The reactor was supplied with the mixture of gases CO_2: CH_4: N_2 at 25:25:50 $ml.min^{-1}$ rate. To continuously monitor and evaluate the surplus reactant and gas released, (Agilent 7890A GC) a gas chromatograph set via a (1010)column carboxy with a 0.1L collecting band with thermal detecting was employed (TCD). Before a randomized choice was determined, 60 minutes were required for reaching the reaction equilibrium at the examined temperature. Equations (1-7) were employed to estimate the rate of conversions and the ratio of syngas (H_2/CO) [9,36,37].

Conversion of CH_4 $= \frac{F_{(CH4)in} - F_{(CH4)out}}{F_{(CH4)in}} \times 100$ (1)

Conversion of CO_2 $= \frac{F_{(CO2)in} - F_{(CO2)out}}{F_{(CO2)in}} \times 100$ (2)

H_2/CO $= \frac{F(H_2)out}{F\ (CO)out}$ (3)

H_2 Selectivity $= \frac{F_{(H2)out}}{2\ [\ F_{(CH4)in} - F_{(CH4)out}]} \times 100$ (4)

CO Selectivity $= \frac{F_{(CO)out}}{[\ F_{(CH4)in} - F_{(CH4)out}] + [\ F_{(CO2)in} - F_{(CO2)out}]} \times 100$ (5)

H_2 Yield $= \frac{F(H_2)out}{2 \times F\ (CH)4in}$ (6)

CO Yield $= \frac{F_{(CO)out}}{F_{(CH4)in} - F_{(CO2)in}} \times 100$ (7)

3.0 Reflection on The Findings

3.1 Catalysts characterization

3.1.1 Characteristics of structure and morphology

Figure 1(A–C) displays FESEM micrographs including elements mapping of all specimens demonstrating the particle dispersion of metal. Figures 1(A) depict the creation of the fibrous silica-alumina structure's expected spherical bi-continuous concentric fibrillar shape. NiO and CoO crystallite scattering and sizes were soft purple spots evident scattered over the support structure. The particle sizes, as determined from the XRD spectra using the Scherrer equation, are 11.7nm and 14.3nm for Ni and Co FSA catalysts respectively. For this reason, the Co is less spread on the surface of the FSA than Ni/FSA [38]. The Co was inadequately diffused on the fibrous silica-alumina (Fig. 1C), due to its limited pores as well

as surface area, as shown by the lumps of Co on the surface of the FSA after impregnation. This being the cause of rapid Co/ FSA inactivation during only short hours on the stream cannot be outweighed. Because of the limited distribution of Co, there is a limited surface for reaction and reduction, resulting in significant sintering due to tiny crystallite migration. Consequently, the deactivation potential of the catalyst will be larger based on the amount of carbon placed [5,12,39]. Moreover, Traces of cobalt and nickel were observed via catalysts are 5.10% and 4.84% respectively by XRF analysis (in the Table.1), The amounts of Ni-loading at 5% wt are consistent with the quantities employed during catalyst preparations, and the identifying amounts of compounds utilized in this investigation are true.

Figure .2. displays the crystalline structures through the X-ray diffraction (XRD) for the specimens FSA, Ni/FSA, and Co/FSA. All the samples demonstrated a broad 2θ band from 20 to 30º, this is often attributed to the amorphous phase of SiO_2 (JCPDS card No. 29-0085)[40,41]. Because of the existence of silica species during the fabrication of dendrimeric silica fibres, the XRD pattern intensity diminished. The Ni and Co FSA catalysts both exhibited nine prominent peaks at 2θ value of 25.8°, 35.4°, 37.8°, 43.5°, 52.8°, 57.5°, 66.7°, 68.4°, and 77.1° identical to the (0 1 2), (1 0 4), (1 1 0), (1 1 3), (0 2 4), (1 1 6), (2 1 4), (3 00), and (1 1 9) alumina crystalline planes via structures of rhombohedral (JCPDSICDD File No 46-1212) for FSA sample [35,42].

Three diffraction peaks were seen for NiO via Ni/FSA at 2θ = 62.9, 75.4, and 79.4°, correlating to NiO planes (2 20), (2 2 2), and (3 1 1), respectively (JCPDS 78-0643). The Co_3O_4, Co/FSA showed five peaks at 2θ = 18.6, 31.3, 36.8, 44.8, and 59.4°, which corresponded to (111), (2 2 0), (3 1 1), (4 0 0), and (511), respectively (JCPDS 42-1467)[43]. The diffraction peak intensity was found to be lower in Ni/FSA in comparison to Co/FSA. As revealed by the FESEM studies; moreover, the nano-crystallite metals of NiO deposited on FSA were uniformly distributed more than Co_3O_4. Owing to the active site mobility

obtainable through FSA, which enables NiO scattering, the possibility for NiO crystal aggregation and the metal-support interaction is increased [44]. Moreover, the peaks of Ni-Al_2O_4 appeared less higher than that of Co-Al_2O_4 indicating more crystallinity of Co over Ni

3.1.2 Textural properties

N_2 adsorption-desorption analysis was used to investigate the textural properties of the FSA, Ni/FSA, and Co/FSA. Figure.3 shows the N_2 adsorption-desorption isotherms including pore size dispersion of the catalysts. Referring to the IUPAC categorization, the catalyst isotherms displayed regular type IV adsorption phases at P/Po = 0.4, and 0.9, indicating a mesoporous property [45,46]. The scattering of pore sizes overall catalysts is illustrated in the figure.3 implementing (NLDFT) non-local density functional theory.

The FSA revealed a sharp peak in the 50-70 (Å) range and a thin peak in the 100-200 (Å) band for mesopore distribution. The high peak is due to the formation of mesopores during surfactant self-assembly. However, the small peaks are owing to the spacing between dendrimeric molecules. When Ni/FSA was compared to FSA, there was no substantial shift in pore dispersion. This attests to a real dispersion of Ni dispersion confirmed by FESEM (Fig. 1). However, the peak intensity of pore dispersion is decreased by adding Co. This finding is linked to a decrease in the amount of adsorbed N_2 in Co/FSA P/Po = 0.46–1.0, indicating a decrease in micropores and interparticle voids mesopores[47]. In the present study (Table.2), the FSA displayed (334.92 $m^2\ g^{-1}$) an extraordinary surface area, after loading Ni, the surface area increased to 338.54 $m^2\ g^{-1}$ because there was more scattering of active metal [48]. Moreover, increased Ni encasement over Ni/FSA indicates that dispersion has been optimized. As seen in figure 1. However, when Co was added to the FSA, the surface area and pore volume were reduced to 303.6 $m^2\ g^{-1}$ and 0.856 $cm^3\ g^{-1}$ respectively.

With the addition of Co, the catalysts' surface area and pore volume diminished due to partial pore blockage and/or pore filling.

3.1.3 Reducibility

TPR-H_2 of the calcined catalysts was performed to gain a deeper insight into the evolution of the nickel and cobalt phases as shown in figure.4. This was useful in determining the reduction degree of the Co and Ni oxide species. the solitary peak of Ni/FSA in the region from 260 ºC to 360 ºC correlates to Ni species reduction [49,50]. This is most definitely attributable to a reduction in narrower NiO nanoparticles or nickel aluminates as shown in the XRD result [44,49]. A low degree of reduction peak might imply that the interaction of NiOx species was slight with the exterior of FSA dendritic fibres.

There were two essential reduction stages in the Co/FSA catalyst's reduction studies. The reduction peak centred close to 300-510 ºC is assigned to free Co_3O_4 reduction.However, this involved consecutive reductions to CoO and metallic Co, respectively. A unique peak was identified between 560 and 770 ºC showing the occurrence of considerable quantities of $CoAl_2O_4$ obtained from the strong interaction between Co_3O_4 and Al_2O_3 [12,17,43,51].

3.1.4 Spectroscopic Studies

FTIR spectroscopy with wavelengths between 400 and 4000 cm-1, assessed the various construction heterogeneity of the (Co and Ni) supported FSA, as displyed in figure.5. The most prominent peaks exhibited siliceous frames because Si interacted with various atoms, (for instance, Si-O-Si, Si-OH, Si-O, Al-O-Al, and Si-O-Al) through the range 400–1300 cm^{-1}. [52]. The wavenumbers of five peaks 1240, 1090, 960, 790, also 460 cm^{-1} were demonstrated in all specimens, indicative of Si-O-Si bond apparent within the range of 960-1260 cm^{-1} in all samples [53]. Similar, all catalysts in fig.5 demonstrated a peak at 3400 cm^{-1} indicative of that O-H-stretching vibration due to water molecules, or Brønsted acid sites

which are dependent on hydrogen concentration [54,55]. As displayed by the same figure, Ni/FSA possess a low-intensity peak at 3400 cm^{-1} reflected in low Brønsted acid sites. Furthermore, asymmetric stretching peak attributed to Si-O-Si transverse-optical (TO) and longitudinal-optical (LO) bands were apparent at approximately 1240 cm^{-1} and 1090 cm^{-1}, respectively [56–58]. The weak bands at 960 and 1640 cm^{-1} were assigned to external groups of Si-OH, whilst symmetric and asymmetric Al-O and Si-O stretch vibrations were pronounce at 800 cm^{-1} and 462 cm^{-1}, respectively [59]. Apart from stretching vibrations, symmetrical and asymmetrical stretch attributable to Si-O-Al were reported by [60] 1090, 790 and 460 cm^{-1} .The disappearance of these peaks upon the introduction of Ni and Co to FSA, could imply that the Si–O–Si and Si-OH were partly replaced by Ni–O–Si, Co–O–Si, Ni-O, and Co–O. In particular, the peak at 666 cm^{-1} in the Co/FSA is attributable to Co–O vibrations indicating the successful incorporation of Co onto the support [17,41]. Accordingly, substituting result of the O–H and O–Si with the Ni ions in the dendritic fibrous FSA structure entails a greater reduction in peak density compared to the Co sample, emphasizing that Ni had a more robust interaction with FSA support than the Co [61,62].

3.2 Activity Evaluation

Figure.6 shows the activity results of Ni/FSA and Co/FSA. Ni/FSA converted more CH_4 than Co/FSA under identical reaction conditions. Based on the fine Ni dispersion as seen in the FESEM picture, Ni/FSA catalysts were more efficient than Co/FSA catalysts, which enhanced the porosity and surface area, thereby providing a variety of active reaction sites and mobility of reactant mass in the process. Additionally, textural characteristics have a significant role in catalytic activity, as demonstrated by the FSA characteristics that supply the active species required to prevent deactivation of the catalyst (surface area, pore size, and

pore volume) [63]. Thus, owing to the extraordinary surface area of Ni/ FSA and possession of high oxygen storage deposits of C are easily transformed to CO thereby forming intermediates carbonate species into reductive basic supports reflected avoiding the coke formation [28].

The Ni/FSA catalyst shows superior catalytic efficacy, with the sustained conversion of CH_4 and CO_2 exceeding 89 % and 80 %, respectively, at 800 ºC, In comparison to Co/FSA (XCH_4= 67%, XCO_2 63%). Indeed, the tiny metal particles and superior metal diffusion will lead to more edges and metal-support frameworks, resulting in more active sites. Interestingly, the conversion of CH_4 and CO_2 at 700 were similar for the Ni/FSA and Co/FSA catalysts, indicating the possibility that side reactions such as; methane decomposition ($CH_4 \rightarrow C + 2H_2$) and the Boudouard reaction ($2CO \leftrightarrow C + CO_2$) have occurred [7,64].

To verify the successful Ni/FSA synthesis for DRM catalytic ability in comparison to the Co/FSA at 800 °C prolonged performance for 10 hours, the stabilization assessments were carried out as shown in fig.7 (A and B). Compared to Co/FSA (XCO_2 = 17%, XCH_4 = 21%), the FSA catalyst exhibits superior catalytic performance, with the stable CO_2 conversion and CH_4 achieving 91 % and 96 %, respectively. The catalytic performance of Co/FSA decreases during the second hour while on stream. This should be identified by the poor Co dispersion within surface aggregation and increased acidity that causes coke deposit and inactivation [28,51]. Moreover, the H_2/CO ratio for Co/FSA is lesser than that of Ni/FSA, achieving a ratio of 0.85 to 95 as depicted in Fig. 7C, which is appropriate for the Fischer-Tropsch application to synthesize lipid long hydrocarbons chain. This possibly is owing to the possibility of Ni/FSA to disperse oxygen species over the surface than Co/FSA catalyst [18,19,63]. According to Fig. 8, the H_2 yield showed a different trend with conversions, with Ni/FSA achieving the highest H_2 yields and Co/FSA achieving the lowest. Meanwhile, the exception of CO selectivity that appeared to be caused by the Co/FSA

catalyst could be explained by the RWGS reaction ($CO_2 + H_2 \leftrightarrow CO + H_2O$). where the H_2 and CO selectivity of Ni/FSA were quite similar, which were 48% of S (CO) and 51% of S (H_2) [65,66].

Simultaneous secondary reactions that occurred throughout catalytic testing were predictable. On the other hand, from the H_2/CO profiles as displayed in Fig. 7C, In actuality, a rise in the ratio of syngas on Ni/FSA after 6 hours was driven by the concomitant occurrence of CH_4 decomposition ($CH_4 \rightarrow C + 2H_2$) and CO disproportionation ($2CO \leftrightarrow C + CO_2$). These subsequent reactions neither simply influenced the syngas ratio, but also produced carbonaceous species that were detrimental to catalytic activity. On the contrary, in the first hours of the reaction, the syngas ratio was shown to drop for both specimens, which was caused by the reverse water gas shift (RWGS) reaction to the decrease in syngas ratio. and seem to improve with the favourability of thermodynamics [67,68].

The activity of Ni/FSA was preferable over that of Co/FSA, which might be attributed to its significant number of active sites via the mesoporous and microporous supplies by the support's fibrous temple. In particular, the characterization results show that the thinner crystallite of NiO is diffused homogeneously across the FSA compared to Co. However, Co has shown in FESEM more accumulation onto the FAS than Ni, as well as the Co particles having blocked the pores of the FSA the (Table. 2). This creates a tremendous contribution to increasing NiO engagement within the FSA and drastically enhancing the environmental basicity of catalysts. As stated previously, the catalysts' basicity assisted CO_2 decomposition and gasification while limiting CH_4 interactions with active sites, potentially minimizing coke formation during the long-term activity[69,70].

Interestingly, FTIR results show that the existence of a synergic influence among Nickle particles and fibrous silica-alumina mesostructures via the generation of Ni-O-Al and

Ni-O-Si bonds prevents the aggregation of metal. This coordinated impact shielded the metallic Ni^0 phase during the reduction of the NiO crystalline phase through the H_2 stream before the reaction begging, thus increasing the re-efficiency of both gaseous reactants, CH_4 and CO_2. The inferior catalytic efficacy of Co/FSA is probably attributed to the coke forming and possibly sintering metals during the DRM process [68,71].

3.3 Spent Characterization

During 10 hours of activation, the Raman spectra evidenced the distinct species of carbon extent in Fig. 9. The sp2-bonded carbon deposit is responsible for two peaks: the disorder-generated band (D-band) at 1350 cm^{-1} and the graphite carbon band (G-band) at 1584 cm^{-1} [38]. The G-to-D-band ratio (IG/ID) is a representation of the amount of carbon placed, which evaluates the quantity of graphitization of coke deposits. Consequently, a higher IG/ID ratio implies that graphitic carbon is being generated at an accelerated rate more highly than amorphous carbon and inconsistently, increases the catalyst's susceptibility to deactivation and complicates the renovation process [72]. The IG/ID ratios for Co/FSA and Ni/FSA were 1.02 and 0.9, respectively, confirming both carbons, graphitic and amorphous, were attended with both specimens. Raman spectra revealed that the Ni/FSA had the lowest IG/ID ratio and narrowest band zones throughout Raman wavelengths. This indicates that a small amount of carbon is deposited on Ni/FSA, while the maximum carbon achieves an amorphous and disordered formation that has little potential for catalyst disruption. The disordered carbon formations are mainly gasified throughout the DRM, preventing them from accumulating and developing into a more stable carbon deposit.

Coke coatings on the catalyst surface were evaluated using the TGA and DTA investigation, and the findings are displayed in Fig.10. The charts demonstrated the weight portion loss caused by the used catalysts, the amount of carbon formed, and the volume of

coke that might be replaced over the suppression mechanism of oxidation employing plenty of O_2 to form CO_2. For the Ni/FSA catalyst, the preliminary loss of weight happened at approximately 85°C and progressed at 4%. This demonstrates the formation of amorphous crbon, which is recognized to oxidize at lower temperatures compared to other carbons deposits, on the catalyst surface [73]. Observations in ancient times have proven that the size of the metal crystallization has a considerable impact on restricting carbon residue or elution, as catalysts with minimal metal crystalline phases release fewer cokes [74]. Additionally, the Raman and TGA analyses provided physical and quantifiable verification of the coke generation. The ease of oxidation exhibited by amorphous carbon over graphitic one made its impact after 10h on stream lesser [75]. On the contrary, the loss of weight particularly evident in Co/FSA, with a maximum value of peak position appearing at about 600 °C confirms the accumulation of exceptionally carbonaceous graphitic, which is challenging to gasify on-site. This carbon type has responsible for the rapid deactivation of Co/FSA, as shown by the stability evaluation (Fig. 7).

The DTG patterns can be subdivided into distinct peaks correspond to different types of carbon and are classes dignifed by the symbols Cγ, Cβ, and Cα [76]. The TGA profile was utilized to differentiate varieties in (Fig. 10B). Amorphous carbon (Cα) is oxidized at minimal temperatures to produce the syngas. Whereas, at extreme temperatures, Cγ and Cβ are oxidized, and those carbon sorts are actually involved in the mechanism of catalyst performance. The mass loss of roughly 100^{o}C recorded across all specimens is assigned to C, whereas the minor peak at 550^{o}C is related to Cβ, which is presumably formed by polymerization and rearrangement of active carbon species. At approximately 650 C, the weight losses were caused by crystalline carbon C, which is crucial for catalytic inactivation [77,78].

After 10 hours time on stream, the catalysts had not morphologically deformed and had sustained the FSA fibrosis (as shown in Fig.11). The Ni lattice fringes were discovered in the assessed quadrat space with lattice spacings of 0.18, 0.25, and 0.2 nm for the Ni/FSA specimen (Fig. 11B) and related to Ni (200), NiO (111), and Al_3Ni (301), respectively. Moreover, the lattice area which correlated to the Co_3O_4 (111), CoO (200), and Co (100) was 0.466, 0.213, and 0.208 nm, respectively in fig .11D. The lattice spacing of carbon interplanar was nonexistent on Ni/FSA provided evidence that carbon-graphite prevention was observed. Only on Co/FSA could different lattice fringes be seen that were related to carbon graphite and nanotubes with different levels of graphitization (Fig. 9D).

The formation of amorphous carbon disordered around the Ni nanoparticles is depicted (Fig.11A). The reaction indicated rapid gasification through oxygen vacancy to generate excess CO with no deactivation by coking. Consequently, it had minimal potential for accumulation in a long-term activity. Although the coke formation was insignificant after 10 hours of reaction, but the carbon nanotubes (C-NTs), whiskers, as well as amorphous coke species were visible on the spent Co/FSA, as evidenced by the TGA and Raman data. As shown in Figure 6, the apparent inactivity of Co/FSA during the early periods of the long-term reaction could be caused by the steady and structural carbon deposition and its lower sintering resistance as catalysts are more prone to inactivation if apprecible graphitic carbon is generated [41,79,80].

4.0 Conclusion

To conclude, fibrous silica-alumina (FSA) has been synthesized through the hydrothermal method with various loading metals by the impregnation method. In the KBr-FTIR and H_2-TPR investigations, the appearance of the degree of metal interactions was conditional on metal dispersion attributed to metal crystallite size on the support surface.

Accordingly, Ni/FSA generated superlative function in the DRM reaction across a temperature range of 500–850 °C and extraordinary stability over 10 h it due to its a large surface area (338.56 m^2/g), fine size dispersion of Ni, and strong metal-support interaction, as well as strong resistance to sintering by restricting Ni atoms or crystallite movements on the support. However, Co/FSA had a bigger crystallinite size, which affects the metal-support interaction reflected in the performance of the catalyst. The Ni/FSA catalyst serves as a coke inhibitor and a disordered amorphous phase with no effect on the catalyst stability. These characteristics are the vital causes for Ni/FSA catalyst's superior efficiency to Co/FSA synthesized via wet impregnation. As documented, the conversion of CH_4 was 97.5% for Ni/FSA, while it dramatically dropped to 20.63% for Co/FSA

Acknowledgment

The High Impact Research (UTMHR) Grant from Universiti Teknologi Malaysia funded this research project (08G92).

Reference

[1] Arbag H, Yasyerli S, Yasyerli N, Dogu G. Activity and stability enhancement of Ni-MCM-41 catalysts by Rh incorporation for hydrogen from dry reforming of methane. Int J Hydrogen Energy 2010;35:2296–304. https://doi.org/10.1016/j.ijhydene.2009.12.109.

[2] Gallego GS, Marín JG, Batiot-Dupeyrat C, Barrault J, Mondragón F. Influence of Pr and Ce in dry methane reforming catalysts produced from La1-xAxNiO3-δ perovskites. Appl Catal A Gen 2009;369:97–103. https://doi.org/10.1016/j.apcata.2009.09.004.

[3] Chong CC, Owgi AHK, Ainirazali N, Chin SY, Setiabudi HD. CO_2 reforming of CH_4 over Ni/SBA-15 prepared by surfactant-assisted impregnation method: Comparative study of surfactant types. Mater Today Proc 2018;5:21644–51. https://doi.org/10.1016/j.matpr.2018.07.014.

[4] Liu Z, Grinter DC, Lustemberg PG, Nguyen- Phan T, Zhou Y, Luo S, et al. Dry Reforming of Methane on a Highly- Active Ni- CeO_2 Catalyst: Effects of Metal- Support Interactions on C−H Bond Breaking . Angewandte Chemie 2016;128:7581–5. https://doi.org/10.1002/ange.201602489.

[5] Aramouni NAK, Touma JG, Tarboush BA, Zeaiter J, Ahmad MN. Catalyst design for dry reforming of methane: Analysis review. Renewable and Sustainable Energy Reviews 2018;82:2570–85. https://doi.org/10.1016/j.rser.2017.09.076.

[6] Takanabe K, Nagaoka K, Nariai K, Aika KI. Influence of reduction temperature on the catalytic behavior of Co/TiO_2 catalysts for CH4/CO2 reforming and its relation with titania bulk crystal structure. J Catal 2005;230:75–85. https://doi.org/10.1016/j.jcat.2004.11.005.

[7] Takanabe K, Nagaoka K, Nariai K, Aika KI. Titania-supported cobalt and nickel bimetallic catalysts for carbon dioxide reforming of methane. J Catal 2005;232:268–75. https://doi.org/10.1016/j.jcat.2005.03.011.

[8] Ruckenstein E, Wang HY. Carbon deposition and catalytic deactivation during CO_2 reforming of CH_4 over Co/γ -Al_2O_3 catalysts. J Catal 2002;205:289–93. https://doi.org/10.1006/jcat.2001.3458.

[9] Therdthianwong S, Therdthianwong A, Siangchin C, Yongprapat S. Synthesis gas production from dry reforming of methane over Ni/Al_2O_3 stabilized by ZrO_2. Int J Hydrogen Energy 2008;33:991–9. https://doi.org/10.1016/j.ijhydene.2007.11.029.

[10] Gao J, Hou Z, Guo J, Zhu Y, Zheng X. Catalytic conversion of methane and CO_2 to synthesis gas over a La_2O_3-modified SiO_2 supported Ni catalyst in fluidized-bed reactor. Catal Today 2008;131:278–84. https://doi.org/10.1016/j.cattod.2007.10.019.

[11] Hambali HU, Jalil AA, Abdulrasheed AA, Siang TJ, Owgi AHK, Aziz FFA. CO_2 reforming of methane over Ta-promoted Ni/ZSM-5 fibre-like catalyst: Insights on

deactivation behavior and optimization using response surface methodology (RSM). Chem Eng Sci 2021;231. https://doi.org/10.1016/j.ces.2020.116320.

[12] Fatah NAA, Jalil AA, Triwahyono S, Yusof N, Mamat CR, Izan SM, et al. Favored hydrogenation of linear carbon monoxide over cobalt loaded on fibrous silica KCC-1. Int J Hydrogen Energy 2020;45:9522–34. https://doi.org/10.1016/j.ijhydene.2020.01.144.

[13] Tran NT, van Le Q, van Cuong N, Nguyen TD, Huy Phuc NH, Phuong PTT, et al. La-doped cobalt supported on mesoporous alumina catalysts for improved methane dry reforming and coke mitigation. Journal of the Energy Institute 2020:1–10. https://doi.org/10.1016/j.joei.2020.01.019.

[14] Shiju NR. The Role of Metal-Support Bonding in Controlling the Particle Size of Ceria-Supported Transition Metal Catalysts. ChemCatChem 2011;3:112–4. https://doi.org/10.1002/cctc.201000357.

[15] Wang F, Xu L, Zhang J, Zhao Y, Li H, Li HX, et al. Tuning the metal-support interaction in catalysts for highly efficient methane dry reforming reaction. Appl Catal B 2016;180:511–20. https://doi.org/10.1016/j.apcatb.2015.07.001.

[16] Ruckenstein E, Hu YH. Carbon dioxide reforming of methane over nickel/alkaline earth metal oxide catalysts. Appl Catal A Gen 1995;133:149–61. https://doi.org/10.1016/0926-860X(95)00201-4.

[17] Xu J, Zhou W, Li Z, Wang J, Ma J. Biogas reforming for hydrogen production over nickel and cobalt bimetallic catalysts. Int J Hydrogen Energy 2009;34:6646–54. https://doi.org/10.1016/j.ijhydene.2009.06.038.

[18] San-José-Alonso D, Juan-Juan J, Illán-Gómez MJ, Román-Martínez MC. Ni, Co and bimetallic Ni-Co catalysts for the dry reforming of methane. Appl Catal A Gen 2009;371:54–9. https://doi.org/10.1016/j.apcata.2009.09.026.

[19] Xin J, Cui H, Cheng Z, Zhou Z. Bimetallic Ni-Co/SBA-15 catalysts prepared by urea co-precipitation for dry reforming of methane. Appl Catal A Gen 2018;554:95–104. https://doi.org/10.1016/j.apcata.2018.01.033.

[20] Erdogan B, Arbag H, Yasyerli N. SBA-15 supported mesoporous Ni and Co catalysts with high coke resistance for dry reforming of methane. Int J Hydrogen Energy 2018;43:1396–405. https://doi.org/10.1016/j.ijhydene.2017.11.127.

[21] Zhang J, Li F. Coke-resistant Ni at SiO2 catalyst for dry reforming of methane. Appl Catal B 2015;176–177:513–21. https://doi.org/10.1016/j.apcatb.2015.04.039.

[22] Plata JJ, Graciani J, Evans J, Rodriguez JA, Sanz JF. Cu Deposited on CeOx-Modified TiO2(110): Synergistic Effects at the Metal-Oxide Interface and the Mechanism of the WGS Reaction. ACS Catal 2016;6:4608–15. https://doi.org/10.1021/acscatal.6b00948.

[23] Chein RY, Fung WY. Syngas production via dry reforming of methane over CeO_2 modified Ni/Al2O3 catalysts. Int J Hydrogen Energy 2019;44:14303–15. https://doi.org/10.1016/j.ijhydene.2019.01.113.

[24] Zhang X, Zhang Q, Tsubaki N, Tan Y, Han Y. Influence of Zirconia Phase on the Performance of Ni / ZrO 2 for 2015.

[25] Roh HS, Potdar HS, Jun KW, Kim JW, Oh YS. Carbon dioxide reforming of methane over Ni incorporated into Ce-ZrO 2 catalysts. Appl Catal A Gen 2004;276:231–9. https://doi.org/10.1016/j.apcata.2004.08.009.

[26] Juan-Juan J, Román-Martínez MC, Illán-Gómez MJ. Effect of potassium content in the activity of K-promoted Ni/Al $_2O_3$ catalysts for the dry reforming of methane. Appl Catal A Gen 2006;301:9–15. https://doi.org/10.1016/j.apcata.2005.11.006.

[27] Monteiro WF, Vieira MO, Calgaro CO, Perez-Lopez OW, Ligabue RA. Dry reforming of methane using modified sodium and protonated titanate nanotube catalysts. Fuel 2019;253:713–21. https://doi.org/10.1016/j.fuel.2019.05.019.

[28] Owgi AHK, Jalil AA, Hussain I, Hassan NS, Hambali HU, Siang TJ, et al. Catalytic systems for enhanced carbon dioxide reforming of methane: a review. Environ Chem Lett 2021;19:2157–83. https://doi.org/10.1007/s10311-020-01164-w.

[29] Xu B, Fan Y, Zhang Y, Tsubaki N. Pore diffusion simulation model of bimodal catalyst for Fischer-Tropsch synthesis. AIChE Journal 2005;51:2068–76. https://doi.org/10.1002/aic.10469.

[30] Ma Q, Han Y, Wei Q, Makpal S, Gao X, Zhang J, et al. Stabilizing Ni on bimodal mesoporous-macroporous alumina with enhanced coke tolerance in dry reforming of methane to syngas. Journal of CO2 Utilization 2020;35:288–97. https://doi.org/10.1016/j.jcou.2019.10.010.

[31] Taguchi A, Schüth F. Ordered mesoporous materials in catalysis. vol. 77. 2005. https://doi.org/10.1016/j.micromeso.2004.06.030.

[32] Abdulkareem Ghassan A, Mijan N-A, Hin Taufiq-Yap Y. Nanomaterials: An Overview of Nanorods Synthesis and Optimization. Nanorods and Nanocomposites 2020:1–24. https://doi.org/10.5772/intechopen.84550.

[33] Yu K, Zhang X, Tong H, Yan X, Liu S. Synthesis of fibrous monodisperse core-shell Fe_3O_4/SiO_2/KCC-1. Mater Lett 2013;106:151–4. https://doi.org/10.1016/j.matlet.2013.04.112.

[34] Ding C, Gao X, Han Y, Ma X, Wang J, Liu S, et al. Effects of surface states over core-shell Ni@SiO_2 catalysts on catalytic partial oxidation of methane to synthesis gas. Journal of Energy Chemistry 2015;24:45–53. https://doi.org/10.1016/S2095-4956(15)60283-2.

[35] Owgi AHK, Jalil AA, Hussain I, Hambali HU, Nabgan W. Enhancing resistance of carbon deposition and reaction stability over nickel loaded fibrous silica-alumina (Ni/FSA) for dry reforming of methane. Int J Hydrogen Energy 2022. https://doi.org/10.1016/j.ijhydene.2021.12.134.

[36] Wang M, Zhang Q, Zhang T, Wang Y, Wang J, Long K, et al. Facile one-pot synthesis of highly dispersed Ni nanoparticles embedded in HMS for dry reforming of methane.

Chemical Engineering Journal 2017;313:1370–81. https://doi.org/10.1016/j.cej.2016.11.055.

[37] Naeem MA, Al-Fatesh AS, Fakeeha AH, Abasaeed AE. Hydrogen production from methane dry reforming over nickel-based nanocatalysts using surfactant-assisted or polyol method. Int J Hydrogen Energy 2014;39:17009–23. https://doi.org/10.1016/j.ijhydene.2014.08.090.

[38] Abdulrasheed AA, Jalil AA, Hamid MYS, Siang TJ, Fatah NAA, Izan SM, et al. Dry reforming of methane to hydrogen-rich syngas over robust fibrous KCC-1 stabilized nickel catalyst with high activity and coke resistance. Int J Hydrogen Energy 2019:1–13. https://doi.org/10.1016/j.ijhydene.2019.04.126.

[39] Usman M, Wan Daud WMA, Abbas HF. Dry reforming of methane: Influence of process parameters - A review. Renewable and Sustainable Energy Reviews 2015;45:710–44. https://doi.org/10.1016/j.rser.2015.02.026.

[40] Abdullah N, Ainirazali N, Chong CC, Razak HA, Setiabudi HD, Jalil AA, et al. Influence of impregnation assisted methods of Ni/SBA-15 for production of hydrogen via dry reforming of methane. Int J Hydrogen Energy 2019. https://doi.org/10.1016/j.ijhydene.2019.09.089.

[41] Ashok J, Raju G, Reddy PS, Subrahmanyam M, Venugopal A. Catalytic decomposition of CH_4 over Ni-Al_2O_3-SiO_2 catalysts: Influence of pretreatment conditions for the production of H_2. Journal of Natural Gas Chemistry 2008;17:113–9. https://doi.org/10.1016/S1003-9953(08)60036-5.

[42] Figueredo GP, Medeiros RLBA, Macedo HP, de Oliveira ÂAS, Braga RM, Mercury JMR, et al. A comparative study of dry reforming of methane over nickel catalysts supported on perovskite-type LaAlO3 and commercial A-Al_2O_3. Int J Hydrogen Energy 2018;43:11022–37. https://doi.org/10.1016/j.ijhydene.2018.04.224.

[43] Liotta LF, Wu H, Pantaleo G, Venezia AM. Co_3O_4 nanocrystals and Co_3O_4-MOx binary oxides for CO, CH_4 and VOC oxidation at low temperatures: A review. Catal Sci Technol 2013;3:3085–102. https://doi.org/10.1039/c3cy00193h.

[44] Littlewood P, Liu S, Weitz E, Marks TJ, Stair PC. Ni-alumina dry reforming catalysts: Atomic layer deposition and the issue of Ni aluminate. Catal Today 2020;343:18–25. https://doi.org/10.1016/j.cattod.2019.03.040.

[45] Huang X, Xue G, Wang C, Zhao N, Sun N, Wei W, et al. Highly stable mesoporous NiO-Y_2O_3-Al_2O_3 catalysts for CO_2 reforming of methane: Effect of Ni embedding and Y_2O_3 promotion. Catal Sci Technol 2016;6:449–59. https://doi.org/10.1039/c5cy01171j.

[46] Li J, Miao P, Li Z, He T, Han D, Wu J, et al. Hydrothermal synthesis of nanocrystalline H[Fe, Al]ZSM-5 zeolites for conversion of methanol to gasoline. Energy Convers Manag 2015;93:259–66. https://doi.org/10.1016/j.enconman.2015.01.031.

[47] Pinheiro AN, Valentini A, Sasaki JM, Oliveira AC. Highly stable dealuminated zeolite support for the production of hydrogen by dry reforming of methane. Appl Catal A Gen 2009;355:156–68. https://doi.org/10.1016/j.apcata.2008.12.007.

[48] Owgi AHK, Jalil AA, Aziz MAA, Nabgan W, Hassan NS, Hussain I, et al. The preferable Ni quantity to boost the performance of FSA for dry reforming of methane. Fuel 2023;332. https://doi.org/10.1016/j.fuel.2022.126124.

[49] de Freitas Silva T, Reis CGM, Lucrédio AF, Assaf EM, Assaf JM. Hydrogen production from oxidative reforming of methane on Ni/γ-Al_2O_3 catalysts: Effect of support promotion with La, La-Ce and La-Zr. Fuel Processing Technology 2014;127:97–104. https://doi.org/10.1016/j.fuproc.2014.06.002.

[50] Kumar P, Sun Y, Idem RO. Comparative study of Ni-based mixed oxide catalyst for carbon dioxide reforming of methane. Energy and Fuels 2008;22:3575–82. https://doi.org/10.1021/ef800326q.

[51] Budiman AW, Song SH, Chang TS, Shin CH, Choi MJ. Dry Reforming of Methane Over Cobalt Catalysts: A Literature Review of Catalyst Development. Catalysis Surveys from Asia 2012;16:183–97. https://doi.org/10.1007/s10563-012-9143-2.

[52] Licciulli A, Notaro M, Santis S de, Terreni C, Kunjalukkal S. CO 2 capture on amine impregnated mesoporous alumina-silica mixed oxide spheres. Fuel Processing Technology 2017;166:202–8. https://doi.org/10.1016/j.fuproc.2017.06.009.

[53] Daniell W, Schubert U, Glöckler R, Meyer A, Noweck K, Knözinger H. Enhanced surface acidity in mixed alumina-silicas: a low-temperature FTIR study. vol. 196. 2000.

[54] Omata K, Nambu T. Catalysis of water molecules acting as Brönsted acids at Lewis acid sites on niobium oxide. Appl Catal A Gen 2020;607. https://doi.org/10.1016/j.apcata.2020.117812.

[55] Ding L, Li M, Zhao Y, Zhang H, Shang J, Zhong J, et al. The vital role of surface Brönsted acid/base sites for the photocatalytic formation of free ·OH radicals. Appl Catal B 2020;266. https://doi.org/10.1016/j.apcatb.2020.118634.

[56] Hambali HU, Jalil AA, Abdulrasheed AA, Siang TJ, Abdullah TAT, Ahmad A, et al. Fibrous spherical Ni-M/ZSM-5 (M: Mg, Ca, Ta, Ga) catalysts for methane dry reforming: The interplay between surface acidity-basicity and coking resistance. Int J Energy Res 2020:1–17. https://doi.org/10.1002/er.5327.

[57] sheng1994 n.d.

[58] Wood DL, Rabinovich EM. HEAT EVOLUTION, LIGHT SCAITERING, AND INFRARED SPECTROSCOPY IN THE FORMATION OF SILICA GELS FROM ALKOXIDES. vol. 107. 1989.

[59] Marie O, Massiani P, Thibault-Starzyk F. Infrared Evidence of a Third Brønsted Site in Mordenites. Journal of Physical Chemistry B 2004;108:5073–81. https://doi.org/10.1021/jp037915v.

[60] Montanari T, Marie O, Daturi M, Busca G. Cobalt on and in zeolites and silica-alumina: Spectroscopic characterization and reactivity. Catal Today, vol. 110, 2005, p. 339–44. https://doi.org/10.1016/j.cattod.2005.09.034.

[61] Chong CC, Teh LP, Setiabudi HD. Syngas production via CO_2 reforming of CH_4 over Ni-based SBA-15: Promotional effect of promoters (Ce, Mg, and Zr). Mater Today Energy 2019;12:408–17. https://doi.org/10.1016/j.mtener.2019.04.001.

[62] Chen BH, Chao ZS, He H, Huang C, Liu YJ, Yi WJ, et al. Towards a full understanding of the nature of Ni(II) species and hydroxyl groups over highly siliceous HZSM-5 zeolite supported nickel catalysts prepared by a deposition-precipitation method. Dalton Transactions 2016;45:2720–39. https://doi.org/10.1039/c4dt00399c.

[63] Zhang RJ, Xia GF, Li MF, Wu Y, Nie H, Li DD. Effect of support on catalytic performance of Ni-based catayst in methane dry reforming. Ranliao Huaxue Xuebao/Journal of Fuel Chemistry and Technology 2015;43:1359–65. https://doi.org/10.1016/S1872-5813(15)30040-2.

[64] San-José-Alonso D, Juan-Juan J, Illán-Gómez MJ, Román-Martínez MC. Ni, Co and bimetallic Ni-Co catalysts for the dry reforming of methane. Appl Catal A Gen 2009;371:54–9. https://doi.org/10.1016/j.apcata.2009.09.026.

[65] Rodriguez JA, Liu P, Wang X, Wen W, Hanson J, Hrbek J, et al. Water-gas shift activity of Cu surfaces and Cu nanoparticles supported on metal oxides. Catal Today 2009;143:45–50. https://doi.org/10.1016/j.cattod.2008.08.022.

[66] Shido T, Asakura K. Reactant-Promoted Reaction Mechanism for Catalytic Water-Gas Shift Reaction on MgO. vol. 122. 1990.

[67] Chen W, Zhao G, Xue Q, Chen L, Lu Y. High carbon-resistance Ni/$CeAlO_3$-Al_2O_3 catalyst for CH4/CO2 reforming. Appl Catal B 2013;136–137:260–8. https://doi.org/10.1016/j.apcatb.2013.01.044.

[68] Chong CC, Bukhari SN, Cheng YW, Setiabudi HD, Jalil AA, Phalakornkule C. Robust Ni/Dendritic fibrous SBA-15 (Ni/DFSBA-15) for methane dry reforming: Effect of Ni loadings. Appl Catal A Gen 2019;584. https://doi.org/10.1016/j.apcata.2019.117174.

[69] Ribeiro NFP, Neto RCR, Moya SF, Souza MMVM, Schmal M. Synthesis of NiAl2O4 with high surface area as precursor of Ni nanoparticles for hydrogen production. Int J Hydrogen Energy 2010;35:11725–32. https://doi.org/10.1016/j.ijhydene.2010.08.024.

[70] Moradi G, Khezeli F, Hemmati H. Syngas production with dry reforming of methane over Ni/ZSM-5 catalysts. J Nat Gas Sci Eng 2016;33:657–65. https://doi.org/10.1016/j.jngse.2016.06.004.

[71] Hambali HU, Jalil AA, Abdulrasheed AA, Siang TJ, Vo DVN. Enhanced dry reforming of methane over mesostructured fibrous Ni/MFI zeolite: Influence of preparation methods. Journal of the Energy Institute 2020. https://doi.org/10.1016/j.joei.2020.01.016.

[72] Nguyen TGH, Tran DL, Sakamoto M, Uchida T, Sasaki K, To TD, et al. Ni-loaded (Ce,Zr)O_2–Δ-dispersed paper-structured catalyst for dry reforming of methane. Int J Hydrogen Energy 2018;43:4951–60. https://doi.org/10.1016/j.ijhydene.2018.01.118.

[73] Zhang Y, Tao Y, Huang J, Williams P. Influence of silica–alumina support ratio on H2 production and catalyst carbon deposition from the Ni-catalytic pyrolysis/reforming of waste tyres. Waste Management and Research 2017;35:1045–54. https://doi.org/10.1177/0734242X17722207.

[74] Gurav HR, Dama S, Samuel V, Chilukuri S. Influence of preparation method on activity and stability of Ni catalysts supported on Gd doped ceria in dry reforming of methane. Journal of CO_2 Utilization 2017;20:357–67. https://doi.org/10.1016/j.jcou.2017.06.014.

[75] Meng J, Gu T, Pan W, Bu C, Zhang J, Wang X, et al. Promotional effects of defects on Ni/HAP catalyst for carbon resistance and durability during dry reforming of methane. Fuel 2022;310:122363. https://doi.org/10.1016/j.fuel.2021.122363.

[76] Zhang ZL, Verykios XE. Carbon dioxide reforming of methane to synthesis gas over supported Ni catalysts. Catal Today 1994;21:589–95. https://doi.org/10.1016/0920-5861(94)80183-5.

[77] Han JW, Park JS, Choi MS, Lee H. Uncoupling the size and support effects of Ni catalysts for dry reforming of methane. Appl Catal B 2017;203:625–32. https://doi.org/10.1016/j.apcatb.2016.10.069.

[78] Serrano-Lotina A, Daza L. Highly stable and active catalyst for hydrogen production from biogas. J Power Sources 2013;238:81–6. https://doi.org/10.1016/j.jpowsour.2013.03.067.

[79] Navalikhina MD, Kavalerskaya NE, Lokteva ES, Peristyi AA, Golubina E v., Lunin V v. Hydrodechlorination of chlorobenzene on Ni and Ni-Pd catalysts modified by heteropolycompounds of the keggin type. Russian Journal of Physical Chemistry A 2012;86:1669–75. https://doi.org/10.1134/S0036024412110192.

[80] Phan TS, Sane AR, Rêgo de Vasconcelos B, Nzihou A, Sharrock P, Grouset D, et al. Hydroxyapatite supported bimetallic cobalt and nickel catalysts for syngas production from dry reforming of methane. Appl Catal B 2018;224:310–21. https://doi.org/10.1016/j.apcatb.2017.10.063.

Table.1. X-ray fluorescence XRF analysis results to catalyst content.

Sample	Ni (% wt)	Co (%wt)	SiO_2 (%wt)	Al_2O_3 (% wt)
Co/FSA	-	5.10%	76.18%	18.7%
Ni/FSA	4.84 %	__-	79.2%	16.5%

Table .2. Textural properties of prepared catalyst samples.

Catalyst	Surface Area m^2/g	Micropore volume cm^3/g	Mesopore volume cm^3/g	Total Pore Volume cm^3/g	Pore Size nm
FSA	334.92	0.0038	1.20	1.21	14.45
Ni/FSA	338.56	0.0053	1.05	1.05	12.51
Co/FSA	303.6	0.0015	0.97	0.98	0.86

Graphical Abstract

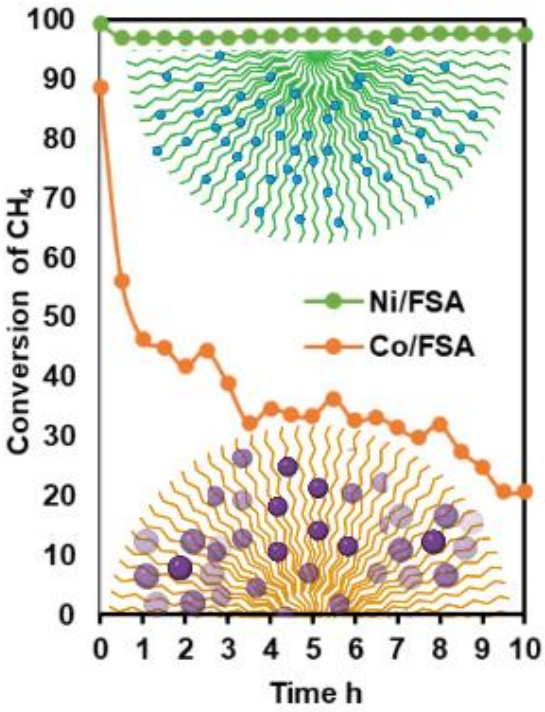

List of Figure

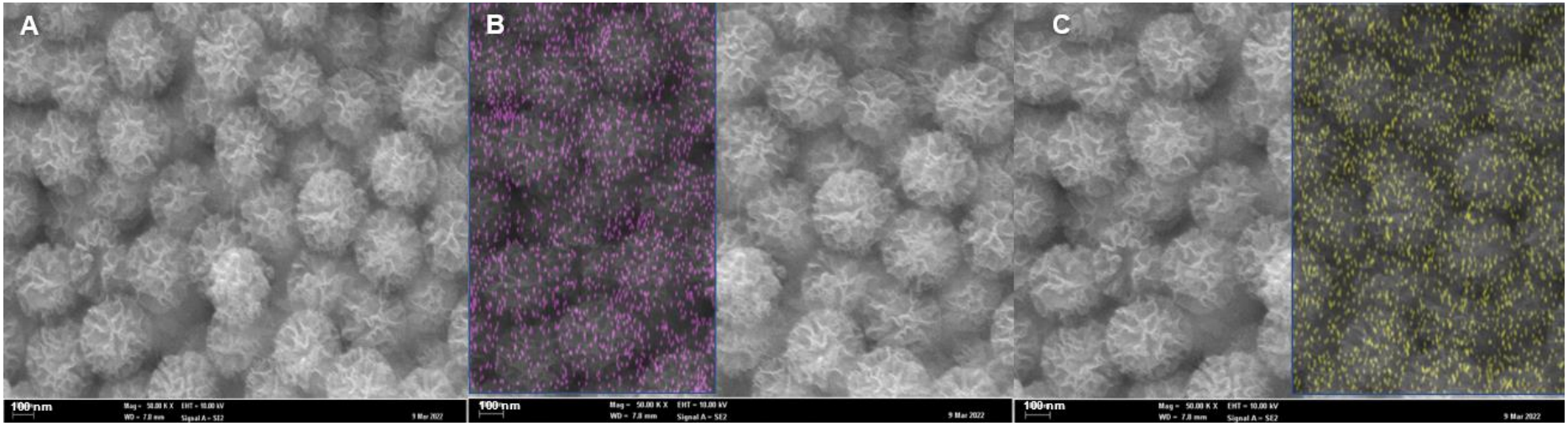

Fig.1. (A) FESEM image of FSA diffusion, (B) The particle mapping of Ni/FSA, (C) Co/FSA with mapping.

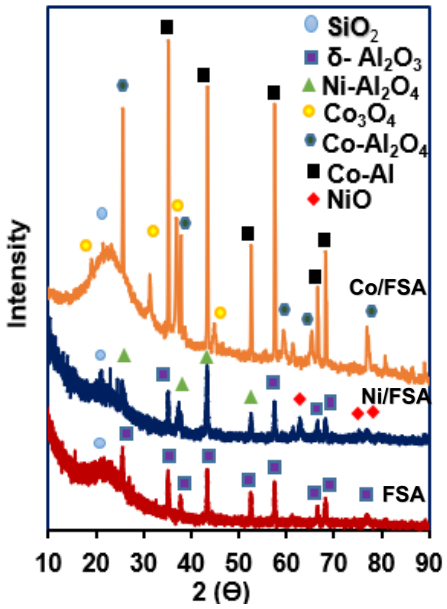

Fig. 2. Wide-angle XRD pattern for the fresh catalyst of FSA, Ni/FSA, and Co/FSA.

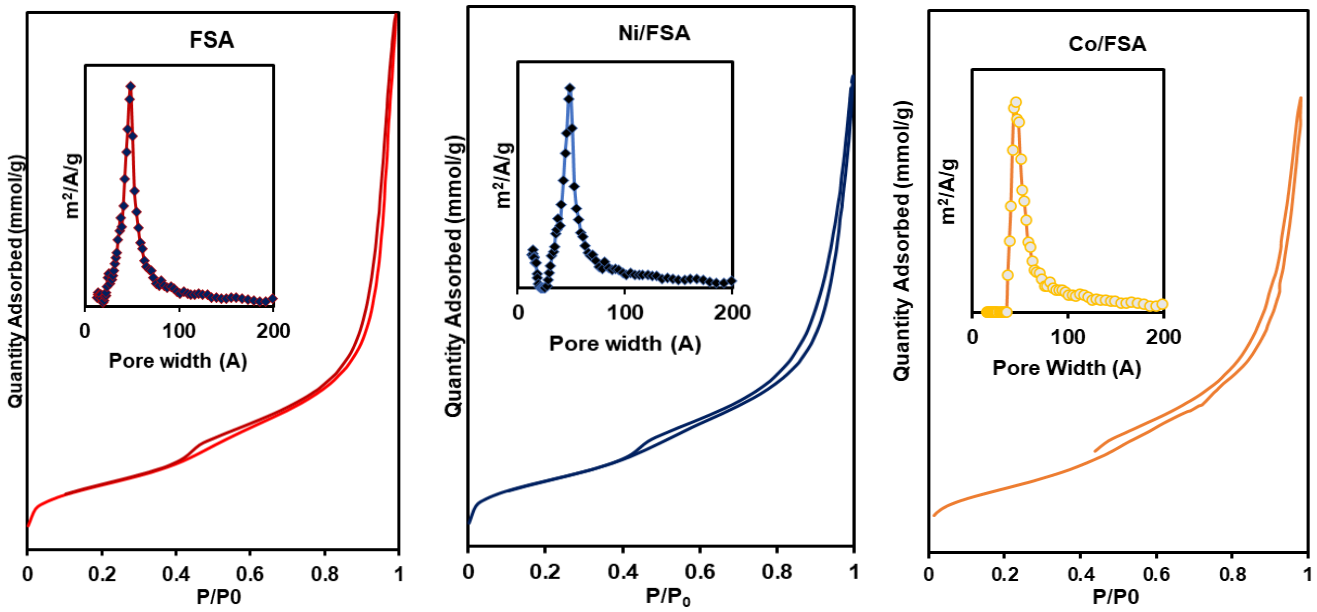

Fig. 3. N_2 adsorption-desorption isotherms and pore size distribution of FSA, Ni/FSA, and Co/FSA.

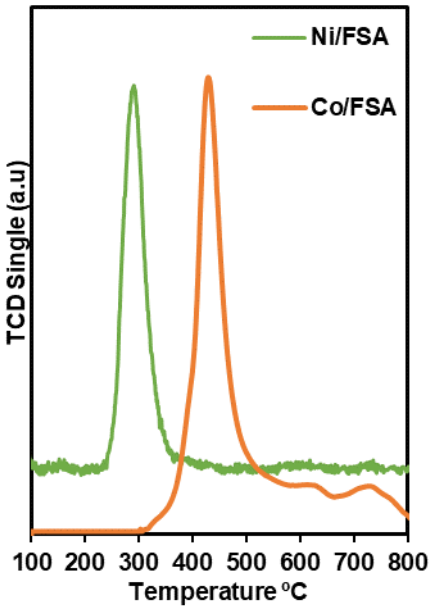

Fig 4. H_2-TPR spectrum of Ni/FSA, and Co/FSA.

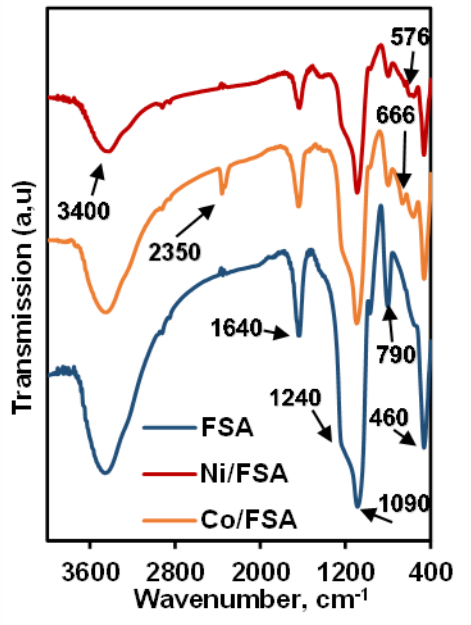

Fig.5. IR study, KBr-FTIR patterns of FSA, Ni/FSA, and Co/FSA.

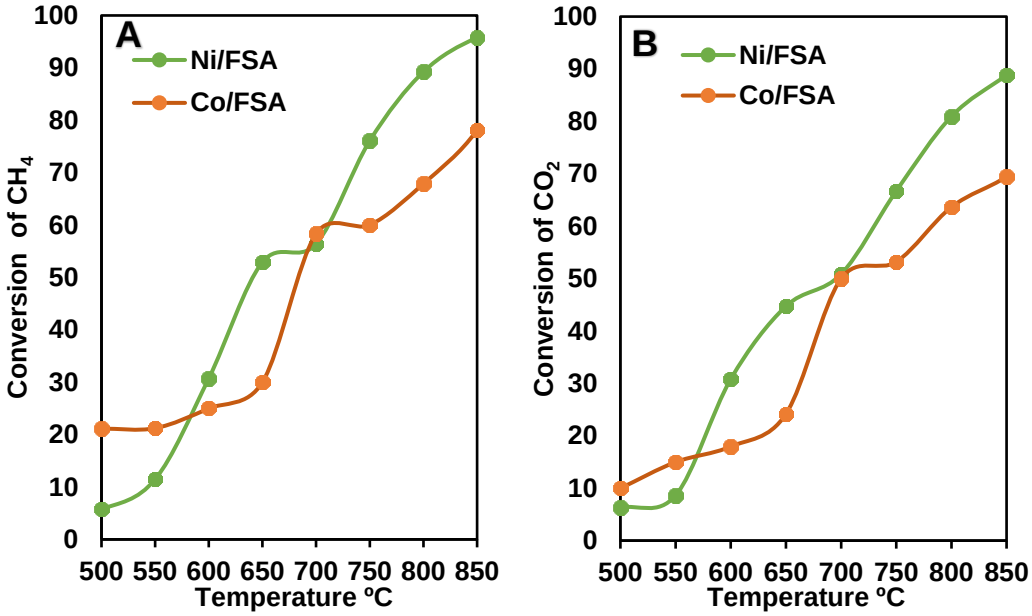

Fig .6. Catalytic performance over the catalysts (A) CH_4 conversion and (B) CO_2 conversion with different catalysts (Condition: CO_2/CH_4=1:1, GHSV=50,000 $mL \cdot g_{cat}^{-1} \cdot h^{-1}$, P= 1atm, T= 500 to 850 ºC).

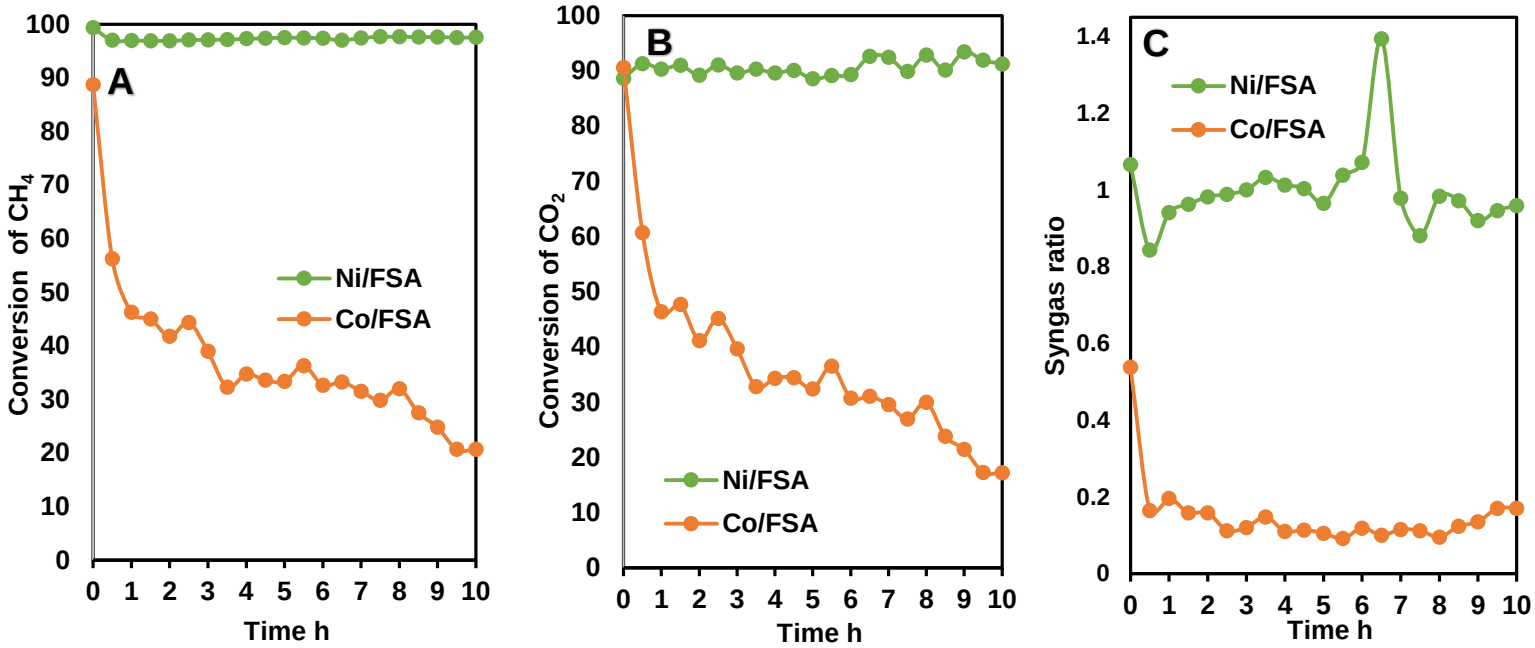

Fig. 7. Catalytic stability over the catalysts (A) CH_4 conversion, (B) CO_2 conversion, and (C) H_2/CO ratio (Condition: CO_2/CH_4=1:1, GHSV=50,000 $mL \cdot_{gcat}^{-1} \cdot h^{-1}$, P=1atm, T=850 °C, Tim= 10h).

.

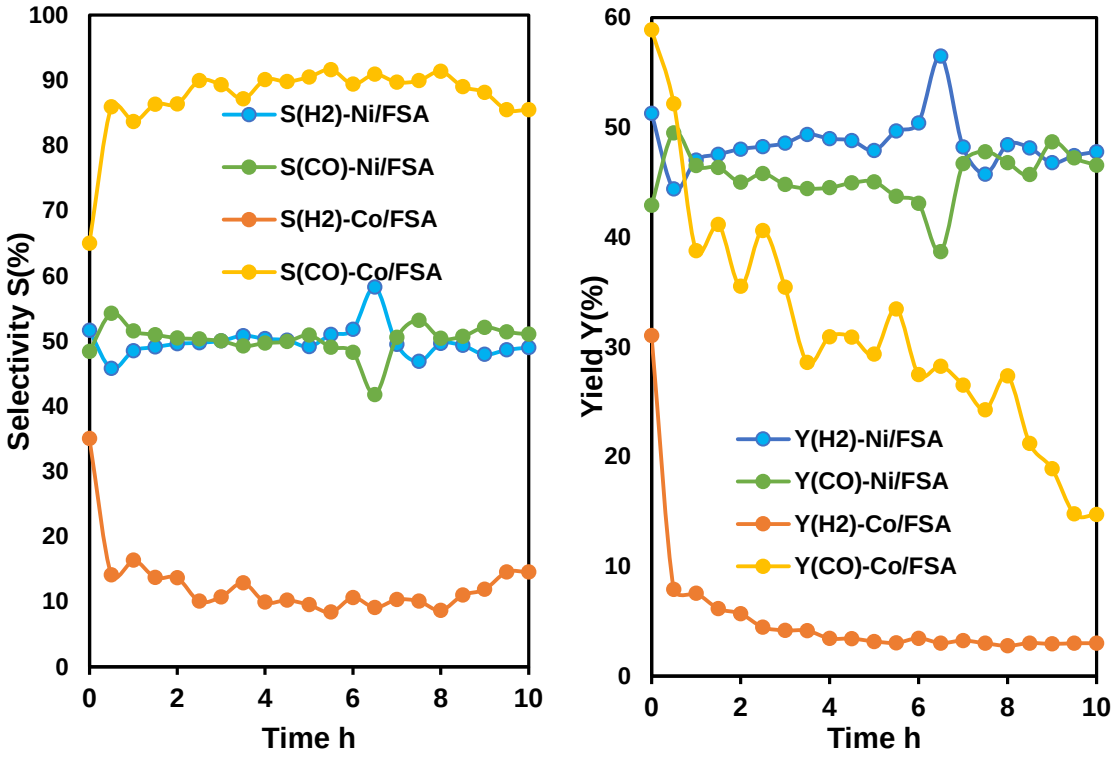

Fig. 8. (A) Selectivity of H_2 and CO, the (B) yield of H_2 and Co during methane dry reforming over Ni/FSA and Co/FSA

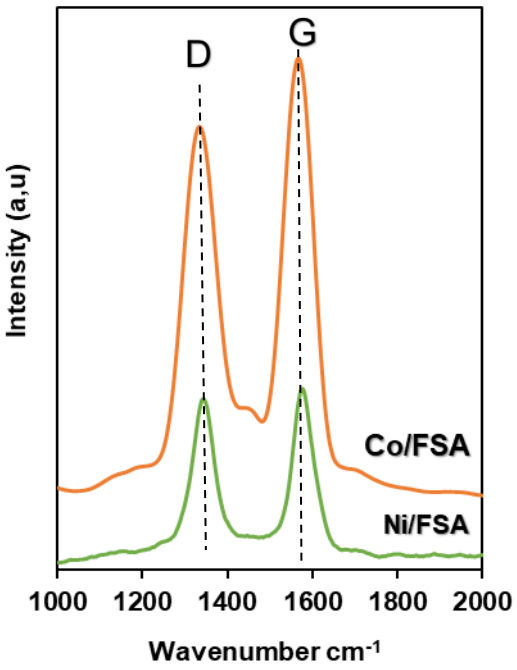

Fig .9. Raman spectroscopy of spent catalyst Ni/FSA and Co/FSA.

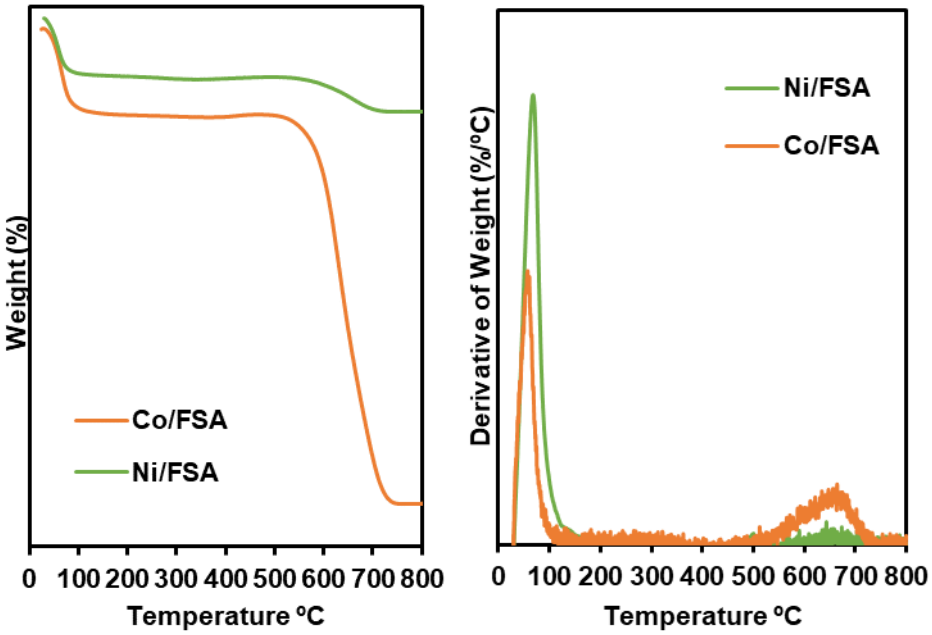

Fig.10. Analysis of carbon deposition on spent catalysts Ni/FSA, and Co/FSA by (A) TGA, and (B) DTG profiles.

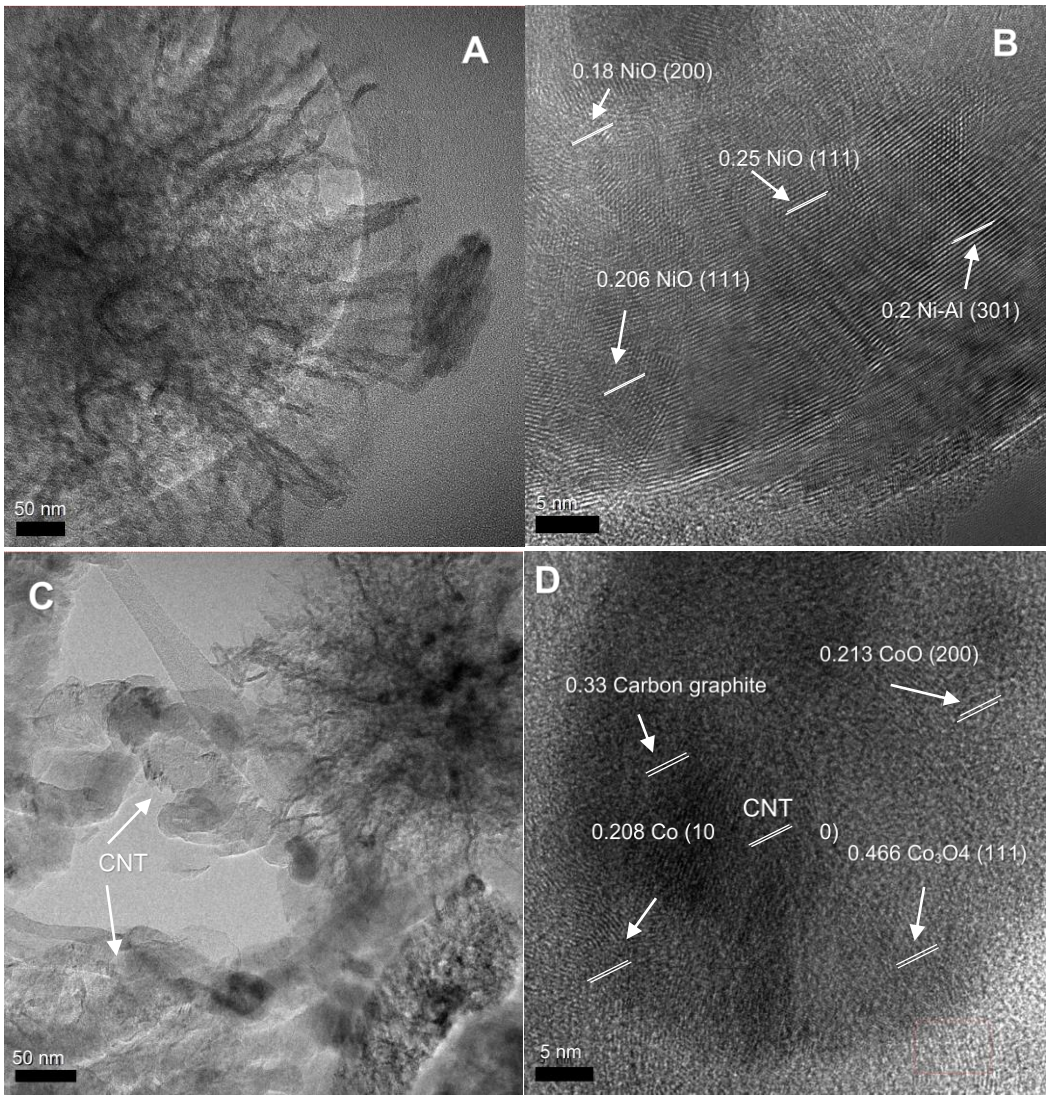

Fig.11. TEM image of the spent catalyst after stability test 10h (A & B) Ni/FSA and (C&D) Co/FSA

Declaration of interests

☒ The authors declare that they have no known competing financial interests or personal relationships that could have appeared to influence the work reported in this paper.

☐The authors declare the following financial interests/personal relationships which may be considered as potential competing interests: